

APPLIED PHYSICS REVIEWS

Two-dimensional carbon nanostructures: Fundamental properties, synthesis, characterization, and potential applications

Y. H. Wu,^{1,a)} T. Yu,² and Z. X. Shen²

¹*Department of Electrical and Computer Engineering, National University of Singapore, 4 Engineering Drive 3, Singapore 117576*

²*Division of Physics and Applied Physics, School of Physical and Mathematical Sciences, Nanyang Technological University, 1 Nanyang Walk, Block 5, Level 3, Singapore 637616*

(Received 4 July 2009; accepted 14 June 2010; published online 13 October 2010)

Since its discovery in less than five years ago, graphene has become one of the hottest frontiers in materials science and condensed matter physics, as evidenced by the exponential increase in number of publications in this field. Several reviews have already been published on this topic, focusing on single and multilayer graphene sheets. Here, we review the recent progresses in this field by extending the scope to various types of two-dimensional carbon nanostructures including graphene and free-standing carbon nanowalls/nanosheets. After a brief overview of the electronic properties of graphene, we focus on the synthesis, characterization and potential applications of these carbon nanostructures. © 2010 American Institute of Physics. [doi:10.1063/1.3460809]

TABLE OF CONTENTS

| | | | |
|--|----|---|----|
| I. INTRODUCTION..... | 1 | 1. Superstructures of epitaxial graphene..... | 24 |
| II. BAND STRUCTURE OF GRAPHENE..... | 2 | 2. Scattered electron waves..... | 25 |
| A. Low-energy electronic spectrum..... | 2 | 3. STS measurement of band gaps..... | 25 |
| B. Effect of a perpendicular magnetic field..... | 4 | 4. Topographic corrugations and charge puddles..... | 25 |
| C. Electrostatic confinement and tunneling..... | 4 | 5. Landau energy levels..... | 26 |
| III. ELECTRICAL TRANSPORT PROPERTIES OF GRAPHENE..... | 5 | 6. Electron–phonon interaction..... | 26 |
| A. Weak (weak-anti) localization..... | 6 | VI. RAMAN SPECTROSCOPY/IMAGING STUDY ON GRAPHENE..... | 27 |
| B. Electrical conductivity and mobility of graphene..... | 7 | A. Thickness determination of graphene layers using Raman spectroscopy..... | 27 |
| IV. SYNTHESIS OF 2D CARBON NANOSTRUCTURES..... | 8 | B. Raman study on strain effect..... | 28 |
| A. Exfoliation..... | 8 | C. Raman study on the doping effect..... | 29 |
| 1. Mechanical exfoliation..... | 8 | D. Raman study on misoriented bilayer graphene..... | 30 |
| 2. Chemical exfoliation..... | 9 | E. Raman study of the crystallographic orientation of graphene..... | 31 |
| B. Graphene on metal surface..... | 12 | VII. POTENTIAL APPLICATIONS OF 2D CARBON..... | 32 |
| C. Graphene on SiC..... | 14 | A. Electronic devices..... | 32 |
| D. Synthesis of free-standing 2D carbon..... | 16 | B. Transparent conductive films..... | 32 |
| E. Fabrication of GNRs..... | 20 | C. Mechanical devices..... | 32 |
| V. STRUCTURAL PROPERTIES OF GRAPHENE AND 2D CARBON..... | 21 | D. Chemical sensors..... | 32 |
| A. TEM..... | 21 | E. Spintronic devices..... | 33 |
| 1. Thickness determination..... | 21 | VIII. SUMMARY..... | 33 |
| 2. Observation of ripples..... | 21 | | |
| 3. Observation of atomic images..... | 21 | | |
| 4. Edges and their dynamics..... | 22 | | |
| 5. Multiple layers..... | 23 | | |
| 6. Patterning of graphene..... | 23 | | |
| B. STM..... | 23 | | |

I. INTRODUCTION

The properties of a material at mesoscopic scale are determined not only by the nature of its chemical bonds but also its dimensionality and shape. This is particularly true for carbon-based materials. Carbon, in the ground state, has four valence electrons, two in the 2s subshell and two in the 2p subshell. When forming bonds with other carbon atoms, it

^{a)}Electronic mail: elewuyh@nus.edu.sg.

will promote one of its $2s$ electrons into its empty $2p$ orbital and then form bonds with other carbon atoms via sp hybrid orbitals. Depending on the number of p orbitals (1 to 3) mixing with the s orbital, there are three kinds of sp hybrid orbitals, i.e., sp , sp^2 , and sp^3 hybrid orbitals. Carbon atoms with sp^2 and sp^3 hybrid orbitals are able to form three and four bonds with neighboring carbon atoms, respectively, which form the bases of graphene and diamond. An ideal graphene is a monatomic layer of carbon atoms arranged on a honeycomb lattice; therefore, graphene is a perfect two-dimensional (2D) material. As ideal 2D crystals at free-state are unstable at finite temperature,¹ graphene tends to evolve into other types of structures with enhanced stability, such as graphite, fullerene, and nanotubes.² Graphite is formed through layering of a large number of graphene layers via van der Waals force; therefore, from physics point of view, it falls into the category of three-dimensional (3D) systems. Under appropriate conditions, a single-layer graphene (SLG) or multiple layer graphene (MLG) can also roll up along certain directions to form tabular structure called carbon nanotubes (CNTs).³ The CNTs, which can be in the form of single-walled, double-walled, and multiple-walled structures, are considered as one-dimensional (1D) objects.⁴ With the introduction of pentagons, the graphene can also be wrapped up to form zero-dimensional (0D) fullerenes.⁵ Although ideal graphene is unstable, it may become stable through the introduction of local curvatures or support formed by foreign materials. Macroscopic SLG was successfully isolated from graphite through mechanical exfoliation in 2004, which was found to be stable on a foreign substrate, highly crystalline, and chemically inert under ambient conditions,^{6–8} albeit with local roughness and ripples.⁹

Among all carbon allotropes, graphene stands out because of its quasirelativistic low-energy excitations near the two inequivalent K points at the corners of the first Brillouin zone (BZ); the quasiparticles are chiral and massless Dirac fermions with the electrons and holes degenerated at the Dirac points.^{10–14} This gives rise to a number of peculiar physical properties of graphene distinguishing it from conventional 2D electron gas systems (2DEGs).¹⁵ Some of the unique physical phenomena that have been observed or explored so far include unconventional integer quantum Hall effect (IQHE),^{7,8} Klein tunneling,^{16–18} valley polarization,^{19,20} universal (nonuniversal) minimum conductivity,^{21–24} weak (weak anti-) localization (WAL),^{21,25–29} ultrahigh mobility,^{21,30–32} specular Andreev reflection at the graphene–superconductor interface,^{33,34} etc.

Since the discovery of SLG, tremendous progresses have been made in developing/redeveloping various types of techniques for synthesizing both SLG and multilayer graphene (MLG) sheets, such as epitaxial growth on both SiC and metallic substrates,^{35–39} reduction from graphite oxide (GO),⁴⁰ chemical vapor deposition (CVD),^{41–44} electrical discharge,⁴⁵ etc. It is worth noting that most of these techniques are not new and they have been used to grow various types of 2D graphitic materials. Although so far mechanical exfoliation still remains as the method of choice for producing graphene of highest quality, epitaxial growth and chemical synthesis, including both dry and wet techniques, are

potentially more useful for practical applications. As a matter of fact, prior to the discovery of graphene, various types of 2D carbon sheets have been synthesized and discussed in the literature, such as carbon nanowalls (CNWs),⁴² carbon flakes, and nanographite sheets.⁴³ Most of these 2D carbon sheets are synthesized by microwave plasma-enhanced vapor deposition (MWPECVD) or rf plasma-enhanced vapor deposition (rf-PECVD) which has been demonstrated recently as a viable technique to produce both SLGs and MLGs.^{46,47} The recent finding of MLGs exhibiting behaviors similar to those of SLGs is encouraging, which may eventually make SLG unnecessary for attaining SLG-like behaviors.^{48,49} Comparing to SLGs, the MLGs are more immune to the influence of external environment.

The current interest in graphene is phenomenal, as evidenced by the large number of publications published in the last few years. Several excellent reviews have been written on graphene, focusing on fundamental physics and structural/electronic properties.^{14,21,50–54} There are also comprehensive reviews on the chemical synthesis and epitaxial growth of graphene using both physical and chemical methods.^{35–40} However, a comparative review on all the major methods for producing and characterizing graphene is still lacking. In this review, after providing a brief survey on the unique band structures and related electrical transport properties of graphene, we focus on the recent progresses made in synthesis and characterization of 2D carbons using various techniques. The review on electrical transport is not intended to be comprehensive; rather it is to serve as a guide to compare the quality of 2D carbons fabricated by different techniques. The remaining of this review is organized as follows. In Sec. II, we provide an overview of the basic properties of graphene by focusing on its electronic band structure. The electrical transport properties are discussed in Sec. III. The synthesis of graphene using various types of techniques is reviewed in Sec. IV. In Secs. V and VI, we discuss the characterization of graphene by focusing on its structural properties using scanning tunneling microscopy (STM), transmission electron microscopy (TEM), and Raman spectroscopy. Finally, in Sec. VII, we summarize some of the potential applications reported so far.

II. BAND STRUCTURE OF GRAPHENE

A. Low-energy electronic spectrum

Graphene is a single layer of carbon atoms arranged in a honeycomb lattice, as shown in Fig. 1(a). The unit cell spanned by the following two lattice vectors:

$$\vec{a}_1 = \left(\frac{3}{2}a, -\frac{\sqrt{3}}{2}a \right), \quad \vec{a}_2 = \left(\frac{3}{2}a, \frac{\sqrt{3}}{2}a \right), \quad (1)$$

contains two atoms, one of type A and the other of type B, which represents the two triangular lattices. Here, $a = 0.142$ nm, is the carbon bond length. The corresponding reciprocal lattice vectors are given by

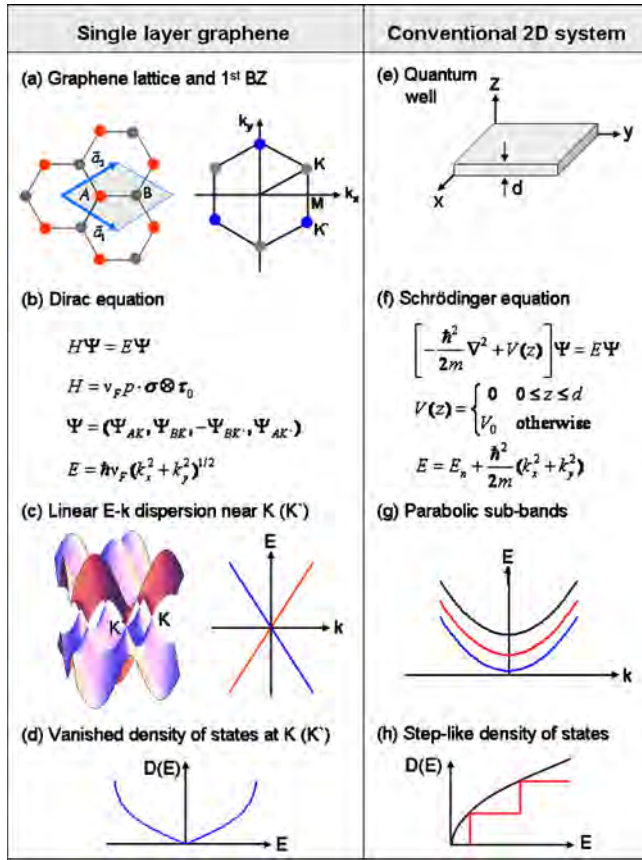


FIG. 1. (Color online) Comparison of graphene [(a)–(d)] and conventional 2D electron systems [(e)–(i)]. (a) Lattice structure and first BZ; (b) Dirac equations; (c) 3D (left) and 2D (right) energy dispersions; (d) DOS as a function of energy; (f) Schematic of a conventional 2DEG confined by electrostatic potentials in the z direction; (g) Schrödinger equation; (h) E - K dispersion curves; (i) DOS as a function of energy.

$$\vec{g}_1 = \frac{4\pi}{3\sqrt{3}a} \left(\frac{\sqrt{3}}{2}, -\frac{3}{2} \right), \quad \vec{g}_2 = \frac{4\pi}{3\sqrt{3}a} \left(\frac{\sqrt{3}}{2}, \frac{3}{2} \right), \quad (2)$$

which also form a honeycomb lattice. The first BZ is a hexagon with a side length of $4\pi/3\sqrt{3}a$. Of particular interest inside the first BZ are two points $\vec{K} = ((2\pi/3a), (2\pi/3\sqrt{3}a))$ and $\vec{K}' = ((2\pi/3a), -(2\pi/3\sqrt{3}a))$, where as will become clear later, the A and B lattices decouple, forming the so-called Dirac point.

As it is discussed briefly in the introduction, each carbon in the ground state has four valence electrons, two in the $2s$ subshell and two in the $2p$ subshell. When forming bonds with other carbon atoms, it will first promote one of its $2s$ electrons into its empty $2p$ orbital and then form bonds with other carbon atoms via sp hybrid orbitals. In the case of graphene, $2p$ orbitals hybridize with one s orbital to form three sp^2 orbitals, which subsequently form the so-called σ bonds with the three nearest-neighbor carbon atoms in the honeycomb lattice. The σ bonds are energetically very stable and localized; therefore, they do not contribute to electrical conduction. In addition to electrons in forming the σ bonds, there is the fourth electron that occupies the $2p_z$ orbital. The overlap of $2p_z$ electron wave functions from neighboring carbon atoms leads to a good electrical conductivity in the graphene plane.

The band structure of graphene has been calculated using the tight-binding approximation by taking into account the $2p_z$ orbital only for each of the two atoms in every primitive cell.^{10,12} The calculation involves the construction of a wave function which is the linear combination of Bloch wave functions for A and B atoms and the use of variational principle to obtain the eigenfunctions and eigenstates. Ignoring the interaction between second nearest neighboring atoms, the energy dispersion of π and π^* bands is given by

$$E(k) = \pm \gamma_0 \sqrt{1 + 4 \cos\left(\frac{3}{2}k_x a\right) \cos\left(\frac{\sqrt{3}}{2}k_y a\right) + 4 \cos^2\left(\frac{\sqrt{3}}{2}k_y a\right)}, \quad (3)$$

where k_x and k_y are the components of \vec{k} in the (k_x, k_y) plane, $\gamma_0 = 2.75$ eV is the nearest-neighbor hopping energy, and plus (minus) sign refers to the upper (π^*) and lower (π) band. Figure 1(c) shows the 3D electronic dispersion (left) and energy contour lines (right) in k -space. Near the K and K' points, the energy dispersion has a circular cone shape which, to a first order approximation, is given by

$$E(k) = \pm \hbar v_F |k|, \quad (4)$$

here $v_F = (3\gamma_0 a / 2\hbar) \approx 10^6$ ms⁻¹ is the Fermi velocity. Note that, in Eq. (4), the wavevector k is measured from the K and K' points. This kind of energy dispersion is distinct from that of nonrelativistic electrons, i.e., $E(k) = (\hbar^2 k^2 / 2m)$, where m is the electrons mass. The linear dispersion becomes “distorted” with increasing k away from the K and K' point due to a second-order term with a threefold symmetry; this is known as trigonal warping of the electronic spectrum in literature.^{55–57}

The salient features of low-energy electron dynamics in graphene are better understood by modeling the electrons as relativistic Weyl fermions (within the $\vec{k} \cdot \vec{p}$ approximation), which satisfy the 2D Dirac equations^{12,17,58}

$$-i\hbar v_F \sigma \cdot \nabla \psi = E \psi \quad (\text{around K point}),$$

$$-i\hbar v_F \sigma^* \cdot \nabla \psi' = E \psi' \quad (\text{around K' point}), \quad (5)$$

where $\sigma = (\sigma_x, \sigma_y)$, $\sigma^* = (\sigma_x, -\sigma_y)$, $\sigma_x = \begin{bmatrix} 0 & 1 \\ 1 & 0 \end{bmatrix}$, $\sigma_y = \begin{bmatrix} 0 & -i \\ i & 0 \end{bmatrix}$, $\psi = (\psi_A, \psi_B)$, and $\psi' = (\psi'_A, \psi'_B)$. Equation (5) can be readily solved to obtain the eigenvalues and eigenfunctions (envelope functions) as follows:

$$E_\alpha = \alpha \hbar v_F (k_x^2 + k_y^2)^{1/2},$$

$$\psi_{\alpha\beta}(\vec{k}) = \frac{1}{\sqrt{2}} \begin{pmatrix} e^{-i\beta\theta_{\vec{k}}/2} \\ \alpha e^{i\beta\theta_{\vec{k}}/2} \end{pmatrix}, \quad (6)$$

where $\alpha = 1$ (-1) corresponds to the conduction and valence bands, $\beta = 1$ (-1) refers to the K and K' valley, and $\theta_{\vec{k}} = \tan^{-1}(k_y/k_x)$ is determined by the direction of wave vector in k -space. Therefore, for both valleys, the rotation of \vec{k} in the (k_x, k_y) plane (surrounding K or K' point) by 2π will result in a phase change in π of the wave function (so-called Berry's phase).⁵⁹ The Berry phase of π has important implications to electron transport properties which will become clear later. The eigenfunctions are two-component spinors; low-energy electrons in graphene possess a pseudospin (with

$\alpha = +(-)1$ corresponding to up (down) pseudospin).⁶⁰ The spinors are also the eigenfunctions of the helicity operator $\hat{h} = 1/2\sigma \cdot \vec{p}/|\vec{p}|$. It is straightforward to show that $\hat{h}\psi_{\alpha\beta} = \alpha\beta 1/2\psi_{\alpha\beta}$. Take \vec{n} as the unit vector in the momentum direction, one has $\vec{n} \cdot \vec{k} = 1$ for electrons and $\vec{n} \cdot \vec{k} = -1$ for holes.¹⁴

The unique band structure near the K point is also accompanied by a unique energy-dependence of density of states (DOS). For a 2D system with dimension of $L \times L$, each electron state occupies an area of $2\pi/L^2$ in k -space. Therefore, the low-energy DOS of graphene can readily be found as $g_s g_v |E|/2\pi\hbar^2 v_F^2$, where g_s and g_v are the spin and valley degeneracy, respectively.^{10,14,58} The linear energy-dependence of DOS holds up to $E \approx 0.3\gamma_0$, beyond which the DOS increases sharply due to trigonal warping of the band structure at higher energy.¹⁴

Figure 1 compares the basic features of the electronic band structure of graphene with that of conventional 2DEG.¹⁵ In the latter case, the electron is confined in the z direction by electrostatic potentials, leading to the quantization of k_z and thus discrete energy steps. As k_x and k_y still remain as continuous, associated with each energy step is a subband with a parabolic energy dispersion curve. Due to energy quantization, the DOS is now given by a sum of step functions, and between neighboring steps the DOS is constant. In contrast, graphene is a “perfect” 2D system; therefore, there are no subbands emerged from the confinement in the z direction. Furthermore, the single band has a linear energy dispersion in the (k_x, k_y) plane, instead of a parabolic shape as it is in the case of conventional 2D system. Note that quantum wells with a well thickness of one atomic layer have been realized in several material systems; but these systems are fundamentally different from graphene.

B. Effect of a perpendicular magnetic field

The difference in the behavior of graphene and particles with a parabolic spectrum is manifested when an external magnetic field is applied perpendicularly to the plane. We first look at the case of conventional 2DEG system.¹⁵ Let the magnetic vector potential be $\vec{A} = (-By, 0, 0)$ (Landau gauge), the Schrödinger equation is given by

$$\left(\frac{(\hat{p}_x - eB\hat{y})^2}{2m_e} + \frac{\hat{p}_y^2}{2m_e} + \frac{\hat{p}_z^2}{2m_e} + V_0(z) \right) \psi = E\psi, \quad (7)$$

where $V_0(z)$ is the confinement electrostatic potential in z direction and m_e is the electron mass. Substitute the wave function $\psi = e^{i(k_x x + k_z z)} \phi(y)$ into Eq. (7), one obtains

$$\left[\frac{\hat{p}_y^2}{2m_e} + \frac{1}{2} m_e \omega_c^2 (y - y_0)^2 \right] \phi = (E - E_{zn}) \phi$$

where E_{zn} is quantized energy due to confinement in z direction and $y_0 = -\hbar k_x / eB$. The total quantized energy levels, or Landau levels (LLs), are given by

$$E_{nl} = \left(l + \frac{1}{2} \right) \hbar \omega_c + E_{zn}, \quad (8)$$

where $\omega_c = eB/m_e$ is the cyclotron frequency, $n = (1, 2, 3, \dots)$ and $l = (0, 1, 2, 3, \dots)$ are integers and are the indices for quantization in the z direction and LLs, respectively. The area between two neighboring LLs is $\pi(k_{l+1}^2 - k_l^2) = (2m_e \pi \omega_c / \hbar)$; therefore, the degeneracy of one LL is

$$P = \frac{g_s m_e \omega_c L^2}{2\pi\hbar}. \quad (9)$$

In the presence of disorder, the Hall conductivity of 2DEGs exhibits plateaus at $lh/2eB$ and is quantized as $\sigma_{xy} = \pm l(2e^2/h)$,¹⁵ leading to the IQHE.^{61,62}

On the other hand, the low-energy electronic spectrum of electrons in graphene with the presence of perpendicular field is governed by

$$\hbar v_F \sigma \cdot (-i\nabla + e\vec{A}/c) \psi = E\psi \quad (\text{around K point}),$$

$$\hbar v_F \sigma^* \cdot (-i\nabla + e\vec{A}/c) \psi = E\psi \quad (\text{around K' point}). \quad (10)$$

The energy of LLs has been calculated by McClure and is given by^{63,64}

$$E_l = \text{sgn}(l) v_F \sqrt{2e\hbar B |l|}. \quad (11)$$

Here, $|l| = 0, 1, 2, 3, \dots$, is the Landau index and B is the magnetic field applied perpendicular to the graphene plane. The LLs are doubly degenerate for the K and K' points. Compared to the case of conventional 2DEGs, of particular interest is the presence of a zero-energy state at $l=0$ which is shared equally by the electrons and holes. This has led to the observation of so-called anomalous IQHE, in which the Hall conductivity is given by^{7,8}

$$\sigma_{xy} = \pm 2(2l+1) \frac{e^2}{h}. \quad (12)$$

Figure 2 shows the results of quantum Hall effect observed for the first time in graphene by Novoselov *et al.*⁷ The measurement was performed at $B = 14$ T and temperature of 4 K. Instead of a plateau, a finite conductivity of $\pm 2e^2/h$ appears at the zero-energy. The plateaus at higher energies occur at half integers of $4e^2/h$. The result agrees well with Eq. (12). The resistivity at neutral point will be discussed shortly. The $l=0$ LL has also been observed in Shubnikov-de Haas oscillations (SdHOs) at low field,^{7,8} infrared spectroscopy,^{65,66} and scanning tunneling spectroscopy (STS).⁶⁷⁻⁶⁹

C. Electrostatic confinement and tunneling

The difference in behavior between graphene and normal 2D electron system is also manifested in their response to lateral confinement by electrostatic potentials. A further confinement of 2DEGs from one of the lateral directions leads to the formation of quantum wires. For a quantum wire of size L_z and L_y in the z and y direction, the quantized energy levels are given by

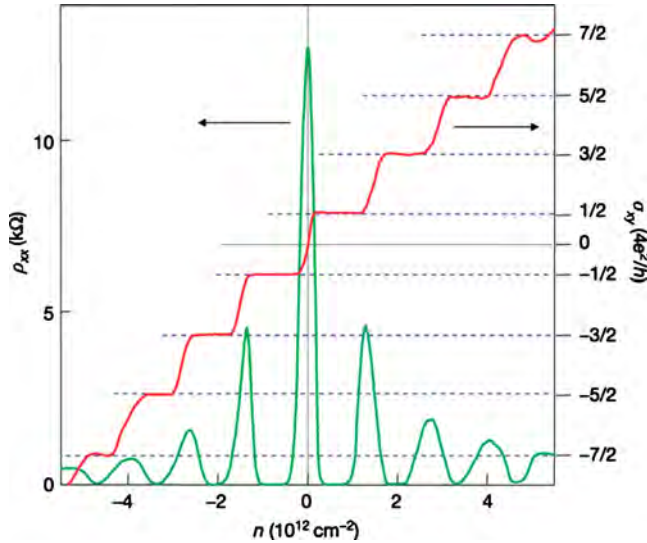


FIG. 2. (Color online) Hall conductivity σ_{xy} and longitudinal resistivity ρ_{xx} of graphene as a function of carrier concentration at an applied magnetic of 14 T and temperature of 4 K. Pronounced QHE plateaus are observed at $(4e^2/h)(l+1/2)$ with the first plateau occurred at $l=0$. Reprinted by permission from Macmillan Publishers Ltd: Nature, Novoselov *et al.*, **438**, 197 (2005), Copyright 2005.

$$E_{n_y, n_z} = \frac{(\hbar k_x)^2}{2m^*} + \frac{\hbar^2}{2m^*} \left(\frac{n_y \pi}{L_y} \right)^2 + \frac{\hbar^2}{2m^*} \left(\frac{n_z \pi}{L_z} \right)^2, \quad (13)$$

where m^* is the effective mass, k_x is the wave vector in x direction, and n_y , n_z are integers. The corresponding DOS is given by

$$\rho(E) = \frac{\sqrt{2m^*}}{\pi \hbar} \sum_{i,j} \frac{H(E - E_{n_y, n_z})}{\sqrt{E - E_{n_y, n_z}}}, \quad (14)$$

where H is the Heaviside function.

The counterpart of nanowire in graphene is the so-called graphene nanoribbon (GNR). In addition to the width, the electronic spectrum of GNR also depends on the nature of its edges, i.e., whether it has an armchair or zigzag shape.⁷⁰ The energy dispersion of GNR can be calculated using the tight-binding method,⁷⁰⁻⁷³ Dirac equation,^{74,75} or first-principles calculations.^{76,77} All these models lead to the same general results, i.e., GNRs with armchair edges can be either metallic or semiconducting depending on their width, while GNRs with zigzag edges are metallic with peculiar edge or surface states. For GNRs with their edges parallel to x axis and located at $y=0$ and $y=L$, their energy spectra can be obtained by solving Eq. (5) with the boundary conditions: $\psi_B(y=0)=0$, $\psi_A(y=L)=0$ at point K and $\psi'_B(y=0)=0$, $\psi'_A(y=L)=0$ at point K', for zigzag ribbons and $\psi_A(y=0)=\psi_B(y=0)=\psi_A(y=L)=\psi_B(y=L)=0$ at point K and $\psi'_A(y=0)=\psi'_B(y=0)=\psi'_A(y=L)=\psi'_B(y=L)=0$ at point K', for armchair ribbons. The eigenvalue equations of the zigzag ribbons near the K point are given by⁷⁴

$$e^{-2\alpha L} = \frac{k_x - \alpha}{k_x + \alpha} \quad \text{and} \quad k_x = \frac{k_n}{\tan(k_n L)}, \quad (15)$$

where $\alpha^2 = (\hbar v_F k_x)^2 - \varepsilon^2$ for real α and $\alpha = ik_n$ for pure imaginary α , ε is the energy calculated from the Fermi level of

graphene. The first equation has a real solution for α when $k_x > 1/L$, which define a localized edge state.⁷⁴ The solution of the second equation corresponds to confined modes due to finite width of the ribbon. The eigenvalues near the K' point can be obtained by replacement, $k_x \rightarrow -k_x$.¹⁴ The localized edge state induces a large DOS at the K and K' which are expected to play a crucial role in determining the electronic and magnetic properties of zigzag nanoribbons.^{70-72,78} In contrast, there are no localized edge states in armchair GNRs. The wave vector across the ribbon width direction is quantized by $k_n = (n\pi/L) - (4\pi/3\sqrt{3}a)$ and the energy is given $\varepsilon = \pm \hbar v_F [k_x^2 + k_n^2]^{1/2}$.¹⁴ Here, n is integer. The armchair nanoribbons will be metallic when $L = 3\sqrt{3}na/4$ and semiconducting in other cases.

Although the chiral electrons in graphene can be effectively confined in nanoribbons through the boundaries, they cannot be confined effectively by electrostatic potential barriers in the same graphene. For a 1D potential barrier of height V_0 and width D in x direction, the transmission coefficient of quasiparticles in graphene is given by^{14,16}

$$T(\phi) = \frac{\cos^2(\theta)\cos^2(\phi)}{[\cos(Dq_x)\cos\phi\cos\theta]^2 + \sin^2(Dq_x)(1 - ss'\sin\phi\sin\theta)^2}, \quad (16)$$

where $q_x = \sqrt{(V_0 - E)^2 / (\hbar v_F)^2 - k_y^2}$, E is energy, k_y is the wave vector in y direction, $\phi = \tan^{-1}(k_y/k_x)$ and $\theta = \tan^{-1}(k_y/q_x)$. The transmission coefficient becomes unity when (i) $Dq_x = n\pi$ with n an integer, independent of the incident angle and (ii) at normal incidence, i.e., $\phi=0$. In these two cases, the barrier becomes completely transparent, which is the manifestation of Klein tunneling.^{16,17} Stander *et al.*¹⁸ have found evidence of Klein tunneling in a steep gate-induced potential step, which is in quantitative agreement with the theoretical predictions. Signature of perfect transmission of carriers normally incident on an extremely narrow potential barrier in graphene was also observed by Young and Kim.⁷⁹ Very recently, Klein tunneling was also observed in ultraclean CNTs with a small band gap.⁸⁰ On the other hand, Dragoman has shown that both the transmission and reflection coefficients at a graphene step barrier are positive and less than unity;⁸¹ therefore it does not support the particle-antiparticle pair creation mechanism predicted by theory. Further concrete evidences are required to verify the Klein paradox in graphene system.

Figure 3 summarizes graphene and normal electron systems under an external magnetic field [(a) and (d)], in ribbon and wire form [(b) and (e)] and with a 1D potential barrier [(c) and (f)]. The fundamental properties of graphene summarized in Figs. 1 and 3 lead to peculiar electronic, magnetic, and optical properties. In what follows, we give an overview of electrical transport properties which have more experimental results to support the theoretical predictions.

III. ELECTRICAL TRANSPORT PROPERTIES OF GRAPHENE

Due to its unique band structure, graphene exhibits several peculiar electronic properties which are absent in conventional 2DEGs.^{14,15} Among those which have been inves-

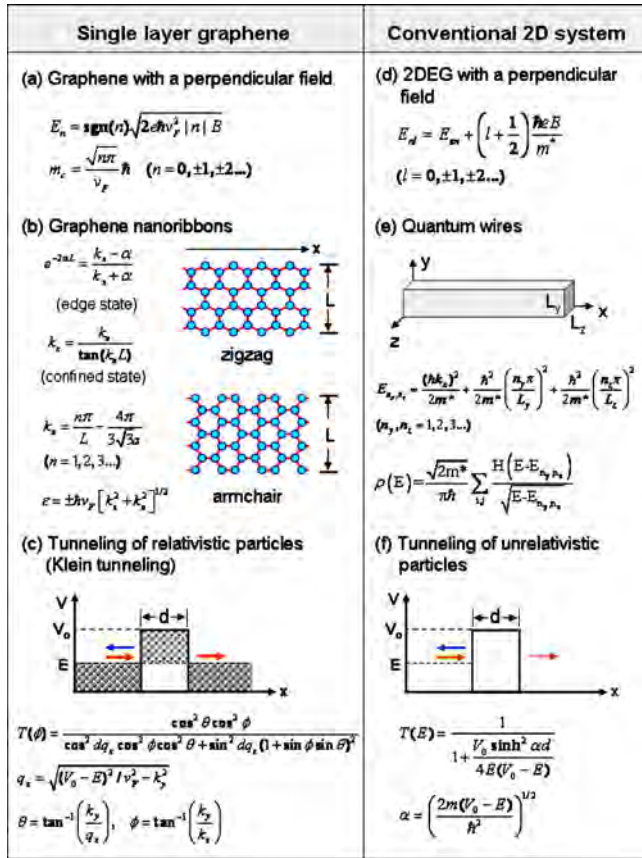


FIG. 3. (Color online) Comparison of graphene and normal electron systems under an external magnetic field [(a) and (d)], in ribbon and wire form [(b) and (e)] and with a 1D potential barrier [(c) and (f)].

tigated most intensively include WAL,^{7,25–27,59,82} minimum conductivity,^{7,8,23,83,84} carrier density dependence of conductivity,^{24,85–88} etc. In what follows, we review briefly the recent progresses made in these aspects.

A. Weak (weak-anti) localization

In a weakly disordered system, there are generally two types of scattering events which affect the electron transport processes: elastic and inelastic scattering. In the former case, the electron energy does not change; therefore, its phase evolution can be traced. In the second case, however, the electron “forgets” its phase after scattering. The probability for electron to lose its phase memory is the inverse of the phase relaxation time τ_ϕ . When $\tau_\phi \gg \tau$, where τ is the momentum relaxation time, quantum interference between self-returned and multiply scattered paths of electrons on the scale of phase coherence length, $L_\phi = v_F \tau_\phi$, leads to quantum interference corrections (QICs) to the electrical resistance, which manifests itself in the form of weak localization (WL).^{89,90} In 2D disordered metals, the quantum correction to conductivity is given by $\Delta\sigma_{2D} = -(2e^2/h) \ln((L_\phi/\lambda))$, where λ is the mean-free path. An applied magnetic field starts to break the WL at $B > B_\phi = (\hbar/eL_\phi^2)$ due to the additional loop area dependent phase acquired by electrons traveling in different directions. Therefore, the WL is usually accompanied with a negative magnetoresistance (MR) effect. In addition to an external magnetic field, the WL can also be

destroyed by scattering with magnetic impurities and strong spin-orbit coupling, which flips the spins along the path of electron transport.

Due to the relativistic and chiral nature of electrons in graphene, the WL in this perfect 2D system is expected to be affected by not only inelastic and spin-flip processes but also a number of elastic scattering processes.^{25,26,82} In graphene, the envelope wave function of electrons around the K point is given by Eq. (6), i.e., $\psi(\vec{k}) = (1/\sqrt{2}) \begin{pmatrix} e^{-i\theta_{\vec{k}}/2} \\ e^{i\theta_{\vec{k}}/2} \end{pmatrix}$, here, $\theta_{\vec{k}} = \tan^{-1}((k_y/k_x))$. The overlapping between wave functions $\psi(0)$ and $\psi(\theta_{\vec{k}})$ is $|\langle \psi(\theta_{\vec{k}}) | \psi(0) \rangle|^2 = \cos^2(\theta_{\vec{k}}/2)$, leading to a suppression of intravalley backscattering (long-range scatters), or the appearance of WAL.^{25,59} The WL will be restored by both intervalley and intravalley scatterings. If the former is dominant, whether a WL and WAL will be observed in an actual graphene sample depends strongly on the ratio between two characteristic times: τ_ϕ and the intervalley scattering time, τ_{iv} . The WL is expected to occur when $\tau_\phi \gg \tau_{iv}$, and WAL occurs when $\tau_\phi \ll \tau_{iv}$.²⁵ The intervalley scattering can be induced by atomically sharp defects or edges in narrow ribbons. As it has been shown by McCann *et al.*²⁶ and Morpurgo and Guinea,⁸² the phase coherence time τ_ϕ and intervalley scattering time τ_{iv} are not the only parameters that determine the quantum transport in graphene. The quantum interference within each valley can be affected by trigonal warping and scattering that breaks the chirality of electrons. Such scattering centers include long-range distortions induced by lattice disclinations and dislocations, nonplanarity of the graphene layers, and slowly varying random electrostatic potentials that break the symmetry between the two sublattices of graphene. All these types of defects are realistically present in real graphene samples; therefore, large differences in the quantum correction to the conductivity measured on different samples should be expected.⁸² Yan and Ting⁹¹ studied the WL effect in graphene under the presence of charged impurities using the self-consistent Born approximation. This model is considered more realistic than the zero-range potential model. It was found that the QIC to conductivity is dependent on sample size, carrier concentration and temperature. The WL is present in large size samples at finite carrier doping and its strength becomes weakened or quenched in a wide temperature range when the sample is below a certain critical size (about a few microns at low temperature). Near the zero-doping region, the QIC becomes mostly positive regardless of the sample size, indicating that the electrons become delocalized.

The suppression of WL was observed in the very first experiment on graphene by Novoselov *et al.*⁷ Subsequently, Morozov *et al.* measured the MR of SLG flakes of several microns in size placed on top of SiO₂ (300 nm)/Si substrate.²⁷ The negative MR measured was typically two orders of magnitude smaller than that expected for metallic samples having a similar range of resistivity, indicating a strong suppression of WL. The authors ruled out both a short phase-breaking length and magnetic impurities as possible mechanisms for the WL suppression, and instead they attributed the unexpected behavior to the existence of mesoscopic corrugations in graphene sheets, which induce a nominal ran-

dom magnetic field. Wu *et al.*²⁹ have observed WAL in epitaxial graphene grown on carbon rich SiC(0001) surface.

Tikhonenko *et al.*²⁸ have shown that the WL in graphene exists in a large range of carrier density, including the Dirac region. The authors attributed this to the significant intervalley scattering. It is argued that total suppression of WL is only possible in experiments where intervalley scattering is negligible, i.e., in very large samples without sharp defects in the bulk. Similar results have also been observed in bilayer graphene, i.e., the WL is observed at different carrier densities including the Dirac point.⁹² In a recent paper from the same group, it was shown that transition between WL and WAL can occur in the same sample, depending on the measurement conditions. The WAL prevails over WL at high temperature and low carrier density.⁹³ The results are in good agreement with the theoretical predictions.²⁶

B. Electrical conductivity and mobility of graphene

Although the DOS of graphene at the Dirac point is zero, it exhibits a minimum conductivity of order of e^2/h even at the lowest temperature possible.^{7,8} Away from the Dirac point, it was found that the graphene conductivity is linear in the concentration of carriers (subtracting the residual carriers at half filling).^{7,8} Miao *et al.*⁸³ measured the conductivity of graphene at the Dirac point, on samples with different width (W) to length (L) ratio and surface areas (A). It was found that, for devices with relatively large length ($L > \sim 1 \mu\text{m}$) and large area ($A > 3 \mu\text{m}^2$), the values of minimum conductivity are geometry-independent and relatively constant: ~ 3.3 to $4.7 \times (4e^2/\pi h)$. For “small” devices with $L < 500 \text{ nm}$ and $A < 0.2 \mu\text{m}^2$, a qualitatively different behavior was observed, depending on the aspect ratio W/L . The minimal conductivity decrease from $\sim 4 \times 4e^2/\pi h$ at $W/L = 1$ to $\sim 4e^2/\pi h$ at $W/L = 4$, beyond which it saturates at this value. Similar results have also been observed by Daneau *et al.*⁸⁴ on samples with large W/L ratios and small L ($= 200 \text{ nm}$). In addition, a finite and gate dependent Fano factor reaching the universal value of $1/3$ was also observed at the Dirac point, which supports the transport via evanescent waves theory.⁹⁴

These results agree well with theoretical predictions that, in the ballistic regime, the minimal conductivity depends on the graphene’s geometry and the microscopic details of the edges, approaching the value of $4e^2/\pi h$ when boundary effects are negligible, i.e., in samples with a large W/L ratio.⁹⁴ These theoretical models predict that, in perfect graphene (i.e., at the clean limit) and at the Dirac point, the electrical conduction occurs only via evanescent waves, i.e., via tunneling between the electrical contacts.^{94,95} As it is summarized recently by Ziegler,²³ depending on whether the Kubo formula or Landauer formula or both of them are used, the theoretically calculated value of minimal conductivity varies from $(1/\pi)(e^2/h)$,^{94–101} to $(\pi/8)(e^2/h)$ (Refs. 96 and 99) and $(\pi/4)(e^2/h)$ (Refs. 102 and 103) per valley and per spin channel. Ziegler showed that all these values can be obtained from the standard Kubo formula of nearly ballistic quasiparticles by taking limits in different order.²³ Various models

have been proposed to account for the difference between theoretical and experimental values of minimal conductivity.

For samples which are not at the clean limit, the minimal conductivity is affected by scattering associated with several different types of scattering centers such as impurities, defects, and phonons.²⁴ In addition to these conventional scattering centers, ripples also affect electrical transport in graphene. Both the ripples and charged impurities in the substrate on which the graphene is placed are known to induce electron-hole puddles at low carrier concentration.^{24,85} These puddles have been observed experimentally for graphene samples on SiO_2/Si substrates with a characteristic dimension of approximately 20–30 nm.^{104,105} From Einstein relation between conductivity and compressibility, a minimal conductivity of the order of $4e^2/h$ is deduced at the Dirac point, which is π times higher than that of the minimal conductivity at the clean limit. Chen *et al.*¹⁰⁶ have investigated the effect of doping on the conductivity of graphene through controlled doping of potassium in ultrahigh vacuum. It was found that the minimal conductivity only decreases slightly with increasing the doping concentration, although there is a significant decrease in mobility. These results suggest that charge inhomogeneity is responsible for the minimal conductivity obtained experimentally. The former is considered being caused by the charged impurities either inside the substrate or in the vicinity of graphene.

The charged impurities are also responsible for the linear dependence of conductivity on the carrier concentration away from half-filling.^{24,85–88} Ostrovsky *et al.*¹⁰⁰ showed that the transport properties of the system depend strongly on the character of disorder; both the strength and type of disorder play an important role in determining the conductivity. Away from the Dirac point, the conductivity exhibits a linear relationship with the carrier concentration in the case of strong scatters, while a logarithmic relationship is found for the case of weak scatters. Ando demonstrated that the conductivity of graphene limited by charged-impurity scattering increases linearly with the electron concentration and the mobility remains independent of the Fermi energy.⁸⁶ It is also shown that the increase in screening with temperature at sufficiently high temperatures leads to the mobility increase proportional to the square of temperature. Hwang *et al.*⁸⁵ have developed a detailed microscopic transport theory for graphene by assuming that charged impurities in the substrate are the dominant source of scattering. It was shown that, away from the Dirac point and at high carrier density, the electrical transport can be accounted for well by the Boltzmann transport theory, which results in a conductivity that scales linearly with n/n_i , where n is the carrier density and n_i is the impurity distributed randomly near the graphene/substrate interface. For samples with either a large carrier density or low charge-impurity concentration, short-range scattering by point defects or dislocations would dominate the transport, which leads to sublinear σ - n curves. The theoretical models explain well most of the experimental observations.^{7,85,106,107}

Removing substrate or using high- κ dielectrics are two possible ways to reduce the scattering from charged impurities.^{30,32,108–111} From a suspended graphene sheet, Du

*et al.*³² obtained a mobility value as high as $200\,000\text{ cm}^2\text{ V}^{-1}\text{ s}^{-1}$ for carrier densities below $5 \times 10^9\text{ cm}^{-2}$. The minimum conductivity at low temperature was found to be $1.7(4e^2/\pi h)$ for a sample with $L=0.5\text{ }\mu\text{m}$ and $W=1.4\text{ }\mu\text{m}$, which is higher than the theoretical value of $4e^2/\pi h$ for ballistic transport at the clean limit. Nevertheless, the sharp change in conductivity with bias voltage suggests that the electrical transport in short and suspended graphene sheets approaches the ballistic regime. Bolotin *et al.*¹⁰⁸ have investigated the effect of impurity absorbed on the surface of suspended graphene on its electrical transport properties. It was found that, for “dirty” samples, the mobility is low ($28\,000\text{ cm}^2/\text{V s}$) even when it is suspended from the substrate. However, the mobility increases significantly after the sample was cleaned *in situ* in UHV so as to obtain ultraclean graphene. For these samples, a mobility as high as $170\,000\text{ cm}^2/\text{V s}$ has been obtained below 5 K. The resistivity of ultraclean graphene is found to be strongly dependent on temperature in the temperature range of 5–240 K. At large carrier densities, $n > 0.5 \times 10^{11}\text{ cm}^{-2}$, the resistivity increases with increasing the temperature and becomes linear with temperature above 50 K, suggesting that scattering from acoustic phonons dominates the electrical transport in ultraclean samples. From the temperature-dependence of a non-universal conductivity at the charge neutral point, a carrier density inhomogeneity of $< 10^8\text{ cm}^{-2}$ is estimated.

If the enhancement of mobility in suspended graphene is due to the removal of charged impurities from the substrate, different values of mobility would be obtained by replacing SiO_2 with other dielectrics. To this end, Ponomarenko *et al.*¹¹¹ have studied graphene devices placed on a number of different substrates, including SiO_2 , polymethylmethacrylate, spin-on glass, bismuth strontium calcium copper oxide, mica, and boron nitride. But the mobility found is almost the same as that of typical graphene devices placed on SiO_2 . Similarly, only a small change in mobility ($< 30\%$) has been obtained by covering the device with glycerol ($\kappa \approx 45$), ethanol ($\kappa \approx 25$), or water ($\kappa \approx 80$). Further studies are required to understand the different results obtained in suspended samples and samples with different dielectric environment.

IV. SYNTHESIS OF 2D CARBON NANOSTRUCTURES

The first step toward the study of any material system is to establish techniques for large scale synthesis of the material with controlled quality and at a reasonable cost. Due to the layered nature of graphite, the most straightforward way to obtaining 2D carbon is to use the exfoliation technique to “peel” off carbon layer-by-layer from graphite.^{7,8} The exfoliation can be performed either mechanically or chemically,⁴⁰ or the combination of both techniques. On the other hand, as is with any other type of material, 2D carbon can also be grown using both physical and chemical synthesis techniques. The main approaches reported so far include arc discharge,¹¹² CVD,⁴² epitaxial growth,³⁶ reduction from GOs,⁴⁰ etc. Although none of these is really a new technique, they have been revisited, rediscovered, and improved dramatically in the last few years since the discovery of

graphene. In this section, we review these synthesis techniques by including both SLG and MLG sheets (or nanowalls).

A. Exfoliation

Exfoliation of graphite can be considered as the reverse process of stacking graphene into graphite. The stacking process is the result of chemical bonding between adjacent graphene sheets. The lowest energy and thus most common stacking is Bernal stacking, in which adjacent graphene sheets are rotated with an angle of 60° relative to each other about the stacking axis. This results in the formation of two sublattices of atoms. For the sublattice consisting of A atoms, for every A atom there is another A atom positioned in the adjacent sheet below, whereas for the other sublattice consisting of B atoms, there are no respective B atoms below them in the adjacent sheet. The intersheet spacing in the stacking direction (or c direction) is 3.354 \AA . The adjacent sheets are bonded through the overlap of partially filled p_z (or π) orbitals perpendicular to the plane, also known as van der Waals force. Due to the large lattice spacing and weak bonding in the c direction as compared to the small lattice spacing and much stronger σ bonding in the hexagonal lattice plane, it has long been tempting to obtain graphene sheets through exfoliation of graphite. Experimentally, exfoliation of graphite has been investigated and realized by using various techniques, including chemical/solution, mechanical, and thermal methods.

1. Mechanical exfoliation

Due to the weak bonding between adjacent graphene sheets in graphite, graphene sheets of different thicknesses can be readily obtained through mechanical exfoliation, or peeling off, of different types of graphitic materials, including Kish graphite (single crystal graphite flakes), highly ordered pyrolytic graphite (HOPG), and natural graphite, etc. Mechanical exfoliation of graphite may happen naturally in many processes such as simply rubbing graphite against a foreign substance, just as writing using a pencil. However, the most recent work with a clearly defined purpose perhaps originates from peeling and manipulation of graphene sheets using atomic force microscopy (AFM) or STM tips.^{113–118} Hiura *et al.*¹¹³ and Ebbesen and Himura¹¹⁴ observed folding and tearing of graphitic sheets which formed spontaneously during scanning due to the friction between the tip and HOPG surface (Fig. 4). It was found that the folding and tearing of graphitic sheets follow well-defined patterns due to the formation of sp^3 -like line defects in the sp^2 graphitic network, occurring preferentially along the symmetry axes of graphite. The curved portion is accompanied with ripples, in order to release the strain and stabilize the electronic structure in the bent region. The possibility of creating various types of 3D graphene structures through folding and re-folding of graphene sheets in different ways has been discussed.¹¹⁴ Instead of forming graphene sheets spontaneously during tip scanning on HOPG, Roy *et al.*^{116,117} has tried to fold and unfold the graphene sheets in a more controllable way through modulating the distance or bias voltage

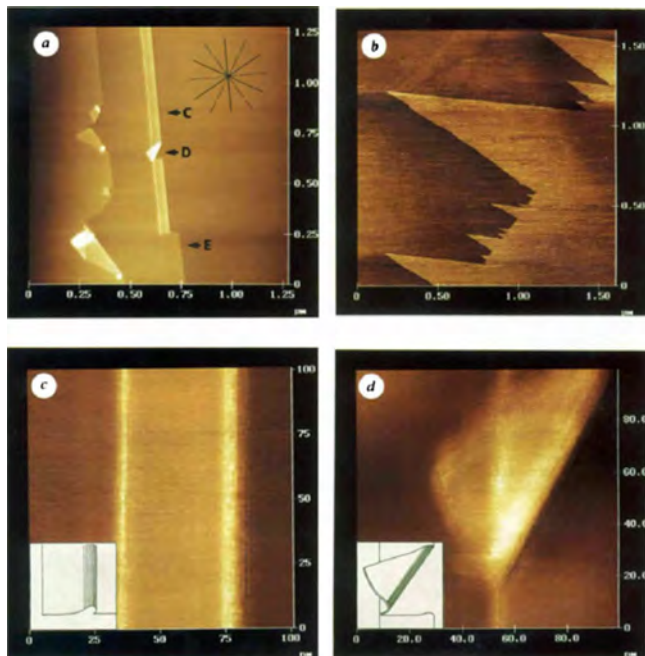


FIG. 4. (Color online) AFM images HOPG. [(c) and (d)] Are the high-magnification images of the portions indicated in (a) as C and D, respectively. Reprinted by permission from Macmillan Publishers Ltd, Nature, Hiura *et al.*, **367**, 148 (1994), Copyright 1994.

between the tip and sample when scanning selected areas. Energetic considerations suggested that the folding/unfolding process can be accounted for by the tip-sample vibration.

In all these experiments, one must first locate step edges using AFM over a large sample surface area and thus the entire process is not well-controlled. Furthermore, it is also difficult to obtain large size graphene sheets using this method. An improvement over these early works was to first pattern the graphite into small islands, followed by tearing using the AFM or STM tip.¹¹⁸ The patterning of HOPG into islands of 2–40 μm was achieved through the combination of a 200-nm-thick SiO_2 mask and oxygen plasma etching. The subsequent manipulation using AFM tip results in the displacement of graphite plates from the original island. The thickness of the graphite plates obtained in this work was about 100 nm (Fig. 5). Zhang *et al.*¹¹⁹ succeeded in reducing the graphite plate thickness by first transferring the detached graphite island to a micromachined silicon cantilever, and then use the mounted graphite block on the cantilever as the tip of an AFM to scan it over a SiO_2/Si substrate. By doing so, graphite plates with a thickness of 10 to 100 nm have been obtained. These thin graphite plates were found to exhibit clear field-effect.

Instead of attaching the graphite island onto the cantilever, Novoselov *et al.*⁶ pressed patterned HOPG square mesas (5 μm in height and 20 μm to 2 mm in lateral size) against a 1- μm -thick layer of a fresh wet photoresist spun over a glass substrate. After baking, the mesas were cleaved off the HOPG sample and attached to the photoresist layer. The subsequent repeated peeling using a scotch tape led to only thin flakes left in the photoresist. These flakes were then released in acetone. When a SiO_2 (~ 300 nm)/ Si (n^+ -doped) wafer was dipped in the solution and then washed in water and

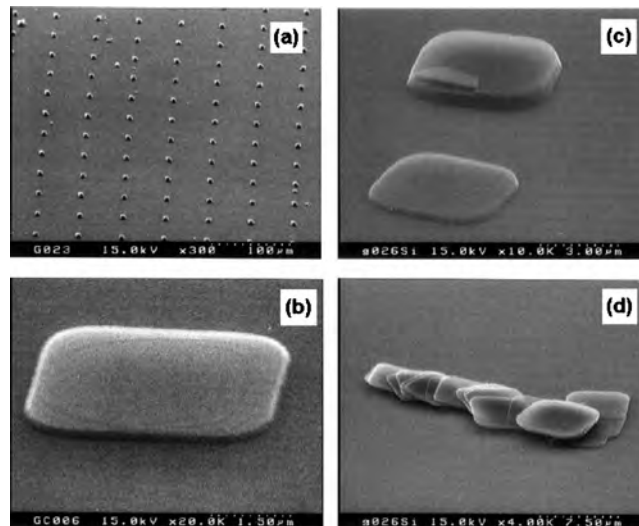


FIG. 5. Scanning electron micrographs of (a) and (b) HOPG islands, and (c) and (d) HOPG plates on $\text{Si}(001)$ substrates. Reprinted with permission from X. Lu *et al.*, *Nanotechnology* **10**, 269 (1999), Copyright 1999, IOP Publishing Ltd.

propanol, some flakes became captured on the wafer's surface. The thick flakes were further removed through ultrasound cleaning in propanol. Thin flakes ($d < 10$ nm) were found to attach strongly to SiO_2 , presumably due to van der Waals and/or capillary forces. By using this method, graphene sheets as thin as one atomic layer have been obtained (Fig. 6). Ever since this work, mechanical exfoliation has become the method of choice for producing graphene with highest quality. Many variations in original exfoliation techniques have been developed and applied to different types of graphites. Although the mechanical exfoliation technique has been improved significantly, its primary drawbacks still remain. Its low-productivity does not allow synthesis of graphene in large quantities. It is also incompatible with standard Si processes. The former might be overcome by chemical exfoliation and CVD, while the latter may be avoided by using epitaxial growth.

2. Chemical exfoliation

Like mechanical exfoliation, chemical exfoliation of graphite is also an old technique. The primary advantage of

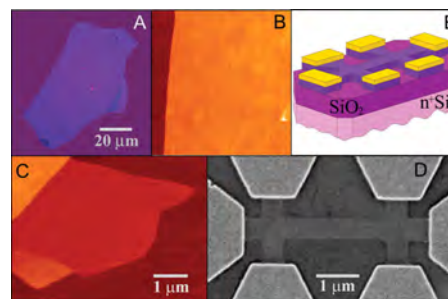


FIG. 6. (Color online) Graphene films obtained by mechanical exfoliation. (a) Photograph of a graphene flake with a thickness of 3 nm placed on top of an oxidized Si wafer. (b) AFM image of a $2 \times 2 \mu\text{m}^2$ area of the flake in (a) near its edge (dark brown, SiO_2 surface; orange, 3 nm height above the SiO_2 surface). (c) AFM image of SLG (central area). (d) SEM image of a few layer graphene device (e) Schematic view of the device in (d). From Novoselov *et al.*, *Science* **306**, 666 (2004), Reprinted with permission from AAAS.

chemical exfoliation over the mechanical approach lies in its high-yield and scalability. The chemical exfoliation is generally accomplished in two process steps. The first step is to enlarge the interlayer spacing between graphene sheets by forming graphite intercalated compounds (GICs).^{120,121} The GICs can be formed in many different forms, depending on the types of the intercalants,¹²¹ although not all of them are suitable for the subsequent exfoliation process. One of the popular methods to form GICs for exfoliation purpose is to soak graphite for an extended period of time in mixtures of sulfuric and nitric acid.^{122,123} After an appropriate duration of soaking, the acid molecules penetrate into the graphite, forming alternating layers of graphite and intercalant. The thickness of the graphite layers decreases with time, with a possibility down to a few layers, though the yield of obtaining few layer graphene sheets is typically quite low. After the intercalation, the second step is to exfoliate the thin graphite sheets via rapid evaporation of the intercalants at elevated temperature. The extent of exfoliation can be further enhanced by subjecting the thermal annealed GICs to treatments like ball milling and ultrasonication.^{123–125} Although this technique is simple, the graphite nanoplatelets obtained via this method usually exhibit thicknesses ranging from a few to a few hundreds of layers.¹²³ In order to obtain SLG sheets, the intercalation and exfoliation processes have to be repeated by using different intercalating and exfoliating chemistry and processes.^{126,127} Alternatively, one can also oxidize the graphite completely to form GOs.^{128,129} The GOs can be subsequently exfoliated to form very thin GO sheets using different techniques.¹³⁰ A chemical, thermal, or electrochemical reduction process is then followed to convert the GOs into graphene sheets.^{131–133} Some typical experiments are described below.

Aiming at obtaining SLG sheets, Horiuchi and co-workers have developed a two-step process to obtain, what they called, carbon nanofilms.^{134,135} The first step was to oxidize the graphite using the Hummer's method, in which natural graphite particles were immersed in a mixture of H_2SO_4 , NaNO_3 , and KMnO_4 to obtain GICs (or GOs). In the next step, the GOs were hydrolyzed to introduce the hydroxyl and ether groups into the intergraphene layer spaces, after which each GO layer became a multiply charged anion with a thickness of approximately 0.6 nm. When the excess small ions from the oxidants were removed by a purification process, the GO sheets automatically separated from each other due to interlayer electrostatic repulsion. The resulting GO layers formed a stable dispersion in water. By using this process, Horiuchi *et al.*¹³⁴ succeeded in obtaining SLG sheets.

Ruoff and co-workers developed a series of processes involving the complete exfoliation of GOs into individual GO sheets followed by their *in situ* reduction to obtain single graphene layers.^{131,136} The process began with the oxidation of graphite using the Hummers method.¹²⁹ The GOs are strongly hydrophilic due to the attachment of epoxide and hydroxyl groups to the basal planes and carbonyl and carboxyl groups at the edges. This makes GOs readily intercalated with water molecules. The GOs thus obtained are GICs with both covalently bound oxygen and noncovalently bound water molecules as the intercalants. Rapid thermal treatment

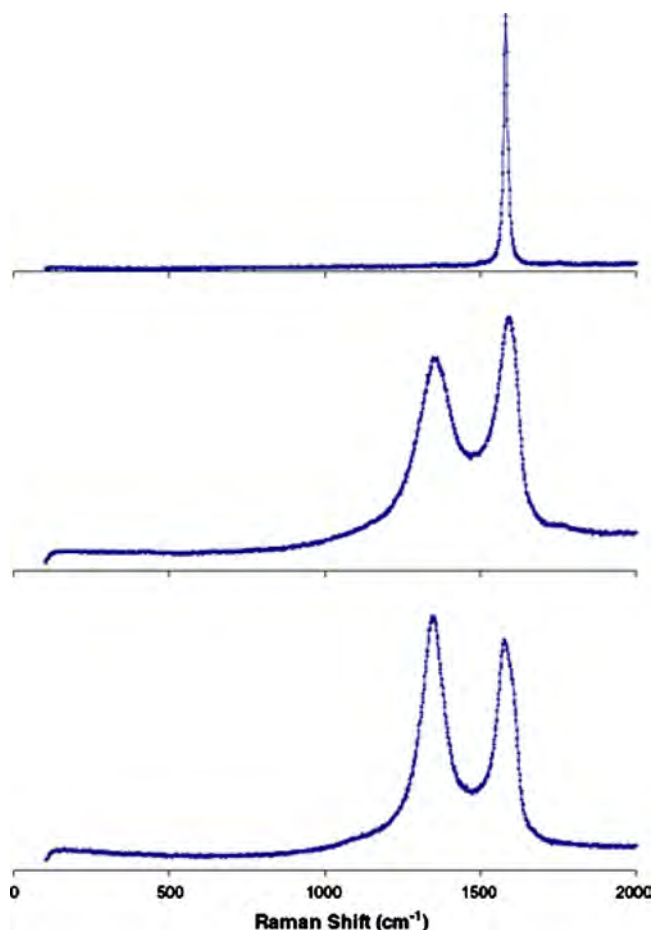


FIG. 7. (Color online) Raman spectra of pristine graphite (top), GO (middle), and the reduced GO (bottom). Reprinted from Stankovich *et al.*, *Carbon* 45, 1558 (2007), Copyright 2007, with permission from Elsevier.

of the GOs results in rapid evaporation of the water molecules at about 100 °C and thermal pyrolysis of oxygen-containing functional groups 250 °C, which in turn help to exfoliate GOs efficiently into individual functionalized graphene sheets. The exfoliated GO sheets were dispersed in water and reduced to graphene sheets by hydrazine reduction. Although the electrical conductivity of reduced GO sheets was found to be five orders of magnitude better than the original GO sheets, it is still ten times lower than that of pristine graphite powders at about 10% of the bulk density. In fact, the electrical transport of reduced GO sheets was found to be dominated by hopping.¹³⁷ This indicates that the reduced graphene sheets likely consist of highly conducting graphene islands cross-linked by nonconductive regions. Raman spectroscopy reveals that the reduced GO sheets are highly disordered.^{131,137–139} Figure 7 shows the typical Raman spectra of pristine graphite, GO and reduced GO.¹³¹ The Raman spectrum of the pristine graphite displays the well-established G peak as the only feature at 1581 cm^{-1} . The G peak is broadened and shifted to 1594 cm^{-1} in GO. In addition, a strong D band appears at 1363 cm^{-1} , indicating the reduction in size of the in-plane sp^2 domains or introduction of disorders during the oxidation process. The Raman spectrum of the reduced GO is also dominated by the G and D bands (at 1584 cm^{-1} and 1352 cm^{-1} , respectively). The D/G

intensity ratio increases as compared to that in GO. This change suggests a further decrease in the average size of the sp^2 domains and increase in defect density or degree of disorder upon reduction in the GO.

The proposed structures of GO and reduced GO have been confirmed recently by Mkhoyan *et al.*¹⁴⁰ using composition sensitive annular dark-field imaging of single and multilayer GO sheets and electron energy-loss spectroscopy for measuring the fine structure of C and O K-edges in a STEM. The results revealed that the GO sheets exhibit an average roughness of 0.6 nm and the structure is predominantly amorphous due to distortions of sp^2 bonds into sp^3 C–O bonds. These works suggest that, in addition to the removal of oxygen, restoration of the sp^2 bonds is necessary if high mobilities are to be achieved in reduced graphene sheets from GOs. The reduced GOs may find applications in areas which high mobility is not so critical such as transparent conductive thin films^{141,142} or composite materials.^{143–145} According to Boukhvalov and Katsnelson and the references therein,^{146–150} the experimentally obtained chemical composition of GO varies in a large range, from $C_8H_{2.54}O_{3.91}$ (Ref. 147) to $C_8H_{4.61}O_{6.70}$,¹⁴⁷ $C_8H_{1.20-1.60}O_{3.12-3.92}$,¹⁴⁸ $C_8-(OH)_{1.38-1.64}O_{0.63-0.79}$,¹⁴⁹ and $C_{12}HO_2$ to $C_{15}H_3O_4$.¹⁵⁰ Based on density functional calculations, Boukhvalov and Katsnelson¹⁴⁶ demonstrated that it is difficult to obtain pure graphene through reduction in GO.

Regardless of the types of applications, another common challenge of using chemically derived graphene sheets is how to prevent agglomeration after the reduction from GOs. In this aspect, a few methods have been developed to create colloidal suspensions of graphene sheets. All these methods are based on controlled charging of the graphene sheets during or after the reduction process, including reduction in GOs under basic conditions,¹⁵¹ hydrazine reduction in KOH-modified graphene oxides,¹⁵² or introducing sulfonic acid groups in partially reduced graphene oxides.¹⁵³

In order to reduce the disorder and defects, several non-oxidation and reduction based methods have been reported. Viculis *et al.*¹²⁶ reported the synthesis of graphite nanoplatelets with thicknesses down to 2–10 nm by using acid-intercalated graphite (Cornerstone, Inc., Wilkes-Barre, PA) as the starting material, reintercalating it with the alkali metals followed by ethanol exfoliation and microwave drying. The reintercalation was performed either by heating graphite and potassium or cesium at 200 °C, or at room temperature using a sodium–potassium alloy. Exfoliation was achieved by the reaction with ethanol. The final process of microwave radiation helps to dry and results in further separation of the sheets. Figure 8 shows the scanning electron micrographs of (a) starting graphite, (b) after intercalation with potassium and exfoliation with ethanol, and (c) and (d) graphite nanoplatelets after further exfoliation induced by microwave radiation. The scale bars in Fig. 8 are 10 μm , 20 μm , 1.67 μm , and 273 nm, respectively. Figure 8(d) shows platelets with a thickness of 10–15 nm, which corresponds to approximately 30–40 layers of graphite. Hernandez *et al.*¹⁵⁴ have demonstrated that graphene dispersions with concentrations up to 0.01 mg ml^{-1} can be produced by dispersion and exfoliation of graphite in organic solvents such as

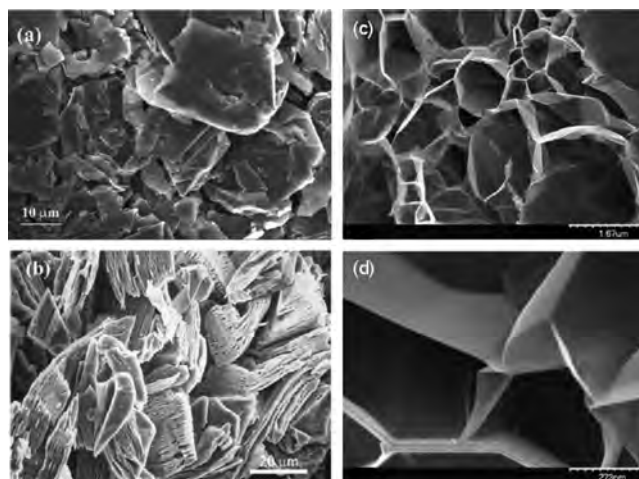


FIG. 8. Scanning electron micrographs of (a) starting graphite, (b) after intercalation with potassium and exfoliation with ethanol, and (c) and (d) graphite nanoplatelets after further exfoliation induced by microwave radiation. The scale bars in Fig. 8(a)–8(d) are 10 μm , 20 μm , 1.67 μm , and 273 nm, respectively. These figures are re-arranged from L. M. Viculis *et al.*, *Mater. Chem.* **15**, 974 (2005). Reproduced by permission of the Royal Society of Chemistry.

N-methylpyrrolidone, γ -butyrolactone, and 1,3-dimethyl-2-imidazolidinone by sonication of graphite powders. The exfoliation is made possible by using solvents whose surface energy matches that of graphene. The existence of almost defect-free SLG and bilayer graphene has been confirmed by TEM, electron diffraction, and Raman, and x-ray photoelectron spectroscopies.

Li *et al.*¹²⁷ successfully obtained GNRs by first heating commercial expandable graphites (made by intercalating $\sim 350 \mu\text{m}$ scale graphite flakes with sulfuric acid and nitric acid) at 1000 °C in a forming gas (3% hydrogen in argon) for 1 min and then sonicating the resulting exfoliated material in a 1,2-dichloroethane solution of poly(mphenylenevinylene-co-2,5-dioctoxy-p-phenylenevinylene) (0.1 mg/ml) to disperse and break up the graphenes into small graphene sheets and ribbons. The subsequent centrifugation process retains the nanoribbons together with small sheets in the supernatant and removes other materials including large graphene pieces and not fully exfoliated graphite flakes. It was found that only $\sim 0.5\%$ of the starting material was retained in the supernatant, and majority of the material remained in many layer structures that were heavy and removed by centrifugation. Figure 9 shows GNRs down to sub-10-nm width, which have been subsequently used to fabricate field-effect transistors (FETs) with on-off ratios of about 10^7 at room temperature. In a recent work, the same group reported a significant improvement in the yield by first exfoliating commercial expandable graphite (160–50 N, Grafguard) via heating it to 1000 °C in a forming gas for 1 min, then grounding the exfoliated graphite and reintercalating it with oleum, followed by inserting tetrabutylammonium hydroxide (TBA, 40% solution in water) into the oleum-intercalated graphite in N,N-dimethylformamide (DMF). The sonication of TBA-inserted oleum-intercalated graphite in a DMF solution of 1,2-distearoyl-sn-glycero-3-phosphoethanolamine-N-[methoxy(polyethyleneglycol)-

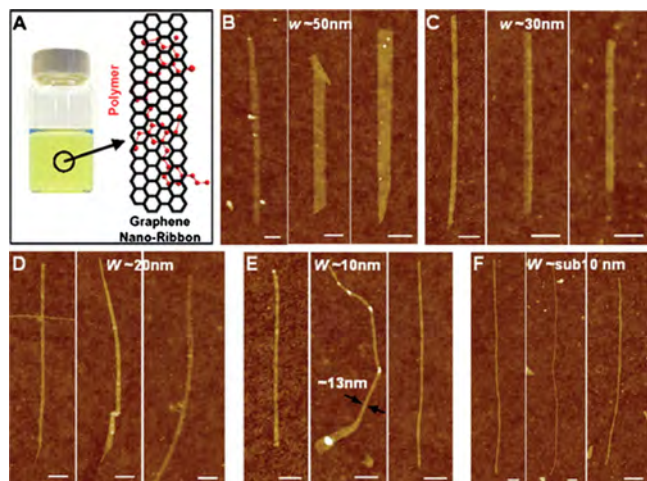


FIG. 9. (Color online) Chemically derived GNRs down to sub-10-nm width. (a) (Left) Photograph of a polymer PmPV/DCE solution with GNRs stably suspended in the solution. Right: schematic drawing of a GNR with two units of a PmPV polymer chain adsorbed on top of the graphene via π stacking. (b) to (f) AFM images of selected GNRs with widths in the 50 nm, 30 nm, 20 nm, 10 nm and sub-10-nm regions, respectively. In (b), left ribbon height ~ 1.0 nm, one layer; middle ribbon height ~ 1.5 nm, two layers; right ribbon height ~ 1.5 nm, two layers. In (c), the three GNRs are two to three layers thick. In (d), ribbons are one (right image) to three layers. In (e), ribbons are two to three layers. In (f), the heights of the ultranarrow ribbons are ~ 1.5 nm, 1.4 nm, and 1.5 nm, respectively. All scale bars indicate 100 nm. From Li *et al.*, Science **319**, 1229 (2008). Reprinted with permission from AAAS.

5000] for 60 min leads to the formation of a homogeneous suspension. After large pieces of materials were removed using centrifugation, a large amount of graphene sheets were then obtained which are suspended in DMF. AFM measurements suggest that 90% of the sheets are individual chemically modified graphene. In order to prevent agglomeration, the graphene sheets have been successfully transferred from DMF to organic solvent 1,2-dichloroethane.

Fabrication of graphene sheets via chemical routes poses both potential and challenges. Efforts are required for both gaining an understanding of the intercalation, oxidation, exfoliation, reduction, fictionalization, and dispersion processes and developing new starting materials and reaction routes. More details can be found in a recent review.⁴⁰

B. Graphene on metal surface

Due to the low surface energy of the basal plane, SLG or MLG sheets can be readily formed on selected metal surfaces via either surface segregation of carbon atoms or thermal decomposition of carbon-containing molecules.³⁹ In the first method, the source of carbon can either be the small amount of carbon impurities or intentionally introduced carbon through annealing the metal in CO atmosphere or in contact with graphite. Then, annealing of the carbon-containing metals at higher temperature causes the carbon to segregate to the surface. Depending on the annealing temperature, the segregated carbon can be in the form of MLGs or SLGs deposited on the surface, or further desorbed from the surface. The former is formed when the segregated carbon reaches thermal equilibrium with the metal. In the second method, the metal surfaces are first covered by carbon-

containing molecules such as ethylene, propene, methane, acetylene, CO, cyclohexane, *n*-heptane, benzene, and toluene at room temperature.³⁹ The subsequent annealing at elevated temperature causes desorption of hydrogen, leading to the formation of graphene sheets on the metal surface. The annealing can also be performed in the presence of these gaseous molecules. There have already been several comprehensive reviews published on this topic.^{37–39} We will only give an overview by summarizing some of the main characteristics of the films grown on metallic substrates.

The metal substrates that have been investigated include but are not limited to Co(0001),¹⁵⁵ Ru(0001),^{156–166} Ni(111),^{167–176} Ni(100),¹⁷⁷ Ir(111),^{178–184} Rh(111),^{156,185} Rh(100),¹⁸⁵ Pd(111), Pd(100),¹⁵⁵ Pt(111),^{155,186–193} Pt(100),^{188–191,194} Pt(110),^{189,190} and Cu.¹⁹⁵ In many cases, the substrate's role is twofold, i.e., functioning as both a substrate and a catalyst. The latter makes the film growth almost self-limited; therefore, it is relatively easy to obtain thin graphene films on metal surface. The two key factors of the metal surfaces that affect the growth of carbon films are electronic structure (atomic structure) of the surface (atoms) and the lattice constant. The former determines the nature of interactions between the carbon π orbital and the substrate surface atoms, while the latter affects the structure of the graphene layers, in particular, in the single-layer sheet case. The lattice constants of graphene, Ni(111), Rh(111), Ru(0001), Ir(111), and Pt(111) are 2.46 Å, 2.49 Å, 2.69 Å, 2.71 Å, 2.72 Å, and 2.77 Å, respectively, corresponding to a lattice mismatch of 1.2%, 8.5%, 9.2%, 9.6%, and 11.2% between graphene and the substrates.³⁹ Unlike the case of epitaxial growth of a typical semiconductor material on lattice mismatched substrate, in which pseudomorphic growth can be achieved through the introduction of lattice strains under a certain critical thickness, graphene cannot be strained so easily on metal due to the large anisotropy in chemical bonding strength between the basal plane and vertical direction. Therefore, except for graphene on Ni(111) in which (1 \times 1) structure is formed due to the small lattice mismatch, in most other cases, graphene supercells are formed on metallic substrates.

Take Ru(0001) as an example, the typical lattice constant of the supercell obtained from the moiré structure is about 30 Å, approximately corresponding to 12 \times 12 graphene on 11 \times 11 Ru(0001) unit cells.^{157,159–161,166} This has also been confirmed by density functional theory (DFT) calculations.¹⁹⁶ Figures 10(a) and 10(b) shows the STM image of graphene on Ru(0001) and the corresponding lattice model of the (11 \times 11) superstructure, respectively. The STM image shows four bright regions and two darker regions of slightly different brightness. The long-range periodic structure is the moiré structure formed by superposition of 12 graphene unit cells and 11 unit cells of the Ru(0001) surface [Fig. 10(b)]. The hexagonal lattice can be seen in the moiré maxima. Recently, a superstructure consisting of four moiré subcells was also observed and revealed by surface x-ray diffraction to be 25 \times 25 graphene unit cells on 23 \times 23 Ru(0001) unit cells.¹⁶³ The x-ray diffraction results suggest that the supercell is formed as the consequence of strong corrugation of both the graphene and underlying Ru sub-

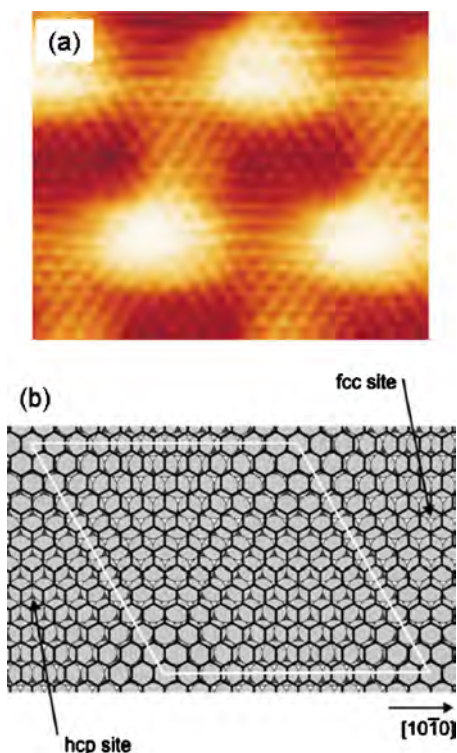


FIG. 10. (Color online) (a) Atomically resolved images of the graphene overlayer on Ru(0001) surface. (b) Model shows a commensurate (11×11) Ru structure with (12×12) graphene unit cells. The first layer Ru atoms are the light gray spheres, the second layer Ru atoms dark gray, and the graphene layer is the honeycomb net. There is no rotation between the graphene and Ru lattices. Reprinted with permission from Marchini *et al.*, Phys. Rev. B 76, 075429 (2007), Copyright 2007 by the American Physical Society.

strate (down to several monolayers). The strong bonding between graphene and Ru weakens the in-plane C–C bonds, which helps accommodate the in-plane tensile stress. Similar moiré structures have also been observed in the graphene/Pt(111) and graphene/Ir(111) systems. The moiré patterns found in graphene/Pt(111) include the coexistence of a non-rotated phase with a periodicity of 22 Å and a 90° rotated phase with a periodicity of 22 Å,¹⁸⁷ or a 4° rotated phase with aperiodicity of 18 Å and a 34° rotated phase without a moiré structure.¹⁹² On the other hand, an incommensurate structure with a periodicity of 9.32 unit cells was observed in graphene formed on Ir(111) surface.^{181,197} Dislocation-free domains with a size of several microns have been obtained by decomposition of ethylene at 1320 K. The film has overgrown the step edges. The edge dislocations accommodate the small-angle misorientations.

As graphene is only one atomic layer thick, naturally the nature of chemical bonding between the carbon and substrate surface atoms is of great concern because it ultimately determines if the carbon film still behaves like a graphene. Although our understanding of graphene/metal interface is still far from complete, one can gauge it approximately through both experimentally observed and calculated vertical spacing between the first carbon layer and the surface layer of the substrate. For Ni(111) surface, it was found that the two carbon sublattices sit on the metal atoms and the fcc hollow sites between these atoms, respectively.¹⁷⁰ The spacing be-

tween the Ni surface and carbon atoms was found to be 2.1 Å and 2.0–2.1 Å, respectively, through ion scattering and low energy electron diffraction (LEED) analyses^{170,198} and first-principles calculations.^{199–201} The small C–Ni distance, as compared to the interlayer spacing of bulk graphite, indicates that graphene is chemically bonded to the Ni substrate. Nevertheless, there are no indications of sp^2 -to- sp^3 rehybridization of the carbon atoms.^{39,200} The graphene structure remains even after the films were detached from Ni and transferred to other substrates.^{202,203} In addition to Ni(111), the calculated distance between graphene sheet and metal surface is also small in graphene/Ru(0001) (2.2 Å) (Ref. 201) and graphene/Pd(111) (2.3 Å) (Ref. 201) systems. On the contrary, the separation of graphene sheet from other (111) metals such as Ir (3.77 Å),¹⁹⁷ Pt (3.3 Å),²⁰¹ Al (3.41 Å),²⁰¹ Ag (3.33 Å),²⁰¹ Cu (3.36 Å),²⁰¹ and Au (3.31 Å) (Ref. 201) are larger than or comparable to that of the interlayer spacing of bulk graphite (3.35 Å).

The interaction with substrate naturally affects the lattice vibration and electronic properties of the graphene. Strong interaction with the substrate results in weaker C–C bonds in the graphene plane and thus softened phonons of the graphene layer, in particular, of the out-of-plane vibration modes. This has been shown experimentally to be the case of graphene on Ni(111) and Ni(001) (Ref. 204) and Ru(0001).¹⁵⁹ On the other hand, the vibration spectrum of graphene on Pt(111) was found to be almost the same as that of bulk graphite.²⁰⁵ Although the origin of the existence of two classes of interfaces, i.e., strong interaction of graphene with Ni, Pd, and Ru and weak interaction with Pt, Ir, Al, Ag, Cu, and Au, are not well understood, it is believed that the interaction strength has something to do with the occupancy and index of d orbitals. There is a trend that the interaction strength increases with decreasing both the index ($5d$ to $3d$) and occupation of the d orbitals.

In addition to the vibration spectrum, significant changes have also been observed in the electronic band structures of graphene sheets on both Ni(111) and Ru(0001) substrates, as revealed by angle-resolved ultraviolet photoemission spectroscopy (ARPES) measurements.^{206,207} Although the energy bands of bulk graphite were clearly observed, the π and σ bands of graphene on Ni(111) are shifted downward by about 2 eV and 1 eV, respectively. This is believed to be caused by the charge transfer from Ni to graphene, which in turn is caused by the hybridization of p_z orbitals of graphene with the $3d$ orbitals of Ni. The charge transfer mainly affects the π band because it is half filled near the K point. The same charge transfer also results in the softening of phonons, as discussed above.²⁰⁴ Similar downshift in π band was also observed in graphene on Ru(0001). Recently, Sutter *et al.*⁴⁹ have shown that the interaction between Ru substrate and graphene is strongly suppressed from the second layer and is almost absent in the third layer.

As somewhat expected, the band shift or distortion was found to be almost absent in graphene on Ir(111).¹⁸⁴ Pletikovic *et al.*¹⁸⁴ investigated the electronic band structure of graphene grown on Ir(111) using ARPES. As shown in Fig. 11, a well-defined Dirac cone was observed which shows no sign of hybridization with the substrate electronic bands,

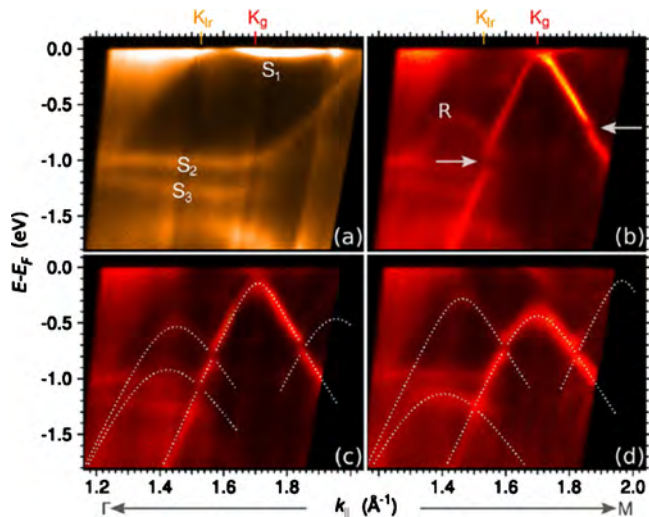


FIG. 11. (Color online) (a) ARPES spectrum of clean Ir(111), $\phi = 0.5^\circ \pm 0.1^\circ$. K_{Ir} and K_g represent the K points of Ir and graphene, respectively. S_1 – S_3 are surface states. (b) ARPES spectrum of Ir(111) covered by graphene along the same azimuth as in (a). Horizontal arrows denote the minigap at the intersection of the primary Dirac cone and BZ boundary. R is a replica band. [(c) and (d)] ARPES spectra for $\phi = 1.4^\circ \pm 0.1^\circ$ and $\phi = 3.0^\circ \pm 0.1^\circ$, respectively. The dashed lines are calculated bands for the Dirac cone replicas due to the superstructure. Reprinted with permission from Pletikosić *et al.*, Phys. Rev. Lett. **102**, 056808 (2009). Copyright 2009 by the American Physical Society.

through the graphene layer is slightly *p*-type doped as evidenced by the upshift in the Dirac cone by about 0.1 eV. The BZ of graphene is aligned with that of the Ir(111) surface lattice. The slight difference between the two reciprocal lattice vectors results in the formation of mini-BZ surrounding the K points of graphene. The superperiodic potential due to lattice mismatch, with the corresponding differential reciprocal lattice vectors, creates replica bands and opens gaps in the Dirac cone along the mini-BZ boundary, which were also observed experimentally [Figs. 11(b)–11(d)]. Due to the inaccessibility of the Dirac point by ARPES, however, it is not possible to confirm if there is a band gap opening at the Dirac point.

Graphene sheets grown on metallic surfaces are generally of higher quality as compared to those obtained by other synthesis techniques; therefore, they are promising candidates for application in electronic devices once large size sheets can be transferred to other insulating substrates. Kim *et al.*²⁰³ have developed a method to transfer graphene sheets grown on Ni foils to SiO_2/Si substrate by using either polydimethylsiloxane (PDMS) stamping or chemical etching (see Fig. 12). In order to reduce the thickness of graphene sheets, instead of using Ni foil, thin layers of nickel of thickness less than 300 nm deposited on SiO_2/Si substrates were used to grow the graphene sheets. The growth was carried out by first heating the substrate to 1000 °C inside a quartz tube under an argon atmosphere, followed by an exposure to a flowing reaction gas mixtures [$\text{CH}_4:\text{H}_2:\text{Ar}=50:65:200$ SCCM (SCCM denotes standard cubic centimeter per minute)] for 30 s to several minutes. It was found that a fast cooling rate ($\sim 10^\circ \text{C s}^{-1}$) is critical in suppressing formation of multiple layers and for separating graphene layers efficiently from the substrate in the later process. The suc-

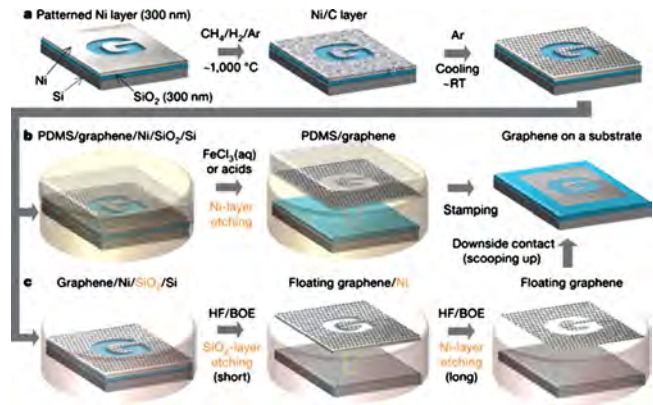


FIG. 12. (Color online) Process flowchart of synthesis and transfer of graphene from Ni to SiO_2/Si substrate. (a) Synthesis of patterned graphene films on thin nickel layers. (b) Etching using FeCl_3 (or acids) and transfer of graphene films using a PDMS stamp. (c) Etching using buffered HF or hydrogen fluoride solution and transfer of graphene films. Reprinted by permission from Macmillan Publishers Ltd: Nature, Kim *et al.*, **457**, 706 (2009), Copyright 2009.

cessful transfer of SLG to SiO_2/Si substrate has been confirmed by the observation half-IQHE. A mobility value greater than $3700 \text{ cm}^2 \text{ V}^{-1} \text{ s}^{-1}$ has been obtained. The authors have also demonstrated the potential application of these graphene films as stretchable transparent electrodes. A similar range of mobility values ($4050 \text{ cm}^2 \text{ V}^{-1} \text{ s}^{-1}$) has also been obtained very recently from graphene sheets transferred from Cu foils.¹⁹⁵

C. Graphene on SiC

As it is discussed above, the key advantage of growing graphene on metallic substrates include the availability of a large number graphene/substrate combinations and relative ease of obtaining large area graphene sheets using simple processes. However, the primary drawback is that it is difficult to fabricate electronic devices using graphene sheets on metallic substrates, unless they are transferred to insulating substrates. This problem can be partially solved by growing graphene directly on insulators or semiconductors. The most successful and representative example is the growth of graphene on SiC substrates. SiC is a wide band gap semiconductor with both cubic and a number of hexagonal crystalline structures. The growth of graphene is mainly performed on hexagonal SiC with *ABCB...* stacking (4H-SiC) and *ABCACB...* stacking (6H-SiC). Both types of SiC polytypes have two polar faces perpendicular to the *c*-axis, i.e., Si-terminated SiC(0001) face and C-terminated SiC(000 $\bar{1}$) face. The polar of SiC surface has determinate effect on both the growth and properties of graphene. For comprehensive reviews on epitaxial growth of graphene on SiC the reader is referred to Refs. 35 and 36. Here, we just provide a brief summary of some of the major findings.

Bommel *et al.*²⁰⁸ have conducted probably the first detailed investigation into thin graphite layer formation upon heating SiC in ultrahigh vacuum ($\sim 10^{-10}$ Torr). Using low-energy electron diffraction and Auger electron spectroscopy analysis, they found that a carbon-rich surface is formed on both the Si-face and C-face of SiC at temperatures between

1000 and 1500 °C. The carbon layer is predominantly graphite after heating at 1500 °C, which has a distinct crystallographic relation to the SiC crystal. It was also found that the graphite layer is monocrystalline on the Si-face and mostly polycrystalline on the C-face. Subsequent works further confirmed the difference in graphitization processes between Si-face and C-face,²⁰⁹ and revealed that the thin graphite layer on Si-face is epitaxial with its lattice rotated 30° with respect to SiC[10 $\bar{1}$ 0] direction²¹⁰ while that on C-face generally exhibits multiple orientational phases.²¹¹

Although significant progresses have been made recently in this field, in particular, the success in growing single and few layer graphene sheets on SiC,^{212,213} understanding of the entire process from surface reconstruction to Si-sublimation and graphitization is still far from complete. A typical graphene growth process on Si-face SiC begins with the preparation of SiC surface. The exact preparation procedure varies, depending on the original surface condition of the substrate that is used. In most cases, a hydrogen etch is employed to remove the scratches and obtain regular atomic stepped surfaces.^{36,214–217} Heating the substrate to about 800–1000 °C in UHV and in the presence of Si flux removes the oxide layer and at the same time leads to the formation of a Si-rich (3×3) phase.^{36,218–220} Starting from this (3×3) phase, a series of intermediate phases would appear before a C-rich (6 $\sqrt{3}$ ×6 $\sqrt{3}$)R30 phase is formed at about 1100 °C.^{36,220–224} There are no unified patterns of appearance of the intermediate phases; in addition to temperature, the appearance of a specific surface reconstruction is also dependent on the quality of the original substrate surface, and heating methods, speed, atmosphere, etc. As the C-rich (6 $\sqrt{3}$ ×6 $\sqrt{3}$)R30 phase serves as the precursor of graphene growth, homogeneity of this phase plays a crucial role in determining the growth and properties of the graphene layers, which is induced by further heating the sample to 1200–1350 °C.^{36,222}

One of the bottlenecks in growing graphene on Si-face SiC is the roughening of the substrate accompanied by graphitization, which significantly limits the domain size of the graphene. Regardless of the initial step size of the substrate, the average step size after graphene formation is mostly in the range of 20–50 nm.^{36,222} The large roughness suggests that the surface is far from equilibrium during the graphitization process, preventing it from achieving a smooth morphology. Using *in situ* low-energy electron microscopy (LEEM), Tromp and Hannon showed that the phase transformation temperatures can be varied over a large temperature range and the transformation time can be reduced by several orders of magnitude, via balancing the rate of Si evaporation and an external flux of Si.²²¹ The ability to achieve quasiequilibrium at higher temperature in the presence of disilane greatly reduce the phase transformation time which in turn makes it possible to obtain homogeneous (6 $\sqrt{3}$ ×6 $\sqrt{3}$)R30 phase with a large domain size. This may eventually lead to the reduction in final surface roughness in graphene grown on the Si-face SiC.

Instead of heating SiC in UHV, Emtsev *et al.*²²⁵ have shown that wafer-size graphene layers can be obtained through *ex situ* graphitization of Si-terminated SiC(0001) in

an argon atmosphere of about 1 bar. They have compared the surface morphologies of graphene obtained from two different routes with that of hydrogen etched substrate. As shown in Fig. 13(a), the hydrogen etched 6H-SiC(0001) surface exhibits a well-defined terrace structure as determined by AFM. For this specific sample, the terrace width is of the order of 300–700 nm, which are determined by the incidental misorientation of the substrate surface with respect to the crystallographic (0001) plane, and the step height is 1.5 nm, which corresponds to the size of one 6H-SiC unit cell in *c* axis. However, after the growth of a monolayer of graphene by vacuum annealing, the original steps are hardly seen in the AFM image, as shown in Fig. 13(b). This agrees with the well-documented facts that the graphene growth is accompanied by substantial roughening of the substrate surface.^{36,222}

The LEEM image [Fig. 13(c)] confirms that the so fabricated graphene has an inhomogeneous thickness distribution, including regions coexisting with graphene bilayer islands and uncovered (6 $\sqrt{3}$ ×6 $\sqrt{3}$) buffer layer. The surface morphology of graphene improves drastically, obtained by heating the SiC under 900 mbar of argon at 1650 °C, as demonstrated by the AFM image in Fig. 13(d). Large continuous terraces are formed through step bunching, leading to macroterraces that are a factor of five to eight times wider than the original terraces, 50 μ m long along the step edges, and have an average height of 8–15 nm. The LEEM images, Figs. 13(e) and 13(f), show that the graphene sheets grown by annealing SiC in the presence of Ar have a remarkable uniform thickness distribution. The spatially resolved LEEM I-V spectra [Figs. 13(g) and 13(h)], taken along a vertical and a horizontal line in Fig. 13(f), allow the authors to conclude that except for narrow stripes at the edges, the large atomically flat macroterraces are homogeneously covered with a graphene monolayer. The narrower and darker regions at the downward edges of the terraces correspond to bilayer and in some cases trilayer graphene. In the AFM images shown in Fig. 13(i), these regions appear as small depressions of around 0.5 and 1 nm amplitude located at the edge of the macrostep, suggesting that the nucleation of new graphene layers starts at step edges of the substrate surface. The authors attribute the improvement of surface morphology to significantly higher annealing temperature of 1650 °C, as compared with 1280 °C in UHV. A higher temperature growth is attainable because the presence of a high pressure of argon leads to a reduced Si evaporation rate. The significantly higher growth temperature in turn results in an enhancement of surface diffusion, which ultimately leads to the markedly improved surface morphology.

Compared to the bulk number of work on Si-face, there are much fewer studies on the growth of graphene on C-face SiC. Unlike Si-face, generally it is more difficult to prepare the surface of C-face SiC in UHV.²²² In this context, Hass *et al.*^{36,226} have developed a method to prepare C-face 4H-SiC samples by heating them in a vacuum rf-induction furnace at a pressure of $P=3\times 10^{-5}$ Torr. The samples were first heated to 1200 °C for about 20 min to outgas the furnace and remove the surface oxide from SiC. After this step the furnace is quickly ramped to ~ 1420 °C, at which 4–13 lay-

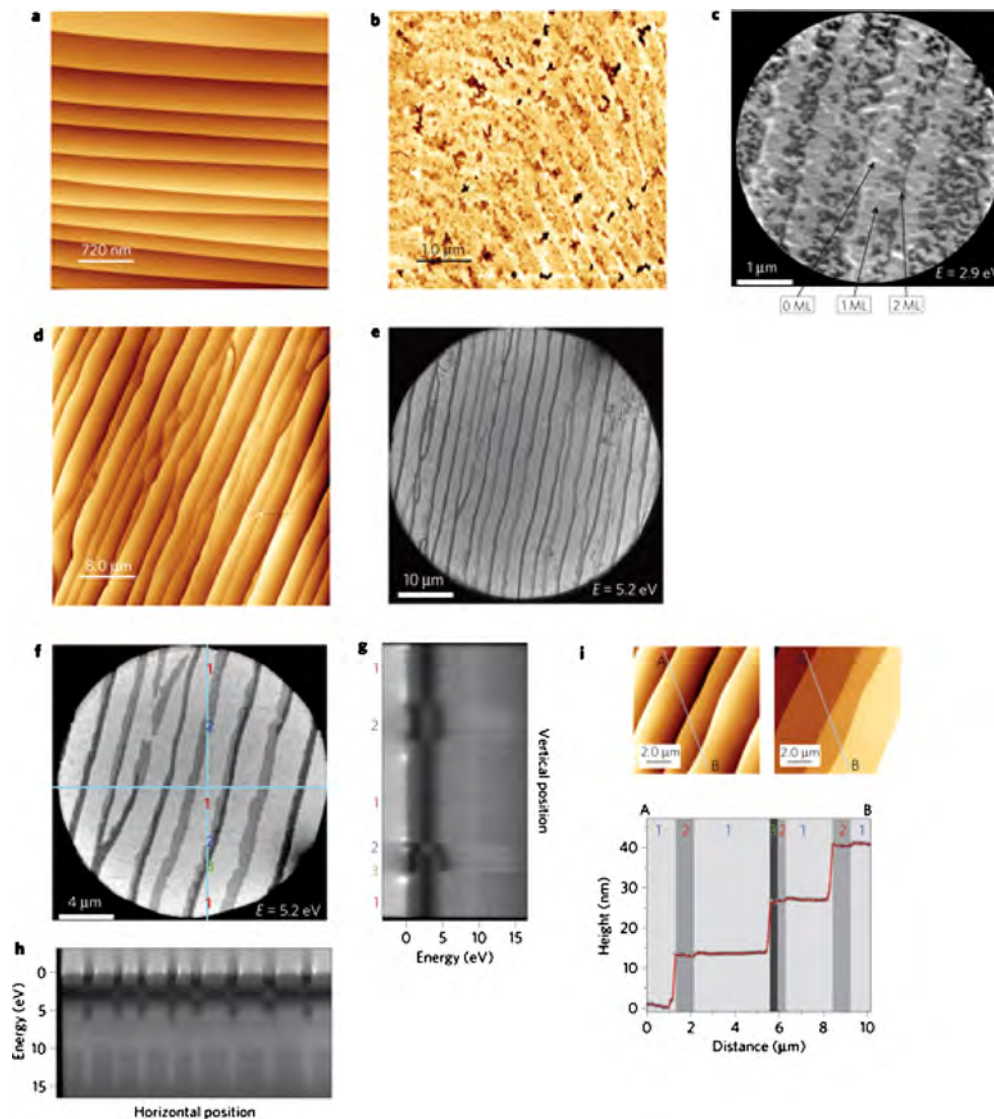


FIG. 13. (Color online) (a) AFM image of H-etched 6H-SiC(0001) surface; (b) AFM image of graphene on 6H-SiC(0001) with a nominal thickness of one monolayer formed by annealing in UHV at a temperature of about 1280 °C; (c) LEEM image of a UHV-grown graphene film with a nominal thickness of 1.2 monolayer; light, medium, and dark gray correspond to a local thickness of zero monolayer, one monolayer, and two monolayer, respectively; (d) AFM image of graphene with a nominal thickness of 1.2 monolayer formed by annealing in Ar ($p=900$ mbar, $T=1650$ °C); (e) LEEM image of a sample equivalent to that of (d); (f) Close-up of the image shown in (e); (g) and (h) electron reflectivity spectra taken at the positions indicated by the lines in (f); (i) close-up AFM images of the film shown in (d). Reprinted by permission from Macmillan Publishers Ltd: Nature, Emtsev *et al.*, **8**, 203 (2009), Copyright 2009.

ers of graphene grow in about 5–8 min.^{36,227} The quality of graphene grown by annealing in rf furnace is exceptionally good.

The separation between the first graphene layer and the SiC surface is found to be only 1.62 Å, implying that there is a very strong interaction between the first graphene layer and the substrate.²²⁷ This strongly bonded layer serves as a buffer to reduce the effect of the substrate exerting on the second layer and above, leading to an rms roughness of <0.05 Å. Hass *et al.*^{48,228} have found that, unlike Si-face films, the C-face epitaxial graphene can grow in following three main rotated phases: layers rotated 30° (R_{30}) or $\pm 2.20^\circ$ (R_{2^\pm}) with respect to the SiC $[10\bar{1}0]$ direction. Surface x-ray diffraction and STM showed that these three rotated phases are interleaved in the film, causing a high density of stacking fault boundaries between the R_{30} and R_{2^\pm} layer. This new stacking sequence preserves the electronic symmetry of an

isolated graphene sheet in C-face grown films,¹⁷¹ as confirmed by the observation of high mobility and other characteristics of SLG in MLG sheets.^{69,227} As one of the example, Fig. 14 shows the recently reported LL spectrum of SLG from MLG sheets grown on the carbon-face of 4H-SiC ($000\bar{1}$) substrate. The unique features of LLs in graphene (see Sec. II A) are clearly demonstrated in Fig. 14. As shown in the inset of Fig. 14(a), the coupling between the topmost layer and the remaining layers is essentially zero. This unique feature makes C-face grown graphene more promising for electronics applications.

D. Synthesis of free-standing 2D carbon

In addition to epitaxial growth, 2D carbon can also be grown in a free-standing form, just like 0D and 1D carbon nanostructures. In fact, 2D carbon often coexists with 0D and

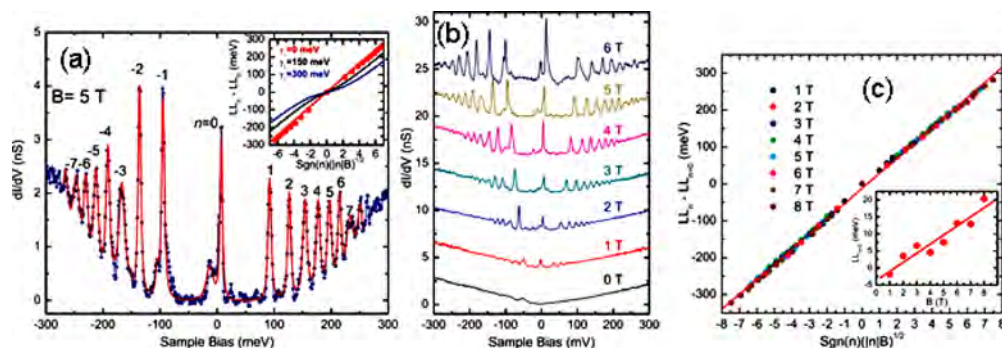


FIG. 14. (Color online) LL spectrum in epitaxial graphene. (a) Tunneling differential conductance spectra vs sample bias of LLs in MLG at $B=5$ T (blue dot: experimental data; red line: fitting in Voigt line shape at LL peak positions). Inset shows the LL peak position vs square root of LL index and applied field from the peak positions in (a). Solid lines are fits to a bilayer model with interlayer coupling of zero (red), 150 meV (black), and 300 meV (blue). (b) LL spectra for various applied magnetic fields from 0 to 6 T. The curves are offset for clarity (tunneling set point, $V_0=350$ mV, $I=400$ pA). (c) LL peak energies for applied fields of 1 to 8 T, showing a collapse of the data when plotted vs square root of LL index and applied field. The solid line shows a linear fit yielding a characteristic velocity of $c^*=(1.128 \pm 0.004) \times 10^6$ ms^{-1} . Inset: the shift in the LL_0 peak position as a function of applied field (symbols). The solid line is a linear fit to the data points. From Miller *et al.*, *Science* **324**, 924 (2009). Reprinted with permission from AAAS.

1D structures during the preparation of the latter using laser ablation and arc discharge.^{45,228} The ratio of 2D carbon over the 0D or 1D structure depends strongly on the experimental condition. A general trend is that the lower the growth temperature the higher the yield of 2D carbon. By optimizing the current and hydrogen pressure in dc arc discharge, Ando *et al.*¹¹² found a large amount of petal-like graphite sheets outside the flame region of arc discharge as well as on the graphite wall surrounding the anode and cathode. These nanosheets are highly curved and interlaced with one another, forming spongelike structures.

Compared to laser ablation and arc discharge, the CVD offers a much larger process window for controlling the shape and dimension of carbon nanostructures. In particular, it allows for the growth of 2D carbon nanostructures on foreign substrates, which are important for many applications. Wu *et al.*^{41,42,229,230} reported on the growth of vertically aligned 2D carbon nanostructures on various types of substrate, dubbed CNWs, using MWPECVD. In addition to MWPECVD,^{46,231–237} similar types of 2D carbon nanostructures have also been successfully grown using other techniques such as rf-PECVD (Refs. 43, 44, and 238–245) and hot filament CVD (HFCVD).^{246–249} In what follows, we give an overview of CNWs grown by MWPECVD.

As shown schematically in Fig. 15, the MWPECVD system used by Wu *et al.*^{41,42,229,230} is equipped with a 500 W microwave source and a traverse rectangular cavity to couple the microwave to a quartz tube for generating the plasma. Inside the quartz tube are two parallel plate electrodes placed 2 cm away from each other in the longitudinal direction of the tube, for applying a dc bias during the growth. The gases used were mixtures of CH_4 and H_2 . In this simple setup, as there is no independent substrate heater, the substrate temperature is in the range of 650–700 °C, determined by the power of the microwave source. Apart from the temperature, other important parameters which affect the growth of carbon nanostructures are H_2/CH_4 flow rate ratio and electrical field. The latter consist of both a global dc field, variable by the applied dc bias, and localized ac field due to the plasma itself.

Wu *et al.*⁴¹ have carried out a series of experiments to grow the CNWs using different H_2/CH_4 flow rate ratios. It was found that there was hardly any growth with a H_2/CH_4 flow rate ratio >50 , for a duration of ~ 5 min. Figure 16 shows the morphology of the carbon nanostructures grown on Au (~ 20 nm) coated Si substrates with a fixed gas pressure of 1 Torr but different H_2/CH_4 flow rate ratios. When the H_2/CH_4 flow rate ratio was reduced to 30, some columnar structure of amorphous carbon formed. Further decrease in the gas flow rate ratio led to the formation of a mixture of carbon fibers/tubes and 2D nanographite sheets. A pure form of CNWs forms when the gas flow rate ratio is in the range of 4–8. Too low a gas flow rate ratio would again lead to the formation of amorphous carbon. An optimum H_2/CH_4 flow rate ratio was found in these studies.

Figure 17(a) shows a typical SEM image of the CNWs grown under optimum conditions.⁴¹ The distribution of the nanowalls was found to be remarkably uniform over the

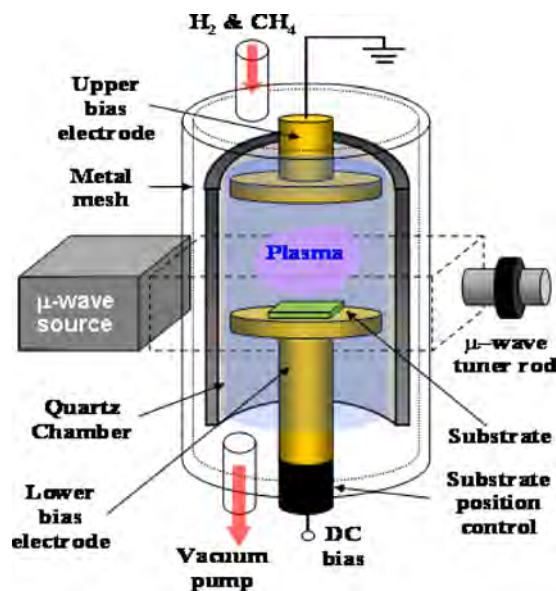


FIG. 15. (Color online) Schematic of MWPECVD used in Refs. 41, 42, 229, and 230.

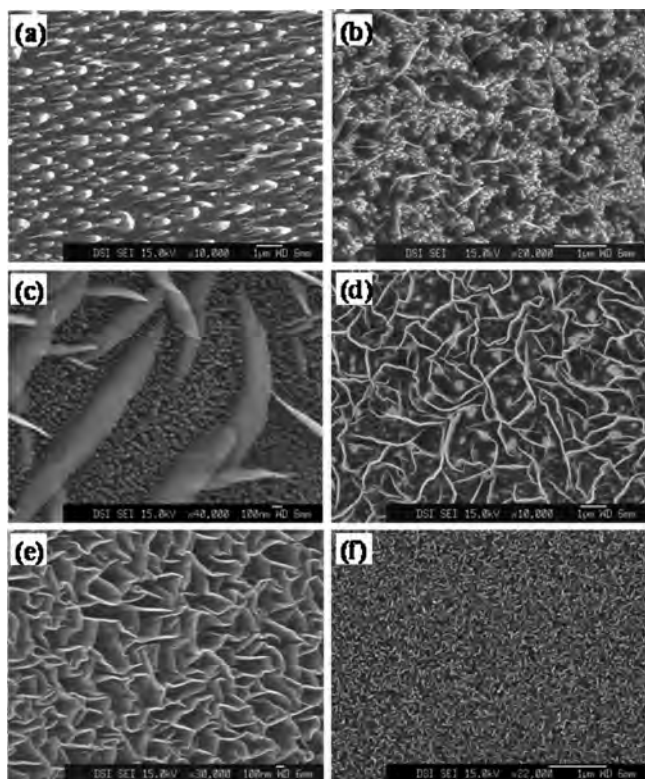


FIG. 16. SEM images of carbon nanostructures grown at different H_2/CH_4 flow rate ratios. (a) 30, (b) 15, (c) 10, (d) 6, (e) 4, (f) 1. Scale bars: (a), (b), (d), and (f) $1\ \mu\text{m}$, (c) and (e) $100\ \text{nm}$. Y. H. Wu *et al.*, *J. Mater. Chem.* **14**, 469 (2004). Reproduced by permission of the Royal Society of Chemistry.

whole substrate surface area that is typically $1 \times 1\ \text{cm}^2$. Figure 17(b) shows some of the nanowalls peeled off from the substrate and lie down on top of the nanowall samples. The nanowalls grow very fast at the first 1–2 min and nearly stop growing after they reach a height of about $2\ \mu\text{m}$. The width is in the range of $0.1\text{--}2\ \mu\text{m}$; it increases with decreasing the nanowall density. The thickness of the nanowalls is typically in the range of one to several nanometers, although sheets as thin as two monolayers were observed by high-resolution transmission electron microscope (HRTEM), as shown in Fig. 18.^{41,250} It is interesting to note that, for some CNWs, the thickness decreases along the growth direction, approaching one monolayer at the top edges. As will be discussed in detail in the later part of this review, Raman spectroscopy revealed that the CNWs contains highly graphitized domains embedded in a disordered 2D carbon host matrix.

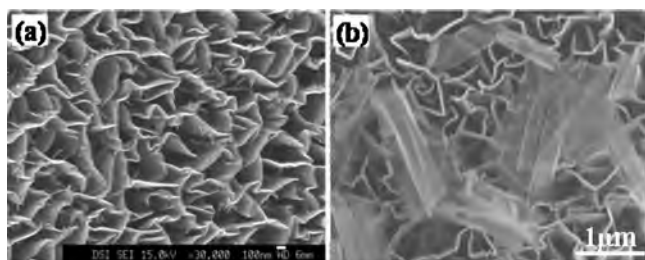


FIG. 17. SEM images of CNWs grown at a H_2/CH_4 flow rate ratio of 4. Scale bars: (a) $100\ \text{nm}$ and (b) $1\ \mu\text{m}$. (a) Was taken at a tilt angle of 25° . Y. H. Wu *et al.*, *J. Mater. Chem.* **14**, 469 (2004). Reproduced by permission of the Royal Society of Chemistry.

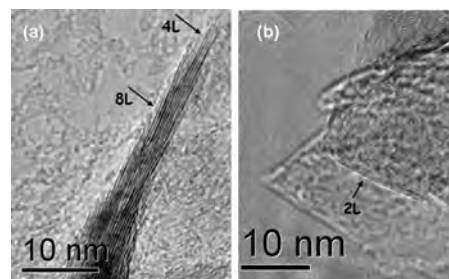


FIG. 18. HRTEM images of CNWs grown at a H_2/CH_4 flow rate ratio of 4. Reprinted with permission from Yang, Ph.D. thesis, National University of Singapore, 2004.

Hiramatsu and co-workers investigated the growth of CNWs using various types of mixtures of fluorocarbon/hydrogen gases, including $\text{C}_2\text{F}_6/\text{H}_2$, CH_4/H_2 , CF_4/H_2 , CHF_3/H_2 , and $\text{C}_4\text{F}_8/\text{H}_2$, in an rf-PECVD system which consists of a parallel-plate rf (13.56 MHz) capacitively coupled plasma chamber and a remote inductively coupled or a surface wave microwave (2.45 GHz) excited H_2 plasma as a radical source.^{44,244,251} The use of a separate H_2 plasma source allowed the authors to study quantitatively the role of hydrogen atom or radicals in the growth of CNWs. The morphologies and growth rate of CNWs were found to be dependent on both the types of carbon sources and rf power of the remote H_2 plasma source.²⁵¹ Among all the gas mixtures investigated, $\text{C}_2\text{F}_6/\text{H}_2$ gave the highest growth rate which is attributed to the effective generation of CF_3 radicals.²⁴⁴ On the other hand, there was no growth of CNWs using either the $\text{C}_4\text{F}_8/\text{H}_2$ mixture or any other carbon source gases without hydrogen. The main role of the H radicals lies in the removal of undesirable amorphous phase during the growth, leading to improved surface morphology and crystalline quality of CNWs. This has been confirmed by measuring the CF_x/H_2 ratio quantitatively and correlating it with the surface morphology of as-grown CNWs.²⁴⁴

Chuang *et al.*²³² reported on the MWPECVD growth of CNWs using a gas mixture of $\text{NH}_3/\text{C}_2\text{H}_2$. It was found that the nanowalls began to grow when the $\text{NH}_3/\text{C}_2\text{H}_2$ flow rate ratio falls below 1 and the growth rate increases with further decreasing the $\text{NH}_3/\text{C}_2\text{H}_2$ flow rate ratio. The CNWs show more well-defined graphitic wall structures with the increasing ammonia ratio, indicating that the ammonia radicals act as an etchant during the growth of nanowalls, a similar role played by hydrogen in the cases where hydrogen is used as the source gas.

Compared to MWPECVD and rf-PECVD, HFCVD reported to be more suitable for smaller and thus denser nanoflakes²⁴⁶ or nanowalls.²⁴⁷ Using C_2H_2 (3%–15%)/ H_2 mixture as the source gases, Shang *et al.*²⁴⁶ demonstrated that the carbon nanoflakes deposited on Si(100) substrate at $400\text{--}600\ ^\circ\text{C}$ have a thickness of less than about $10\text{--}20\ \text{nm}$ and a lateral size of $300\text{--}600\ \text{nm}$. In this temperature range, the size and density of the nanoflakes decreases and increases, respectively, as the temperature increases. When the substrate temperature was increased to $700\ ^\circ\text{C}$, the thickness and lateral size of the carbon flakes decreases to about $5\ \text{nm}$ and $80\ \text{nm}$, respectively, leading to the formation of a very dense film. Dikonimos *et al.*²⁴⁷ investigated the effect of a dc

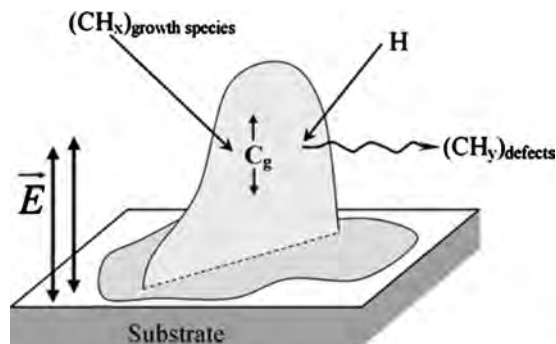


FIG. 19. Schematic of the growth model of carbon nanosheets. \vec{E} : electric field near a substrate surface; CH_x : carbon-bearing growth species impinging from gas phase; C_g : growth species diffuse along carbon nanosheet surface; H : atomic hydrogen impinging from gas phase; CH_y : defects removed from carbon nanosheet by atomic hydrogen etching effects. Reprinted from Zhu *et al.*, Carbon **45**, 2229 (2007), Copyright 2007, with permission from Elsevier.

plasma on the HFCVD growth of nanowalls using CH_4/He as the gas mixture. Both the thickness and lateral size initially increase with increasing the plasma current which subsequently saturate at a total plasma current of 100 mA in that specific setup. CNWs with a maximum lateral size ranging from 10 to 200 nm and thickness lower than 5 nm, have been grown on Si substrates. Both the lateral size and density are much higher than those of nanowalls grown by rf-PECVD or MWPECVD. Well-aligned CNWs were also successfully synthesized by an electron beam excited PECVD using a mixture of CH_4 and H_2 at a total pressure of 2–4 Pa and a temperature of 570 °C.²⁵²

The CNWs or nanosheets can be grown on any type of substrates without catalyst as long as the substrate can sustain the growth temperature which is typically below 800 °C.^{41,43} Unlike the CNT case, the growth mechanism of 2D carbon by CVD is still not well understood. Zhu *et al.*²⁵³ proposed a model for the growth of 2D carbon nanosheets using rf-PECVD. In their experiments, the nanosheets were deposited on a variety of substrates in an inductively coupled plasma from a gas mixture of $\text{CH}_4(5\%–100\%)/\text{H}_2$, at a total gas pressure of 20–400 mTorr, substrate temperature of 600–950 °C, and rf power of 400–1200 W. According to this model, the nanosheet initially grows parallel to the substrate up to a thickness of 1–15 nm before the onset of vertical growth. The formation of parallel layer has been confirmed by surface x-ray scattering measurements.²⁵⁴ The latter is presumably caused by the building up of upward curling force at the grain boundaries of nanographite domains. Once the nanosheet is oriented in the vertical direction, it grows much faster in the direction parallel to the sheet due to the very high surface mobility of incoming C atoms or CH_x radicals and polarization of the graphitic layers induced by the local electric field in the sheath layer (Fig. 19). The fast diffusion of carbon-bearing species and etching by hydrogen radicals strongly suppress the growth in thickness direction. Once they reach the edges, however, the carbon-bearing species will form bonds with edge atoms, leading to the growth in height direction. The free-standing 2D carbon formed by various types of plasma processes contains a high density of defects due to the bombardment by

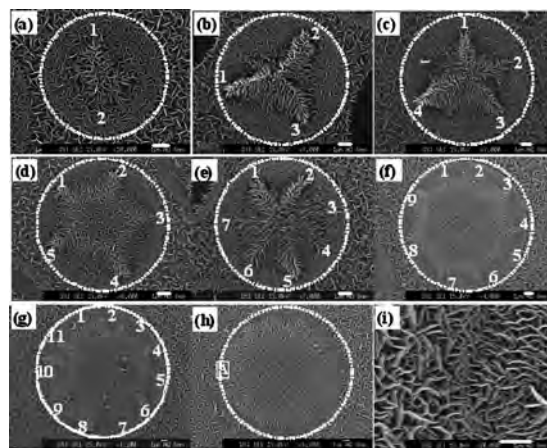


FIG. 20. SEM images of CNW patterns formed by the electrical field of surface plasmons with different number of poles. (i) is the enlarged image of portion (a) in (h). Scale bars: 1 μm . Adapted with permission from Wu *et al.*, Nano. Lett. **2**, 355 (2002). Copyright 2002, American Chemical Society.

high energy electrons, ions and radicals. This has been revealed by Raman spectroscopy^{42,240,255} and TEM.²⁵⁶

Wu *et al.*^{41,230} have conducted a series of experiments to investigate the effect of lateral field on the growth of CNWs by making use of strong electrical field surrounding metallic nanoparticles on an insulating substrate or sharp features created by anisotropic etch of Si. In the former case, the strong electrical field is associated with the excitation of surface plasmon, while the latter is due to the large surface curvature. The surface plasmon was created by exciting the Au nanoparticles on sapphire substrate using the photon emissions from the plasma. The Au particles in turn were obtained through annealing the Au films in a hydrogen plasma environment.²³⁰ It was found that the influence of the surface plasmon to the growth of CNWs was a rather drastic one. Figure 20 summarizes the unique CNW patterns that have been observed due to the presence of surface plasmon. The circular region consists of an outer ring with denser nanowalls and a flower-like nanowall structure at the center. The latter consists of one to several poles and the number of poles increases with the density of the nanowalls surrounding the circular region, so is the size of the entire region [see Figs. 20(a)–20(h)]. However, the occupation ratio of the outer ring in the whole circular region decreases when the number of poles increases. Figure 20(i) shows an enlarged view of the boundary between the circular region and the region surrounding it. It shows clearly that the nanowalls orient randomly outside the circular region, while they align well along the circumference direction in the rim region and change the direction by almost 90° when they move further to the central region. This large change in wall orientation within a very localized region could hardly be possible without the existence of strongly localized electric fields induced by the surface plasmon. The patterns shown in panels (a)–(h) resemble well the electric field distribution of multiple pole surface plasmon (SP) predicted by Mie's theory with the number of poles increasing from (a)–(h).²⁵⁷ The size of the pattern increases with the number of poles. It is about 8 μm for the dipole pattern shown in panel (a) and 20 μm for the multiple pole patterns shown in (g) and (h). Assume that the

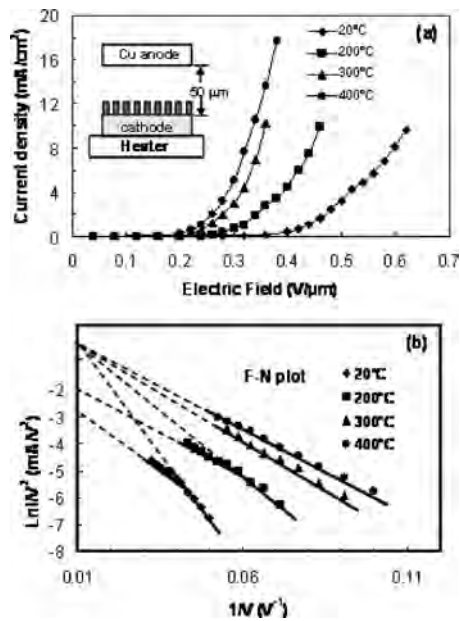


FIG. 21. (a) Emission current density as a function of the electrical field at different temperatures for CNWs and (b) the corresponding FN plots of the curves in (a). The inset of (a) shows the sample configuration for field emission measurement. Y. H. Wu *et al.*, *J. Mater. Chem.* **14**, 469 (2004). Reproduced by permission of the Royal Society of Chemistry.

surface plasmon emission travels at the same speed of light in vacuum, it gives a lifetime of about 25 fs and 70 fs, respectively. These values agree well with the reported lifetime for surface plasmons in literature. In addition to gaining an insight into the growth mechanism of CNWs, this work has also successfully “fingerprint” the electric field of surface plasmon at nanometer scale accuracy. This is a remarkable result because it is the only technique reported so far which can detect the electrical field instead of the intensity of the surface plasmons. Similar type of plasmon-based technique has been employed elsewhere to assist the growth and fabrication of various types of nanostructures.^{258–260}

The free-standing 2D carbon nanostructures are particularly suitable for field emission applications.^{41,43,239,261–265} Wu *et al.*⁴¹ carried out a series of experiments to investigate the field emission characteristics of the CNWs grown on Cu substrates. The turn-on electrical field was found to be in the range of 1–1.5 V/ μm at an emission current density of 10 $\mu\text{A}/\text{cm}^2$ and at room temperature. The small threshold electrical field is attributed to the sharp edges and good alignment of the nanowalls on the substrates grown by MWPECVD. Figure 21(a) shows the emission current densities as a function of the applied electric field for one of such samples obtained at temperatures of 20 °C, 200 °C, 300 °C, and 400 °C, respectively, and at an anode–cathode distance of 50 μm . The experiments were carried out at 20 °C first, and then were repeated at different temperatures after the substrate was heated up using a resistive heater and stabilized at each temperature setting point. The turn-on electric field decreased to 0.26 V/ μm , 0.2 V/ μm , and 0.16 V/ μm with the temperature increasing to 200 °C, 300 °C, and 400 °C, respectively. Figure 21(b) shows the $\ln(I/V^2)$ versus $1/V$, or Fowler–Nordheim (FN) plot, where V is the applied voltage between the cathode and anode. It was observed that

FN plot is linear at 300 and 400 °C but deviates from the linear relationship at low temperature. It was argued that there exist two energy barriers with different height at lower temperatures, which could be caused by the adsorbates on the nanowall surfaces. The adsorbates in this case are most likely hydrogen because the nanowalls were grown using a mixture gas of CH_4 and H_2 . Araidai *et al.*²⁶⁶ investigated field emission from graphitic ribbons by first-principles calculations based on time-dependent DFT. It was found that the field emission current from graphitic ribbons depends strongly on the hydrogen termination and the direction of the applied electric field. Recently, Elias *et al.*²⁶⁷ demonstrated that the electronic properties of SLG can be readily modified through a reversible hydrogenation process. The absorbed hydrogen can be completely removed through thermal annealing at 300 °C. Luo *et al.*²⁶⁸ have conducted a more detailed study about the hydrogen desorption processes through monitoring the D band to G band intensity ratio of the Raman spectrum. The results show that the dehydrogenation occurs in two processes with different activation energies. The dehydrogenation occurs rapidly below 200 °C, beyond which it processes slowly and is completed at 300 °C, agreeing well with the trend observed in field emission.

Compared to 2D carbon grown on different types of substrate, the largest advantage of free-standing carbon is that the effect of substrate on the electrical transport properties is almost negligible. Of course, at the same time, this is also the drawback because it is difficult to form electrodes for electrical transport measurements. Wu and co-workers have studied the electrical transport properties of CNWs using both the top⁴¹ and bottom electrodes.²⁶⁹ The former allows the authors to study the transport properties across self-assembled 2D carbon networks, which exhibits interesting oscillations in MR. The latter makes it possible to study the transport of a single piece of free-standing nanosheets. Takeuchi *et al.*¹⁷³ have attempted to control the conductivity of CNWs through nitrogen doping. If both p and n -type conductivity can be obtained through doping, it is possible to form nanometer scale p - n junctions of 2D carbon on wafer-level. The nanowalls can also be used as templates to form other types of nanostructures or junctions.²⁷⁰

E. Fabrication of GNRs

The exceptionally high mobility makes graphene very appealing for electronics applications.^{32,108} However, the major obstacle to applying graphene in electronics, especially FETs is its lack of band gap. Although a sizable gap can be opened in graphene through making it into narrow ribbons,^{70,74,77} as discussed in Sec. II C, it is quite challenging experimentally to make nanoribbons with sharp edges. Top-down techniques such as the combination of e-beam lithography and etching are certainly the natural choices for fabricating GNRs. However, the ribbons produced by this approach tend to have rough edges and the width attained so far is insufficient to have a sizable gap.^{271,272} The rough edges make it difficult to differentiate real gaps from the transport gap. As it is discussed in Sec. IV A 2, Li *et al.*¹²⁷ have successfully produced GNRs with a width of sub-

10-nm from a chemical sonication route, by using intercalated and exfoliated graphite as the starting material. The nanoribbons exhibit semiconducting properties and have been used to fabricate FETs with high on-off ratios. However, by nature of this method, it is not straightforward to control the width distribution, which ranges from sub-10 nm to 100 nm. The yield was also found to be low.

Recently, two groups have demonstrated that it is possible to obtain GNR with well-controlled width via “unzipping” CNTs. As CNTs with a narrow distribution in diameter are relatively easily to be fabricated, this approach offers the possibility to obtain narrow GNRs with both smooth edges and narrow distribution in width. The approach developed by Jiao *et al.* involves the following major steps: (1) dispersing of pristine multiwalled cCNTs with a diameter of 4–18 nm in 1% surfactant solution by brief sonication and depositing them on a Si substrate, (2) spin-coating a 300-nm-thick film of poly(methyl methacrylate) (PMMA) on the nanotubes/Si substrate, (3) peeling-off and flipping over the PMMA/nanotubes composite after baking, and (4) exposing the composite film to a 10-W Ar plasma for various times so as to selectively etching off the top portion of the nanotubes which are not covered the PMMA. It was demonstrated that it is possible to produce single-layer, bilayer, and multilayer GNRs or GNRs with inner CNT cores, depending on the diameter and number of layers of the starting nanotubes and the plasma etching time. The width of the resulting GNRs ranges from 10 to 20 nm, which is about half of the circumference of nanotubes with a mean diameter of 8 nm. Raman study confirms the existence of single-layer, bilayer, and trilayer GNRs. The intensity ratio between D and G band is lower than that of GNRs obtained from the lithography technique, suggesting a lower density in either defects or edge sites. The GNRs were further processed to fabricate FETs through stamping the GNRs onto SiO₂ (500 nm)/Si substrate using the same PMMA film which was subsequently removed via using acetone vapor. The on-off ratios of devices made from GNRs with a width of 6 nm and 7 nm, with a channel length of 250 nm, were 100 and 10, respectively.

On the other hand, the method developed by Kosynkin *et al.* involves the formation of oxidized nanoribbons by suspending multiwalled CNTs in concentrated sulphuric acid followed by treatment with 500 wt % KMnO₄ for 1 h at room temperature (22 °C) and 1 h at 55–70 °C. The oxidized nanoribbons were reduced to GNRs with aqueous N₂H₄ in the presence of ammonia. To prevent reaggregation during the reduction procedure, the nanoribbons were dispersed in an aqueous surfactant solution, sodium dodecyl sulfate. The yield of this technique is reported to be nearly 100%.

Lemme *et al.*²⁷³ and Bell *et al.*²⁷⁴ have attempted to make graphene NRBs using a helium ion microscope with lithography capability. Structures with a size down to sub-10 nm can be easily obtained through direct writing. Although this method offers the possibility of creating ribbons as well as other types of graphene nanostructures, it is quite challenging to completely remove the redeposition so as to obtain ultraclean structures. The imaging process may also cause deposition on or damage to the graphene lattice.

V. STRUCTURAL PROPERTIES OF GRAPHENE AND 2D CARBON

A. TEM

1. Thickness determination

Although TEM has been employed to probe the crystalline structures of thin graphitic layers grown on copper or nickel about half a century ago,²⁷⁵ investigations of monolayer graphite or graphene by electron diffraction became possible only recently after the success of exfoliating graphene from graphite.^{6,276} In these works, the freely suspended graphene sheets were transferred to a microfabricated scaffold from the standard Si wafer with a 300-nm-thick oxide layer. There are two possible ways to identify the number of graphene layers. One of these is to image the folded part of graphene. For monolayer graphene, folding exhibits only a single dark line, similar to TEM images of one-half of a single-walled CNT, while for a bilayer graphene, a folded edge shows two dark lines, as in the case of double-walled nanotubes. However, this method requires observer’s care because even monolayer graphene may have scrolls or multiple folds at the edge which give rise to any number of dark lines. The other approach is to analyze the nanobeam electron diffraction patterns from monolayer or thicker sheets as a function of incidence angles. As monolayer graphene is a 2D crystal lattice, there is only the zero-order Laue zone in its reciprocal space. Therefore, the intensities of diffraction peaks should not change too much with varying the incidence angles. In contrast, bilayer graphene with the extension in the third dimension exhibits obvious changes of total intensity with different incidence angles. Thus, the weak monotonic variation in diffraction intensities with tilt angle is a reliable way to identify the monolayer graphene.

2. Observation of ripples

About six decades ago, theoreticians predicated that a perfect 2D lattice could not exist at any finite temperature because thermal fluctuations should destroy long-range order.^{1,277} This has been found to be true in suspended graphene, which exhibits microscopic ripples, as reflected by the broadening of the diffraction peaks with increasing tilted incidence angles (Fig. 22).²⁷⁶ Such height fluctuations with the size comparable to the lattice could be suppressed by an anharmonic coupling between bending and stretching modes and are essential for the structural stability of 2D carbon membranes. Moreover, the authors also claimed that the existence of the elastic corrugations is consistent with high mobility of charge carriers in graphene and may explain some of its unusual transport characteristics, such as the suppression of WL.

3. Observation of atomic images

Although SLG has been identified by electron diffraction in 2007,²⁷⁶ the lattice and individual carbon atoms were directly visualized two years later with the help of aberration-corrected TEM.^{278,279} Traditional TEM are usually operated at a relatively high acceleration voltage like 200 or 300 kV, which has the risk of destabilizing thin membranes like graphene. To minimize or totally avoid the damage caused

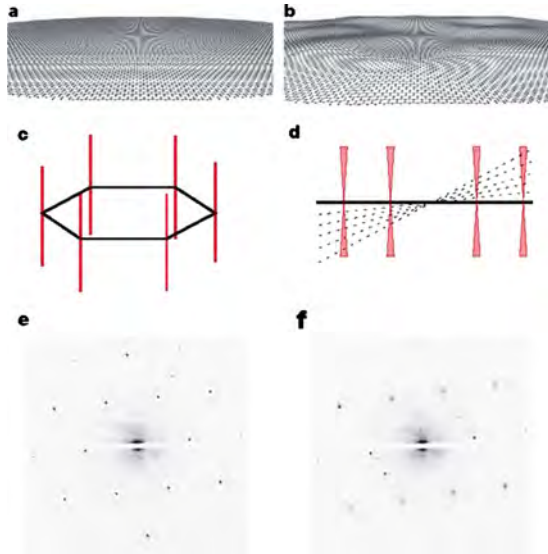


FIG. 22. (Color online) (a) Flat graphene crystal in real space (perspective view). (b) The same for corrugated graphene. (c) The reciprocal space for a flat sheet is a set of rods (red) directed perpendicular to the reciprocal lattice of graphene (black hexagon). (d) For the corrugated sheet, a superposition of the diffracting beams from microscopic flat areas effectively turns the rods into cone-shaped volumes so that diffraction spots become blurred at large angles (indicated by the dotted lines) and the effect is more pronounced further away from the tilt axis. [(e) and (f)] Electron diffraction patterns from a graphene monolayer under incidence angles of 0° and 26° , respectively. The roughness of graphene could be measured from diffraction patterns obtained at different tilt angles. Reprinted by permission from Macmillan Publishers Ltd: Nature, Meyer *et al.*, **446**, 60 (2007), Copyright 2007.

by the electron beam, a low operation voltage is preferred; however, the resolution of traditional TEM operated under such low-voltage is poor. Using a transmission electron aberration-corrected microscope (TEAM), researchers at Lawrence Berkeley National Laboratory successfully achieved 1 Å resolution with the acceleration voltage of only 80 kV. As a result, they directly imaged the individual carbon atoms with few point defects of graphene and further probed the real-time dynamics of defects, e.g., the Stone–Wales (SW) defects.²⁷⁸ Deviating from the highly curved graphene structures such as nanotubes and fullerenes where the formation and transformation of the SW defects involve the dislocation or disclination, the pentagon-heptagon (five to seven) defects relax to the unperturbed graphene lattice. Shape change like shrink has been evidenced in single-walled CNTs after formation of a defect, rearrangement and eventually resulting in the local deformation.²⁸⁰ However, it was not observed in graphene with the planar geometry and fixed boundary, implying the absence of significant strain in graphene.

Instead of bright-field phase contrast, Gass *et al.*²⁷⁹ observed the individual atoms in graphene by high-angle annular dark-field (HAADF) in a STEM in aberration-corrected mode and with an operation voltage of 100 kV. The HAADF images are a direct depiction of the ball-and-stick model of an atomic lattice structure, where bright contrast corresponds to atoms and dark contrast to the gaps between. With the ability of scanning electron beam associated with STEM, the low-loss energy-loss spectroscopy mapping of single-layer, bilayer, and few layered graphene were performed and the

results demonstrated that the single layered graphene exhibits a unique behavior, an obvious redshift in the energy of π and $\pi+\sigma$ plasmons due to the absence of bulk (graphite) component. Carbon vacancies and ring-type defects, resulting from the electron beam damage and the glide movement of reconstructed atom arrangements at each edge of graphene sheets are present in HAADF images. The rolling up of the edges into a nanoscroll was also observed.

4. Edges and their dynamics

The structure of edges of graphene plays an important role in determining the physical and chemical properties of graphene, especially for GNRs, as discussed in Sec. II C. Depending on the atomic structure of their edges, GNRs could behave like either a quasimetal or a semiconductor. Theoreticians suggested that a strong exchange interaction may introduce ferromagnetism to the graphene with the dominant zigzag edge due to the localized spins.²⁸¹ Liu *et al.*²⁸² probed the graphene layers with open and closed edges by TEM. Different from other works, where graphene was prepared by mechanical exfoliation, in this work, the graphene was isolated from graphite by vacuum annealing at an elevated temperature (2000 °C). As no monolayer graphene was found in their experiments, the authors focused on bilayered graphene. Interestingly, rather than the common AB stacking in the Bernal graphite, large number of AA stacking bilayered graphene with the closed edges were found from the high temperature annealed graphite. This might be because the formation of closed edge is favorable for reducing the local strains during the heat treatment. The high-magnification images revealed the existence of the mixture of zigzag and armchair arrangement at the edges. The perfect match between the simulation model and the experimental images confirms that a pentagon-heptagon pair is required for each intersecting point at the closed edges. For the first time, the open edge with the bare carbon atoms also known as Klein edge predicted by theory was observed next to the broken part of a closed edge.²⁸³

The detailed investigations of the stability and dynamics of graphene edges and even artificial manipulation of the edge of graphitic nanoribbons were reported recently.^{284,285} By using a TEAM and recording the images with average 1 s exposure time for each frame, Berkeley's group directly visualized the movement of individual atoms at an isolated edge in real time.²⁸⁴ Comparing to the minimum energy required to remove an in-lattice carbon, a lower knock-on energy threshold for ejection of a carbon at the edge was noticed and attributed to the existence of the vacancies at the edge, which is also responsible for the growth of the hole. The stability of the graphene edges was probed by both time-resolved TEM images and the simulation through a kinetic Monte Carlo method. Both zigzag- and armchair-type arrangement in a long range were observed in the evolution of the graphene hole, implying that they are the stable configurations. Between them, the possibility of observing a longer zigzag edge is higher, indicating that zigzag edge is more stable, which was further supported by the dynamics study. A model was proposed to explain the long term stability of zigzag edges. For an armchair edge, two atoms are involved

to repair the edge. One atom is ejected and its neighboring dangling atom needs to migrate away. However, in a zigzag configuration, only the ejected atom needs replacement. Therefore, the zigzag edge is more stable under electron irradiation. In stead of utilizing the energy of e-beam in a TEAM, MIT's group triggered the reconstruction of the edge of graphitic nanoribbons by resistive Joule heating and simultaneously monitored this process in an integrated TEM-STM system.²⁸⁵ In this work, the efficient shaping of graphitic nanoribbon edges into zigzag or armchair was systematically investigated by both *in situ* high-resolution TEM and theoretical modeling. A local process was employed to explain the formation of zigzag edges based on the following principles. Electronic local states populate along the zigzag edge and the electronic flow in zigzag edged nanoribbons occurs mainly along these edges. At the heterojunction of the zigzag edge and nonzigzag edge, the electronic flow is reduced, equivalent to a large resistance locating at the junction and resulting in the local heat. If the energy dissipating at the junction is large enough, a modification of the shape of edge will happen and the atomic structure will rearrange locally until electronic flow is reestablished. The authors also noticed the transformation of AA stacking to AB stacking during the evolution of the edges. This could be due to the fact that the AB stacking is thermodynamically more stable than AA stacking.

5. Multiple layers

By introducing the rotational stacking faults into AB Bernal stacked graphene bilayers, the incommensurate bilayer graphene exhibits unique physical properties such as changing the parabolic electronic spectrum of an AB bilayer to the linear shape of a single-layer, however with a reduced Fermi velocity comparing to the pure SLG close to the K-point. To understand the structure of such misoriented graphene at the atomic level, Warner *et al.*²⁸⁶ performed a detailed HRTEM study on few layer graphene with rotational stacking faults. After analyzing and filtering the overall HRTEM images of the few layer graphene, an image of each graphene sheet is able to be reconstructed, and this enables to determine the orientations of up to six layers. A typical example is shown in Figs. 23 and 24. The excellent agreement between the experimental TEM images and the simulated Morie pattern demonstrates the promising ability of the low-voltage aberration-corrected HRTEM to resolve the rotational stacking fault in such kind of novel graphene structure.

6. Patterning of graphene

Due to the feasibility of controlling the energy associated with the electron beam and focusing such e-beam into a small dimension, researchers used HRTEM to pattern the graphene. Meyer *et al.*²⁸⁷ successfully demonstrated that the electron beam induced deposition (EBID) could be employed to arbitrarily pattern graphene layers with a nanometer scale resolution. The precursors in the EBID process are hydrocarbons adsorbed on the sample surface. Considering the high sensitivity of graphene's electronic properties to small-scale perturbations, the deposited materials might significantly af-

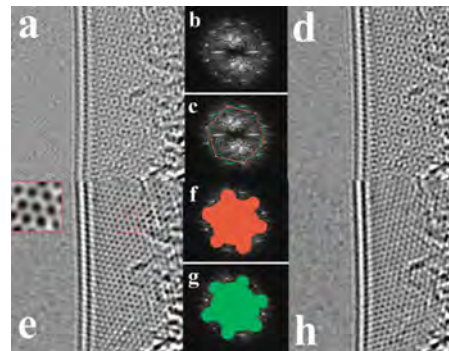


FIG. 23. (Color online) (a) Raw HRTEM image of the edge of a graphene nanosheet showing a bilayer structure with Moire' pattern. (b) Fast Fourier transform of Fig. 1(a) showing two sets of hexagons with 30° rotation between them. (c) Red and green hexagons overlaid on the FFT to indicate the two sets of spots. (d) Reconstructed image after filtering in the frequency domain to include contributions from both sets of hexagons. (e) Reconstructed image showing the back graphene layer with one set of hexagon spots removed by filtering in the frequency domain. Inset shows a magnified section of the graphene indicated with a red box. (f) Mask used to filter in the frequency domain to obtain panel (e), color region is used for the reconstructed image. (g) Mask used for the reconstructed image of the front graphene layer in panel (h). (h) Reconstructed image of the front graphene layer after filtering in the frequency domain. Adapted with permission from Warner *et al.*, Nano Lett. 9, 102 (2009). Copyright 2009 American Chemical Society.

fect the local electronic structure of the graphene membrane. Further efforts on depositing different types of materials with precisely controlled amount, spatial location and dimension may realize the success of engineering the electronic spectrum of graphene. Rather than patterning graphene by introducing foreign materials, Fischbein and Drndic²⁸⁸ created a variety of features like nanometer scale pore, slits and gaps by knocking away the carbon atoms under the irradiation of high energy (200 kV) electron beam in a TEM.

B. STM

STM and STS have been employed to study the topography, crystal structures and electronic properties of carbon

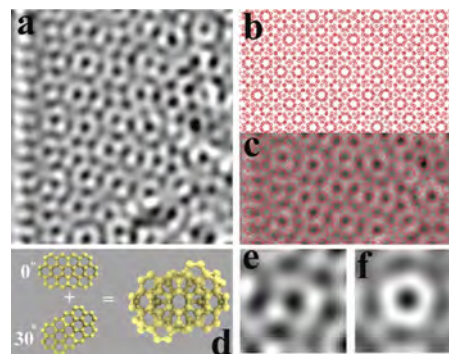


FIG. 24. (Color online) (a) HRTEM image of the Moire' pattern produced in the bilayer structure observed in Fig. 4.2.2. (b) Structural representation of two graphene layers with 30° rotation. (c) Overlay of the structural representation in panel (b) with the HRTEM image in panel (a), showing excellent agreement with the areas of contrast. (d) Schematic diagram illustrating two graphene layers with 30° rotation added together to produce a superstructure. (e) HRTEM image of the superstructure illustrated in panel (d). (f) HRTEM image simulation of the superstructure illustrated in panel (d) and imaged in panel (e) showing excellent agreement. Adapted with permission from Warner *et al.*, Nano Lett. 9, 102 (2009). Copyright 2009 American Chemical Society.

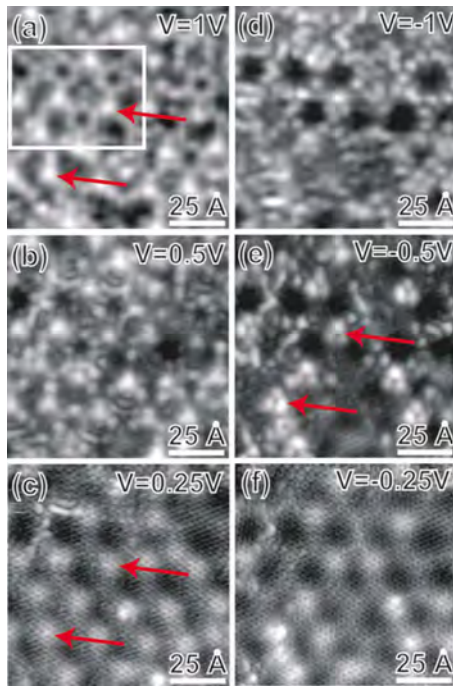


FIG. 25. (Color online) Bias-dependent topographic images show the progression from imaging the SiC interface structure at high bias to imaging the graphene overlayer at low bias. The tunneling current is fixed at 100 pA, and the bias voltages are (a) 1.0 V, (b) 0.5 V, (c) 0.25 V, (d) -1.0 V, (e) -0.5 V, and (f) -0.25 V. Red arrows indicate that different features [tetramers in (a), graphene 6×6 maximum in (c), and trimers in (e)] are imaged at the same surface location, dependent on bias voltage. The white box in (a) designates the area magnified in Fig. 4.3.2(b). Reprinted with permission from Rutter *et al.*, Phys. Rev. B **76**, 235416 (2007). Copyright 2007 by the American Chemical Society.

materials for several decades.^{38,289} After the success of discovering graphene on SiO₂/Si wafer, probing graphene by STM and STS attracts a great deal of attention. In what follows we review briefly characterization of graphene by STM and STS.

1. Superstructures of epitaxial graphene

Berger *et al.*²¹² produced ultrathin epitaxial graphite films (three-layer graphene) and studied the topography and electronic spectrum of epitaxial graphene by STM and STS. As the epitaxial graphene is prepared by graphitizing the polar surface of the hexagonal SiC crystals, the substrates that support graphene play an important role in determining the electrical transport of graphene by, for example, breaking the ideal symmetries or doping the graphene with extrinsic charge. Although the interface electronic states do not contribute to transport directly, the graphene device operation could be readily influenced by these interface electronic states through electrostatic screening of the external potential used to modulate the graphene carrier density. Taking the advantage that graphene appears transparent at energies of ± 1 eV above or below the Fermi energy (E_F), Rutter *et al.*²⁹⁰ visualized the interface structure beneath SLG using STM. As shown in Fig. 25, the authors imaged the same surface location under varying bias voltages (-1 eV \sim $+1$ eV) and clearly demonstrated a direct correspondence between the Si tetramer features and “ 6×6 ” maxima in the graphene domi-

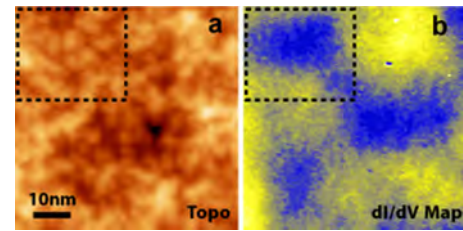


FIG. 26. (Color online) Large area image of graphene topography and charge puddles. (a) 60×60 nm² constant current STM topography of graphene ($V_b = -0.225$ V, $I = 20$ pA). (b) dI/dV map ($V_b = -0.225$ V, $I = 20$ pA, $V_g = 15$ V) taken simultaneously with (a) reveals electron puddles with a characteristic length of ~ 20 nm. Reprinted with permission from Macmillan Publishers Ltd: Nature, Zhang *et al.*, **5**, 722 (2009), Copyright 2009.

nated images, indicating that the 6×6 periodicity observed in graphene layers grown on SiC is due to a SiC interfacial reconstruction, and not a moiré effect. Further detailed analysis (see Fig. 26) revealed that the interface structure, comprised of equivalent structures on each of the three SiC $\sqrt{3} \times \sqrt{3} R30^\circ$ sublattices, which explains many features of the SiC $6\sqrt{3} \times 6\sqrt{3} R30^\circ$ pattern observed in LEED measurement.²¹³ Using the low bias STM images, Hiebel *et al.*²⁹¹ investigated the interface of the epitaxial graphene grown on C face SiC. Their STM analysis showed that the interaction between the first graphitic plane and the substrate is rather weak, especially for the 3×3 surface reconstruction where the characteristic features of graphene appear almost unperturbed at low energy. Brar *et al.*²⁹² measured the local electronic structure of monolayer and bilayer graphene grown on SiC(0001) by STM and STS under both low and high voltage. Spatial inhomogeneity in electronic structure was found and attributed to the nanoscale structure at the SiC/graphene interface. More interestingly and importantly, a gaplike feature around zero bias for both monolayer and bilayer graphene on SiC was noticed in the STS.

Besides studying graphene grown on SiC and exfoliated on SiO₂, STM, and STS have also been widely used to probe the structural and electronic properties of graphene on metals. de Parga *et al.*¹⁶¹ epitaxially grew monolayer graphene on Ru(0001) and examined by STM and STS. The periodical ripples and charge inhomogeneities were observed. Real space STS measurements revealed the existence of electron pockets at the higher parts of the ripples. Pan *et al.*¹⁶⁶ successfully fabricated large dimensional (millimeter-scale) and continuous monolayer graphene on Ru(0001), Ni(111), and Pt(111) crystals. The Moiré pattern resulted from the interference between the lattices of graphene and the Ru crystals was clearly demonstrated. The continuity over the substrate steps was indicated by the absence of bond breakage. Klusek *et al.*²⁹³ deposited monolayer, bilayer, and trilayer graphene sheets on conductive Au/Cr/SiO₂/Si substrate and probed their properties by STM and STS. Dirac points imply the p -type behaviors of graphene due to the donation of holes by the Au substrate. The position of Dirac point show that the larger number of graphene layers the lower Fermi level shift is observed.

2. Scattered electron waves

The quantum state symmetries, which restrict the scattering of the charge carriers in graphene lead to many exceptional electronic properties of graphene. Understanding the effects of defects on the transport properties of graphene is critical to realizing future electronics based on carbon. Rutter *et al.*²⁹⁴ used STM and STS to measure quasiparticle interference patterns in epitaxial graphene grown on SiC(0001). Through differential conductance mapping, the authors imaged the 2D local density of states and revealed modulations on two different length scales, which reflects both intravalley (pseudospin-flip) and intervalley (chirality-reversal) backscattering with the presence of in-plane atomic defects. This result might be helpful on explaining the WL in a similar sample considering the fact that, for perfect monolayer graphene, the near conservation of pseudospin and chirality in the presence of weak potentials is equivalent to a suppression of backscattering.²¹² Meanwhile, WAL was reported in epitaxial graphene grown on C-terminated SiC, indicating a very low density of in-plane atomic scattering centers in those samples.²⁹

Mallet *et al.*²⁹⁵ reported the STM investigation of monolayer and bilayer graphene on 6H-SiC(0001). At low temperature (45 K), both monolayer and bilayer graphene exhibits $\sqrt{3} \times \sqrt{3} R30^\circ$ ($R3$) quantum interferences in the vicinity of static defects on top of the surface. Such $R3$ superstructure around impurities has also been observed in monolayer graphene grown on Ir(111).²⁹⁶ The $R3$ pattern proves the intervalley scattering, which is a key issue for transport properties of graphene. Most recently, Simon *et al.*²⁹⁷ studied the epitaxial graphene grown on *n*-doped SiC(0001) by STM and Fourier transform STM (FT-STM). A strong threefold anisotropy in the standing waves generated by the defect was found and attributed to the chirality of the electrons. The chiral form of the tight-binding Hamiltonian introduces an extra dependence of the scattering amplitude on the angle between the incident and the scattered quasiparticles, which translates an anisotropic intensity along the high-intensity circles at the corners of the BZs in the FT of the local DOS (LDOS) into threefold anisotropic real-space features. Moreover, with the advantage of FT-STs such as the ability of obtaining the quasiparticle dispersion for a wide range of energies, the authors also found that the quasiparticle dispersion remains linear, suggesting that the quasiparticle approximation and the Fermi liquid theory are robust over a large range of energies (-800 to $+800$ meV) in this work.

3. STS measurement of band gaps

Although graphene exhibits great potentials in future nanoelectronics, the fact that there is no gap in the electronic spectrum of graphene does hinder the development of graphene-based FETs. To address this issue, a straightforward way is to introduce quantum confinement, for example, by patterning graphene sheet into narrow ribbons where the electronic wave functions could be quantum mechanically confined and lead to a confinement-induced gap opening. STM and STS have proved their unique advantages in studying the nanographenes like GNRs and graphene quantum

dots (GQDs). Berger *et al.*²¹³ used STM and STS studied the GNRs fabricated by patterning epitaxial graphene through standard lithography techniques. The typical $6\sqrt{3} \times 6\sqrt{3}$ pattern and the continuity of the graphene layer over the step of SiC were clearly revealed by STM and STS.²⁹⁸ Enoki *et al.*²⁹⁹ performed systematic investigation of nanographene with special focus on the edge of graphene.

Tapasztó *et al.*³⁰⁰ demonstrated the new function of STM by successfully patterning graphene on HOPG into nanoribbons of several nanometers in width by STM lithography. They also probed the atomic structure and electronic properties of GNRs by STM and STS. Oscillations in the electron density distribution parallel to the axis of the ribbon, reminiscent to a Fabry–Perot electron resonator was noticed during imaging a 10-nm-wide armchair GNR at low bias voltage (100 mV). Noticing the obvious mismatch between the period of the atomic structure underneath (~ 0.246 nm) and the periodicity of the observed oscillations (~ 0.4 nm), which corresponds to the Fermi wavelength of electron in graphene, and considering that the STM measurements map the electronic wave function near the Fermi level, the authors attributed these oscillations to the quantum mechanical confinement of electrons across the ribbon. It was noticed that the interference patterns are continuous along the entire ribbon, which is a proof of phase-coherent quantum billiard in GNRs at room temperature and further demonstrates electronic waveguides behavior, the 1D nature of the electronic structures of the GNRs. By measuring the first pair of van Hove singularities, STS reveals 0.18 eV and 0.5 eV gaps in the 10 nm and 2.5-nm-wide armchair GNRs, respectively. These values show good agreement with theoretical prediction for separation of the energy levels due to the geometrical restriction of wave functions $E_g(W) = \pi\hbar v_0/W$.²¹³

The electronic structure of GNRs and GQDs has been predicted to depend sensitively on the crystallographic orientation of their edges. Experimentally, Ritter and Lyding³⁰¹ manifested the influence of edge structure by STM and STS. In this work, the GQDs with 2–20 nm lateral dimensions and GNRs with 2–3 nm widths and 20–30 nm lengths were *in situ* exfoliated from HOPG in a UHV chamber and subsequently passivated by hydrogen. STM visualized the edge of the each GQD consists of both armchair and zigzag configurations with some unassigned structure. The fraction of zigzag or armchair could be directly determined through STM images. Combining the STM and STS, the results clearly show that predominantly zigzag edge GQDs with 7–8 nm average dimensions are metallic and GNRs with a higher fraction of zigzag edges display a smaller energy gap than a predominantly armchair-edge ribbon of similar width. This phenomenon was explained by the presence of the localized zigzag edge state. Moreover, a triangular pattern was observed in the STM images of GQDs and attributed to the interference effects induced by the edges.

4. Topographic corrugations and charge puddles

In an ideal graphene sheet charge carriers behave like 2D Dirac fermions. However, usually in the real graphene, especially nonsuspended graphene the existence of perturbations such as topographic corrugations and charge puddles could

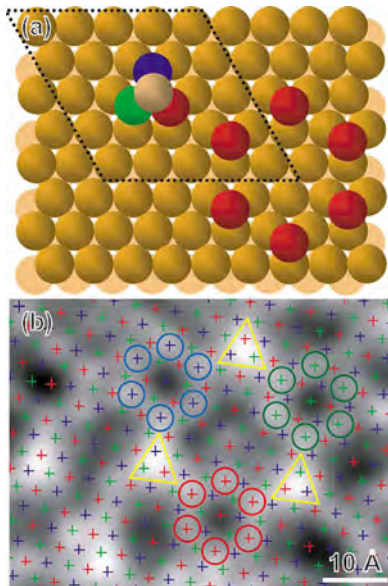


FIG. 27. (Color online) (a) Schematic geometry of possible Si adatom features consisting of one tetramer and hexagon. The three different colors (red, blue, and green) correspond to Si adatoms on three different sublattices as in (b). The gold atoms represent the Si atoms in the SiC substrate. (b) Magnified view of the first layer of graphene from Fig. 4.3.1(a). Three hexagons are observed to lie on the three different SiC $\sqrt{3} \times \sqrt{3}$ sublattices, denoted by the three different colors. Tetramer features (yellow triangles) are what allow hexagons to switch to different $\sqrt{3} \times \sqrt{3}$ sublattices. Reprinted with permission from Rutter *et al.*, Phys. Rev. B **76**, 235416 (2007). Copyright 2007 by the American Chemical Society.

influence Dirac Fermion behavior, with implications for the fundamental physics and future practical applications. Stolyarova *et al.*³⁰² imaged the topography of exfoliated graphene on an insulating surface by STM. A height fluctuation of ~ 0.5 nm on a lateral scale of ~ 10 nm, which is comparable the topographic features of the substrate (SiO₂) determined by AFM was observed. Thus, the reason that causes the nonperiodic roughness of graphene was explained as the graphene sheet follows the features of the underlying SiO₂ surface. Utilizing a combined SEM-AFM-STM technique, Ishigami *et al.*³⁰³ obtained the real-space images of the cleaned monolayer graphene atomic lattice and nanoscale corrugation. The results show that the graphene primarily follows the underlying morphology of SiO₂.

The systematical investigation of the origin of spatial charge inhomogeneities in graphene was conducted by Zhang *et al.*¹⁰⁵ In this work, an electron density spatial resolution which is two orders of magnitude higher than previous measurements was achieved during simultaneously probing the topographic and electronic disorder in graphene by STM and STS. As shown in Fig. 27, the poor correlation of the geometry like lateral dimensions and spatial locations between the topographic corrugation and charge puddles rules out the hypothesis that topographic disorder is the main cause of the charge inhomogeneity. Moreover, the authors claimed that the same perturbations that create graphene charge puddles also act as scattering sites for the Dirac fermions in graphene and lead to quasiparticle interference patterns. The observed quasiparticle interference patterns are raised from quasiparticle scattering from a disordered potential. Considering the samples were prepared in ambient, the

origin of the charge puddles observed in this work was attributed to the molecules from air trapped between graphene and the SiO₂ substrate.

Deshpande *et al.*³⁰⁴ performed low temperature (4.5 K) STM and STS study on morphology, local electronic properties, and scattering phenomena in exfoliated monolayer graphene on SiO₂. The comparison analysis among the topography, local electrochemical potential and LDOS map revealed that the curvature in the graphene flake contributes to a variation in the electrochemical potential but it is not the main factor responsible for the charge puddles in the dI/dV map. In fact, the combination of the ripples and long-range scatters could be responsible for the potential variation. Long-range scatters lead to intravalley scattering within one sublattice creating the electron and hole puddles and short-range scatters such as lattice defects can induce intervalley scattering from one Dirac cone to the other. The authors also probed the intervalley scattering in graphene by visualizing the lattice defects and analyzing the resulting Fourier transforms of the LDOS maps and topography. An enhanced intervalley scattering at low energy was noticed, which proves the presence of WL of carriers.²⁹⁴

5. Landau energy levels

As discussed in Sec. II, in graphene, the LL energies are not equally spaced and include a characteristic zero-energy state. Miller *et al.*⁶⁹ directly observed the discrete, nonequally-spaced energy-level spectrum of LLs, including the emblematic zero-energy state of epitaxial graphene grown on C-face 4H-SiC. A unique STS system with tunneling magnetoconductance oscillations was employed to measure the band structure properties at a variable tunneling energy rather than a single energy at the Fermi surface, which the traditional SdHOs in transport measurement probes. With the help of the TMCOs, the local electrostatic potential of graphene on SiC with atomic scale resolution was determined by spatially mapping the variation in LL_0 . It was noticed that the spatial variation in the local potential of the epitaxial graphene in this work is smoother than previously reported in exfoliated graphene on SiO₂.¹⁰⁴

6. Electron-phonon interaction

Most recently, electron-phonon interaction or inelastic scattering in the graphene attracted attentions when researchers studied the local carrier density-dependent properties of graphene by STM and observed intriguing phenomena. Zhang *et al.*³⁰⁵ noticed a robust unexpected gap-like feature in the graphene tunneling spectrum. STS taken at the same location with varying gate voltages shows the independence of the width and energy position of this gap to the gate voltages. Meanwhile, the conductance minimum shifts monotonically with gate voltage and even switches polarity. Such anomalous graphene energy gap behavior and gate voltage-dependent conductance minima were addressed by a new tunneling process: phonon-mediated inelastic tunneling of electrons into the graphene flake accompanied by a strong suppression of elastic tunneling at E_F . Based on this hypothesis, the conductance minima should arise from inelastic tun-

neling to the graphene Dirac point and the energy location (eV_D) should be offset by $\hbar\omega_o$ from its true energy location, E_D because each inelastically tunneling electron loses energy $\hbar\omega_o$ as described by $E_D = e|V_D| - \hbar\omega_o$. The excellent fit strongly supports the proposed process. Comparing the inelastic excitation energy ($\hbar\omega_o \approx 63$ meV) derived from the experimental data to the energies of phonon modes of graphene, an out-of-plane acoustic phonon mode located near the K/K' points in reciprocal space could be a possible attribution. A DFT calculation further confirms this general interpretation.³⁰⁶

Li *et al.*⁶⁸ reported electron–phonon coupling induced reduction in Fermi velocity v_F in their STM study of graphene on graphite. In this work, the decoupled graphene layers were identified by checking their LL energy present clear dependence on both magnetic field and Landau index. A V-shaped DOS was observed in the STS of monolayer graphene. Interestingly, for the monolayer graphene, a strong shoulder-like feature and a relatively small Fermi velocity, comparing to the tight-binding value¹⁴ were noticed when examining the zero-field and the field-dependent tunneling spectra, respectively. As also evidenced by the DFT calculations,³⁰⁷ electron–phonon coupling could be responsible for the above phenomena. The electron–phonon coupling was also investigated in the STM study on strained graphene on SiO₂ by Teague *et al.*³⁰⁸ Instead of V-shaped spectra expected for Dirac fermions, U-shaped conductance spectra was observed in the STS of strained graphene, though V-shaped spectra could be recovered in the regions of relaxed graphene. An apparent correlation between the strain distributions with the local tunneling conductance was also noticed. These behaviors were attributed to a strain-induced frequency increase in the out-of-plane phonon mode that mediates the low-energy inelastic charge tunneling into graphene.

VI. RAMAN SPECTROSCOPY/IMAGING STUDY ON GRAPHENE

Raman spectroscopy has been used extensively to probe structural and electronic characteristics of carbon materials, especially that of CNTs and graphene-related materials. In general, Raman spectroscopy is a characterization tool that provides information on the vibrational states of a bulk sample and it is normally neither sensitive to the surface nor to the electronic energy levels. However, in the study of carbon materials, due to strong resonance behavior for a large range of laser excitation wavelengths, Raman provides an extremely useful tool to study the electronic structure as well. The resonance effect also makes the Raman signal extremely strong, making study of single-walled carbon nanotubes (SWNT) and SLG possible. An excellent review on fundamental aspects of Raman study of graphene is recently reported by Malard *et al.*⁵⁴

The aim of this section is to provide a useful practical guide on the use of Raman spectroscopy and imaging in the characterization of graphene, particularly in the following aspects: (i) as an unambiguous and easy method to identify the number of layers of graphene sheet; (ii) strain effect that

can modify the electronic band structure; (iii), doping which can be either intentional or unintentional; (iv) graphene sheets with misorientation between the layers; and (v) Raman imaging as a way of determining the crystallographic orientation of graphene.

A. Thickness determination of graphene layers using Raman spectroscopy

As the properties of graphene depend critically on the number of layers, finding a reliable and easy-to-use method to determine the graphene thickness is crucial in graphene study. In the early stage of graphene study, AFM and TEM were employed to measure the thickness of the graphene samples. The AFM method suffers from the fact that there is always an offset in the measurement³⁰⁹ while TEM measurements are time consuming and require a complicated sample preparation procedure.³¹⁰ After Ferrari *et al.*³¹⁰ demonstrated the capability of using 2D band in Raman spectra to study the number of layers of AB stacking graphene, Raman spectroscopy/imaging has become a general method in graphene thickness determination, especially for identification of SLG due to its fast testing speed, large detection area and minimum sample preparation.

Figure 28(a) shows the typical spectra of one, two, three, and four layered graphene made by micromechanical cleavage method, placed on SiO₂ (300 nm)/Si substrate.³¹¹ The number of layers has been verified by AFM. The Raman spectra are obtained with an excitation source of 532 nm. As can be seen from the figure, there are three major Raman features of graphene: The G band (~ 1580 cm⁻¹) that rises from the in-plane vibrations of the sp^2 carbon atoms,³¹² and the 2D band (~ 2700 cm⁻¹) which is a second-order process induced Raman feature.^{313–315} In the presence of disordered carbon atoms or the edge of graphene, another band located around 1300 cm⁻¹ can be observed, which is called the defect-induced band or D band. The appearance of the D band and 2D band is related to the double resonance Raman scattering process, which consists of several steps: (i) an electron–hole pair is excited whose energy is close to that of the excitation photon, (ii) the electron (or hole) is inelastically scattered by a phonon, (iii) the electron (or hole) is scattered by a defect (D band) or another phonon with opposite wavevector (2D band), and (iv) the excited electron and phonon recombine.³¹⁶ Figure 28(b) is an enlarged view of the 2D band. It can be seen that with increasing the number of layers of graphene the 2D band becomes broadened and blueshifted. Such a phenomenon corresponds closely with the band structure of graphene, as the 2D band originates from the two phonon double resonance process, where a sharp and symmetric 2D band is typically observed in SLG.^{310,317,318} Besides the difference in 2D band for graphene of different thickness, the G band intensity increases almost linearly with the graphene thickness, as shown in Fig. 28(a).³¹⁹ This can be understood as more carbon atoms are detected for MLG. Therefore, the intensity of G band can be used to determine the number of layers of graphene. In practice, the Raman

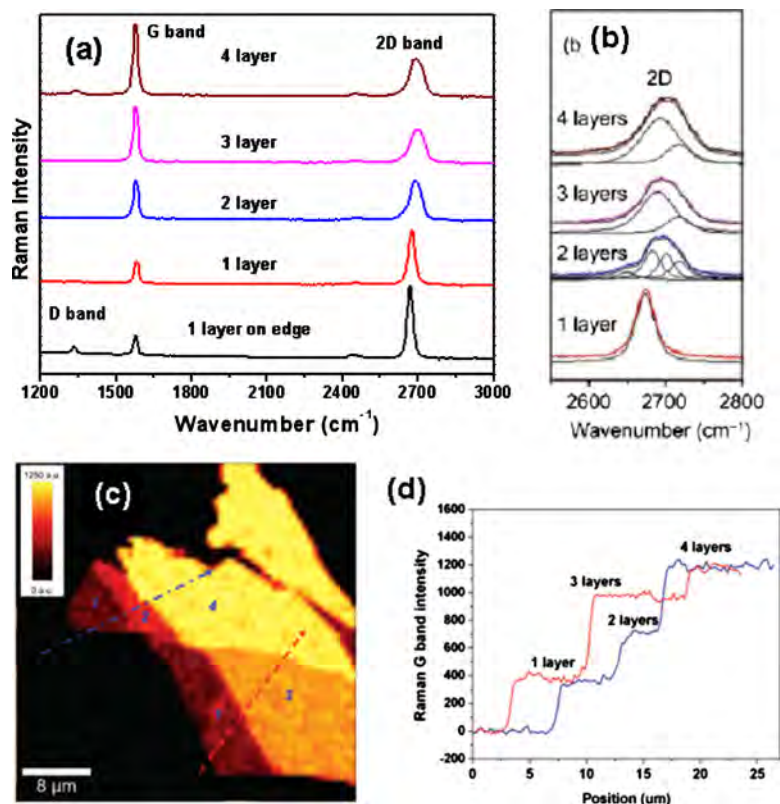


FIG. 28. (Color online) (a) Raman spectra as a function of number of layers. (b) Zoom-in view of the Raman 2D band. (c) Raman image plotted by the intensity of G band. (d) The cross section of Raman image, which corresponds to the dash lines. Reprinted with permission from Ni *et al.*, *Nano Lett.* 7, 2758 (2007). Copyright 2007 by the American Chemical Society.

band intensity ratio between the G band and 2D band is used because the intensity of 2D band is roughly constant. The latter is still not well understood.

In addition to the spectral approaches,^{309,310} Raman imaging is also widely used in graphene study.^{311,320} For example, a Raman image constructed by the intensity of the G band is shown in Fig. 28(c). The sample contains graphene sheet with one, two, and three layers prepared by the mechanical cleavage method. The contrast in this image directly shows the G intensity difference for graphene sheet with different number of layers. The intensity profile of the G band along the dashed line is shown in Fig. 28(d). The linear increase in the G band intensity with the number of layers can be obviously seen. Therefore, the SLG can be distinguished by the width of the 2D band [full width at half maximum (FWHM) ~ 27 cm^{-1}], and the other thickness by its G band intensity or intensity ratio of G band and 2D band. The advantages of Raman spectroscopy and imaging in determining the thickness of graphene are their insensitivity to the substrate, no sample preparation required, ease of use and high accuracy.

B. Raman study on strain effect

Strain in graphene is of great importance for both application and fundamental study. Unexpected strain can affect the performance of the device and even cause an electric breakdown. On the other hand, intentional induced strain may improve the carrier's mobility.⁴⁹ Raman spectroscopy has played a very important role in measuring the strain of carbon nanostructures like CNTs.^{321–325} In a similar manner, Raman spectroscopy/imaging technique can be used to study the strain in graphene. Here, we focus on the effects of

uniaxial and biaxial strain on graphene. The most common way to apply an uniaxial strain is to stabilize the graphene sheet on a flexible substrate,^{326–330} the strain is then applied by curving or stretching/compressing the substrate.

Figure 29 shows the Raman spectra of graphene under uniaxial tensile strain.³²⁹ An obvious redshift in G band and 2D band is observed on tensile strained graphene due to the

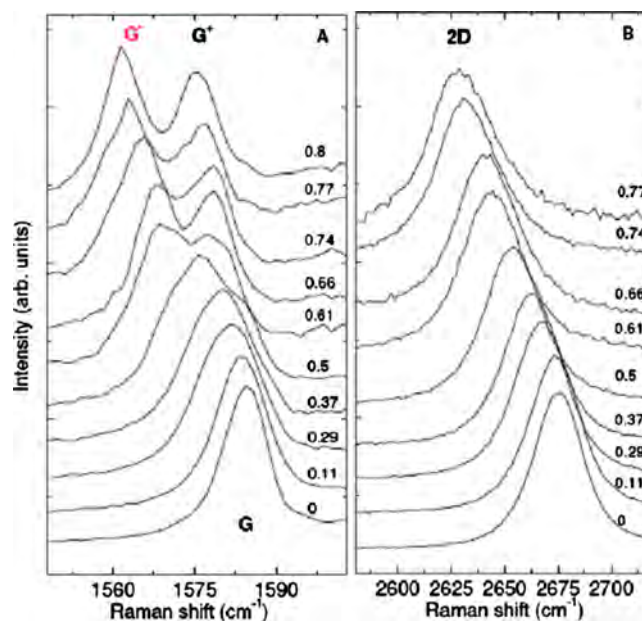


FIG. 29. (Color online) (a) List of Raman spectra, showing G and (b) 2D peaks as a function of uniaxial strain. The incident light polarized along the strain direction, and no analyzer was used to collect the scattered signal. The numbers on the right side of the spectra are indicating the strain. Reprinted with permission from Mohiuddin *et al.*, *Phys. Rev. B* 79, 205433 (2009). Copyright 2009 by the American Physical Society.

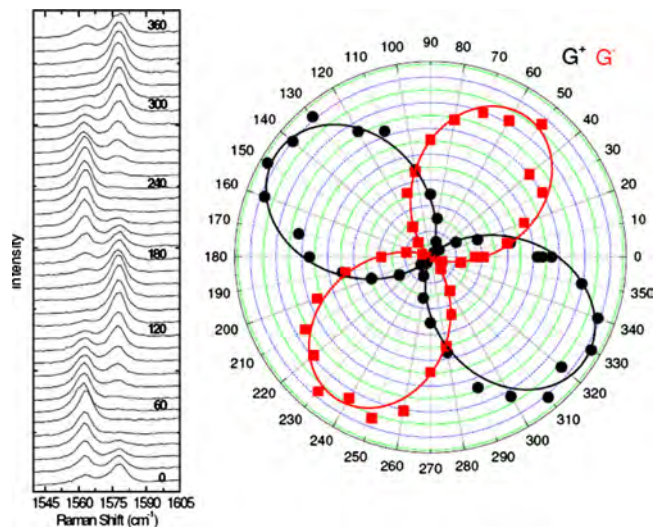


FIG. 30. (Color online) Raman spectra (left) and polar plot (right) of the G^+ and G^- peak intensity as a function of the angle between the polarization direction of the incident light and the strain axis. The spectra were collected with an analyzer direction along the strain axis. The polar data are fitted to $\varphi_s = 34^\circ$. Reprinted with permission from Mohiuddin *et al.*, Phys. Rev. B **79**, 205433 (2009). Copyright 2009 by the American Physical Society.

elongation of carbon bonds, and such band shift is found to be linearly related to the strain. Thus the Raman shift in G band and 2D band under strain can be used as a parameter to measure the value of uniaxial strain in graphene. Another results of uniaxial strain on graphene is the G band splitting. The single Lorentzian shape G band in unstrained graphene is a result of doubly degenerate optical phonon mode. After the application of strain, lowering of the graphene symmetry splits the two phonon mode apart, causing the appearance of the two branches of the G bands in strained graphene.^{328–330} Furthermore, the subbands G^+ and G^- due to G band splitting show different polarization dependence. This phenomenon can also be used to detect the angle between the graphene crystallographic orientation and applied strain, as shown in Fig. 30. By rotating the incident laser polarization and collecting scattered Raman signal along the strain direction, Raman intensity of G^+ band and G^- band can be fitted as $I_{G^+} \propto \cos^2(\theta_{in} + \varphi_s)$ and $I_{G^-} \propto \sin^2(\theta_{in} + \varphi_s)$, where θ_{in} is the angle between incident laser polarization and strain direction and φ_s is the desired crystallographic orientation (e.g., the direction of the C–C bond) with respect to the strain direction.

Biaxial strain was first observed in graphene epitaxially grown on SiC substrate. Due to the lattice mismatch between graphene and SiC substrate,^{331,332} the epitaxial graphene (EG) sustains a compress strain. Such biaxial strain would cause change in the whole phonon dispersion spectrum thus inducing a significant blueshift for G band and 2D band.^{333–335} Figure 31 shows a comparison between Raman spectra of single-layer EG, two-layer EG and those of single-layer mechanically exfoliated graphene and bulk graphite.^{333–335} The peak positions of the G band and 2D band were used to calculate the average compressive stress in the EG which turns out to be 2.27 GPa for the G band at $\sim 1597 \text{ cm}^{-1}$. Recently, Robinson *et al.*³³⁴ also used the Raman imaging technique to show that the strain of large area

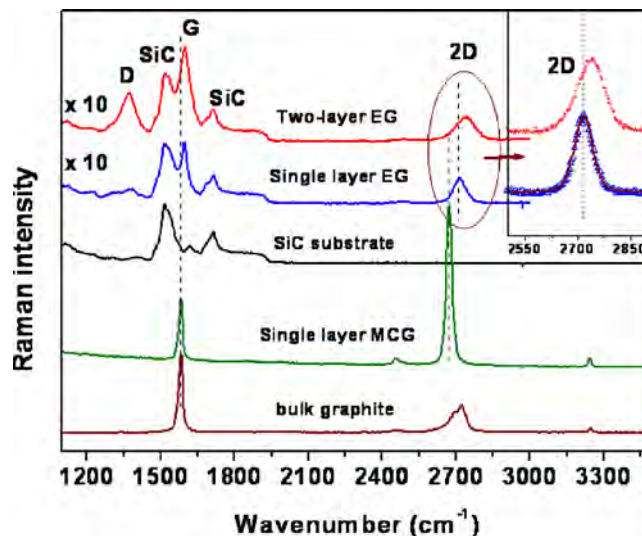


FIG. 31. (Color online) Raman spectra of epitaxial graphene grown on Si terminated SiC (Si–SiC) and C terminated SiC (C–SiC). Reprinted with permission from Ni *et al.*, Phys. Rev. B **77**, 115416 (2008). Copyright 2008 by the American Physical Society.

EG is not uniform. Apart from epitaxial graphene, the biaxial strain is also observed in graphene covered by insulators and after annealing.³²⁸

C. Raman study on the doping effect

As a potential candidate for future electronics, controllable doping is a key to the application of graphene. Raman spectroscopy is a powerful nondestructive tool to monitor the dopants concentration and the Fermi level changes in carbon nanomaterials.^{336,337} In graphene, there is strong electron–phonon coupling near the K point and Γ point. Such strong coupling causes the phonon softening near these two points, resulting phonon frequency and lifetime change.^{338–340} This phenomenon is called Kohn anomaly.³⁴¹ As a semimetal material, the Fermi level in graphene strongly affects the Kohn anomaly. By upshifting or downshifting the Fermi level, the electron–phonon coupling changes dramatically, thus resulting in the change in position and FWHM of both the G and 2D bands. In what follows, we review briefly such Raman studies on both intentional doping and unintentional doping in graphene.

The most common way of introducing intentional doping is by the gate effect. Gate effect is realized in following two setups for Raman study: back Si gate and top electrochemical gate. The doping effect on single layered graphene has been studied both theoretically and experimentally.^{53,342–344} Figures 32(a)–32(c) shows the Raman spectra of SLG with doping concentration tuned by a top gate, together with the adiabatic DFT calculation results. When the Fermi level moves away from the neutral point, the G band of single layered graphene becomes blueshifted and narrowing. On the other hand, because the phonon associated with the 2D band is far away from the Dirac point, the 2D band responses differently to the doping effect.

Raman study on bilayered graphene under doping effect has also been carried out. Due to the AB stacking structure,

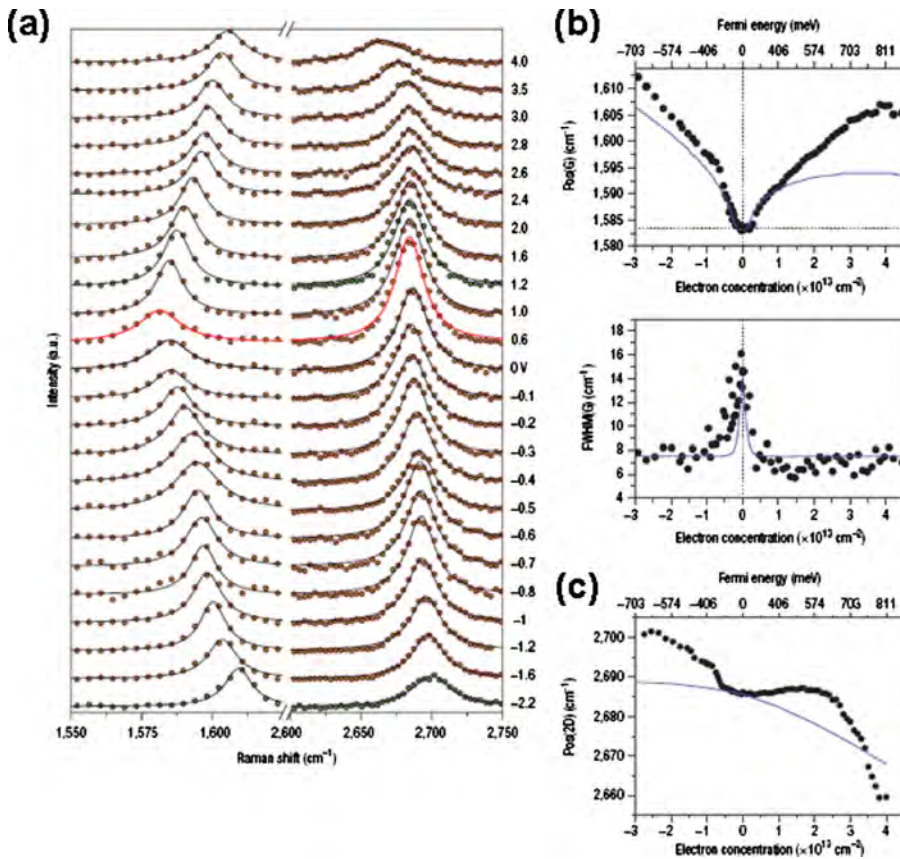


FIG. 32. (Color online) (a) Raman spectra at values of V_{TG} between -2.2 and $+4.0$ V. The dots are the experimental data, and the peaks are fitted by Lorentzians. The Dirac point is indicated by the red line. (b) Peak position of the G band (top panel) and its FWHM (bottom panel) as a function of electron and hole doping. The predicted nonadiabatic trends (Ref. 342) are shown in solid blue lines. (c) Peak position of the 2D peak as a function of doping. The solid line is their adiabatic DFT calculation. Reprinted with permission from Macmillan Publishers Ltd: Nature, Das *et al.*, 3, 210 (2008), Copyright 2008.

the electronic band structure and phonon mode in bilayer graphene is different from that of SLG, resulting in some interesting observations.^{345–347} Yan *et al.* carried out *in situ* Raman study at low temperature (17 K) to probe the electron–hole coupling with respect to the doping effect. At such a low temperature, while tuning the Fermi level away from the Dirac point, the G band frequency first appears redshifted then starts to blueshift at a high gate voltage, which agrees with the theoretical prediction.^{345–347}

Beside the study on intentional doping, unintentional doping is also attracting attentions. The extremely high surface/volume ratio makes graphene very sensitive to its environment. It is not always easy to avoid an unintentional doping caused by the substrate and ambient environment. Raman spectroscopy has been employed to probe the effect from such unintentional doping.^{348–351} Furthermore, Stampfer *et al.*³⁵² also applied Raman imaging technique to study the unintentional doped graphene and showed the possibility of using this technique to study the doping distributions.

Suspended free-standing graphene has been used to mimic samples free of unintentional doping from substrate.^{32,108} In suspended graphene samples, both G band and 2D band are redshifted as compared to that of the supported graphene, and the intensity ratio I_{2D}/I_G is also much higher in suspended graphene due to the extremely low charged impurities concentration.¹¹⁰ It is worth mentioning that Balandin *et al.*^{353,354} used Raman spectroscopy to measure local temperature of suspended graphene, and by studying the laser induced temperature change, the thermal conductivity of graphene has been deduced.

D. Raman study on misoriented bilayer graphene

Although the micromechanically cleaved graphene (MCG) provides a good platform to study the fundamental properties of graphene, future applications will rely on large scale graphene produced by other methods, like CVD, which have the ability to produce uniform graphene in large area. Pioneer works have been done to grow few layer graphene on metal films.^{158,160,161,170,180,193,355–361} Recently, Reina *et al.* successfully transferred the as-grown few layer graphene to an arbitrary substrate. Using Raman spectra, they found that such CVD grown graphene may not have ordered stacking, which in turn results in different electronic band structures.⁴⁷ Raman study on stacking disordered graphene together with simulation results may help to understand the properties of the CVD grown graphene. As the first step, one of the stacking disorder, misorientation in bilayer graphene has been demonstrated and studied using folded graphene sample by Ni *et al.*³⁶² and Poncharal *et al.*³⁶³ The folded graphene is favored because by knowing the exact crystallographic axes and the folding direction, the angle between the orientations of the two layers can be determined accurately. Figure 33(a) shows a piece of graphene sample with twofolded portions, together with a schematic diagram showing the folding directions of the twofolded pieces. Figure 33(b) shows the schematic diagram of the exact folding for the two sections, where the lower section of the folded section marked as Y has a misorientation of 12.5° between the top and bottom layers and the other section has a misorientation angle of about 7.5° . The Raman spectra recorded for the Y section is shown in Fig. 33(c) using excitation lasers at 457, 488, and

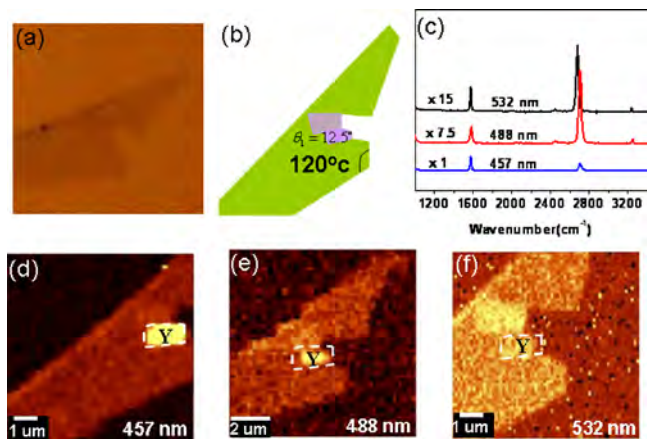


FIG. 33. (Color online) (a) Optical image of a SLG sheet contains folded (twisted) regions. (b) Schematically image of folded sample as shown in (a). The estimated twisted angle of top layer relative to the bottom layer is 12.3° . (c) Raman spectra of folded graphene from area Y when excited by 457, 488, and 532 nm laser. Raman imaging of the G band intensity of the graphene sample excited by 457 nm (d) and 488 nm (e) 532 nm lasers (f), respectively. As can be seen in (d), the G band intensity from area Y is much higher than that of SLG, which is ~ 15 times that of SLG. And this kind of enhanced G band intensity disappears when the excitation energy is 532 nm as shown in (f). The G band intensity from area Y is now the same as that of SLG. Therefore, there is a G band resonance for twisted bilayer graphene with rotation angle of $\sim 12.5^\circ$ under excitation energy of 457 nm (Ni *et al.*, unpublished work).

532 nm. It is clearly shown that Raman spectra are strongly dependent on laser excitation energy. Raman images of the G band intensity of the folded sample obtained using the 3 excitation wavelengths are illustrated in Figs. 33(d)–33(f). Again the dependence of the laser energy is clearly demonstrated. It is also noteworthy that the resonance G band intensity is also strongly dependent on the folding angle, i.e., angle of misorientation between the layers. For example, the folded graphene with 7.5° misorientation shows maximum G band intensity at 532 nm excitation, while maximum G band intensity for the Y section with 12.5° misorientation was observed with 457 nm laser excitation. This can be explained by first principle calculations that such G band resonance is due to the band folding and splitting in graphene layers that deviate from AB stacking.³⁶⁴

E. Raman study of the crystallographic orientation of graphene

Knowledge about the crystallographic axes and the chirality of its edges of graphene is vitally important for both fundamental understanding and any potential applications. For example, the electric properties of nanoscale graphene materials (e.g., GNRs) are greatly correlated with the chirality of its edges, and the study of misoriented graphene layers discussed in Sec. VI D requires knowledge on the crystallographic axes of the graphene layers.

Raman spectroscopy has been used as a routine tool to identify the chirality of CNTs,^{57,365–369} and it is still a distance away for it to become a mature tool to determine the edge state (armchair or zigzag) of graphene. Before the appearance of micromechanical cleavage graphene, Raman spectroscopy study on graphene edge has been carried out on step edges of HOPG surface.^{312,370} It was found that the D

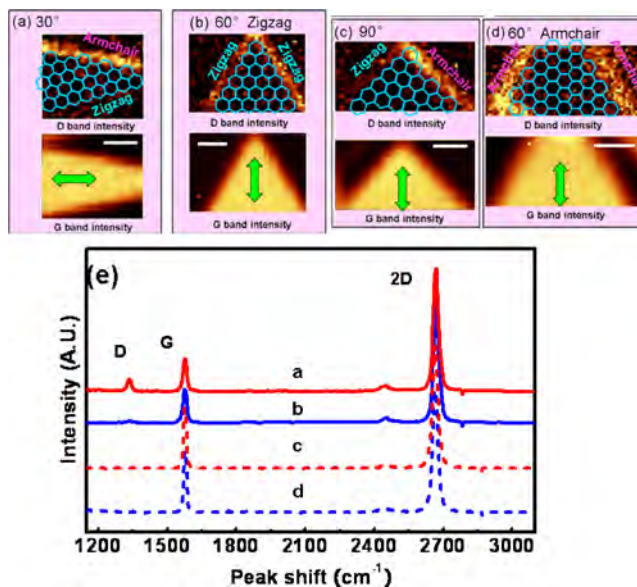


FIG. 34. (Color online) Raman imaging results from edges with angles (a) 30° , (b) 60° (zigzag), (c) 90° , and (d) 60° (armchair). The positions and shapes of the SLG sheets can be seen from the images constructed by the G band intensity. The laser polarization is indicated by the green arrows. The superimposed frameworks are guides for the eye indicating the edge state. Note that the edge state of (b) and (d) were determined by the other pair of edges (not shown) with $30^\circ/90^\circ$ on the same piece of SLG. The scale bar is $1 \mu\text{m}$. Adapted from You *et al.* (Ref. 371).

band only appears at the step edge of HOPG, and it shows strong polarization dependence. In the concept of double resonance process, the D band can only be observed at the armchair edges that provides elastic scattering of electrons to maintain momentum conservation, and it is shown that only in an armchair edges, the double resonance process can be fulfilled (stronger D band), while for zigzag edge, the resonance process is forbidden (weaker or vanished D band). Inspired by their results, Raman spectroscopy has been carried out to study and identify the edge state of MCG.^{371–373}

Being a 2D crystal, the cleavage angle of graphene is not arbitrary and it has been found that the angles between MCG edges, which are equivalent to the crystal planes in 3D crystals, have an average value equaling to multiples of 30° . It can be easily shown that, for the perfect graphene edge, when the angle between two adjacent edges is 30° , 90° , or 150° , both edges are of different edge state, one armchair and one zigzag. On the other hand, when the angle is 60° or 120° , both edges have the same edge state (either both zigzag or both armchair).^{371–373}

Strong polarization dependence of the D band Raman intensity from the edges was observed.^{372,373} Such dependence can be explained by the inhomogeneous optical absorption of the graphene.³⁷⁴ When the laser polarized along the graphene edge, the D band intensity is the highest. Figures 34(a)–34(d) show Raman images from edges using the D band intensity with angles (a) 30° with one zigzag and one armchair edges, (b) 60° (two zigzag edges), (c) 90° (one zigzag and one armchair), and (d) 60° (two armchair edges). The SLG sheets can be seen from the images constructed by the G band intensity shown below the D band images. To avoid the problem associated with the polarization depen-

dence of the D band from the edges, the laser polarization was chosen to be long the bisection of the two edges under study as indicated by the green arrows. The superimposed honeycomb frameworks are guides for the eye indicating the edge chirality. Note that the edge chirality of (b) and (d) was determined by the two other edges of the SLG samples (not shown) with $30^\circ/90^\circ$ edge angles.³⁷¹ Figure 34(e) shows Raman spectra on different position on a piece of SLG sheet with edges have the angle of 30° . All of the spectra were recorded under the same conditions. Spectra (a) and (b) were recorded on different edges.

In this section, the applications of Raman spectroscopy and imaging in the study of graphene have been reviewed briefly, with a particular focus on the characterization of various properties of graphene. Raman spectroscopy provides a convenient and versatile technique for the study of many aspects of graphene that are critical to the understanding and potential applications of graphene. Due to the page limit, many other applications in the study of graphene are not included, e.g., in sensing and H_2 uptake, etc.

VII. POTENTIAL APPLICATIONS OF 2D CARBON

The unique properties of 2D carbons make them attractive for many potential applications. As most of the applications are still at the exploratory, we just list out some of the applications reported so far.

A. Electronic devices

Ever since graphene has been discovered, there is always a high hope that it can be applied to high-performance electronic devices.²¹ Although exceptionally high values of mobility have been obtained in suspended graphene,^{30–32} the on-off ratio of large-width graphene FETs is low due to the existence of a minimum conductivity even at zero bias. Although the on-off ratios can be increased to a value which is comparable to that of nanotube FETs,¹²⁷ the mobility of such kind of GNR device tends to be much lower than the mobility observed in large and wide devices due to edge scattering. Therefore, the potential application of graphene might be in areas which require large current and high operation frequency instead of high on-off ratios.³⁷⁵ Compared to CNTs, graphene is more suitable for large current applications because it is easy to scale up the current by simply increasing the width of the device. Lin *et al.*³⁷⁵ have conducted a systematic study on the high-frequency response of top-gated graphene FETs with different channel lengths, by standard S -parameter measurements. The devices were made from mechanically exfoliated graphene sheets. A 12-nm-thick Al_2O_3 layer was used as the gate oxide which was deposited by atomic layer deposition at $250^\circ C$. The source/drain contacts were made of Ti (1 nm)/Pd (50 nm) bilayers. It was found that the cutoff frequency (f_T) is proportional to the dc transconductance g_m , following the relation $f_T = g_m / (2\pi C_G)$, where C_G is the gate capacitance, and increases with decreasing channel length (L_G), with the scaling dependence $f_T \sim 1/L_G^2$ for the devices studied. A peak cutoff frequency of 26 GHz was measured for a transistor with $L_G = 150$ nm. A

cutoff frequency approaching terahertz is achievable by further shortening the channel length and increase the carrier mobility.

B. Transparent conductive films

Transparent conductive films are highly demanded in transparent electronics. Several groups have demonstrated graphene composite films with high transparency, good conductivity, and superior mechanical properties.^{141,142,203,376–379} Majority of the transparent films was obtained from the solution route which involves the preparation of GO films followed by reduction to increase the conductivity. The advantages of using GO as the starting materials include the low cost and flexibility in controlling the optical and electrical properties through optimizing the reduction process and time. The drawback is that graphene sheets derived from GO tend to have a high density of defects, which may limit the performance of transparent electronic devices made from graphene. An alternative has been demonstrated by Kim *et al.* who have developed a method to produce transparent graphene films using graphene sheets synthesized by CVD. The graphene sheets were first grown on Ni films and then transferred to transparent substrate.²⁰³ The transferred graphene films showed a very low sheet resistance of 280 Ω per square with 80% optical transparency.

C. Mechanical devices

In addition to peculiar electronic properties, graphene also possesses superior mechanical properties. Lee *et al.*³⁸⁰ have measured the measured the mechanical properties of monolayer graphene membranes suspended over open holes using AFM nanoindentation. The force-displacement behavior obtained from the nanoindentation experiments is interpreted within a framework of nonlinear elastic stress-strain response, which yields second- and third-order elastic stiffnesses of 340 Nm^{-1} and -690 Nm^{-1} , respectively. The breaking strength is 42 Nm^{-1} . These quantities correspond to a Young's modulus of 1.0 TPa and intrinsic strength of 130 GPa, which establish graphene as the strongest material ever measured. The superior mechanical properties make graphene promising for applications in nanoelectromechanical systems^{318,381–385} or other flexible papers.³⁸⁶ Bunch *et al.*³¹⁸ have demonstrated nanoelectromechanical devices from SLG and MLG sheets by placing them over trenches in silicon oxide. The devices fabricated from graphene sheets with thicknesses ranging from one atomic layer to 75 nm exhibit fundamental resonant frequencies in the range of 1–170 MHz, with quality factor Q of 20–850. The high Young's modulus, extremely low mass, and large surface area make these nanometer scale mechanical devices ideally suited for sensing mass, force, and charges. Charge sensitivities down to $8 \times 10^{-4} e(\text{Hz})^{-1/2}$ have been obtained at room temperature.

D. Chemical sensors

By exposing both surfaces to the surrounding environment, SLG has the highest surface-to-volume ratio that can be achieved in any solids. This property makes graphene

natural choices as gas and chemical sensors.^{387–399} Ultrahigh sensitivity can be achieved through detecting the electrical, mechanical and optical properties induced by absorption of foreign atoms, molecule or charges. Schedin *et al.*³⁸⁷ have shown that it is possible to detect single gas molecular using a micrometer-sized sensor made from graphene. This is due to the fact that the absorbed gas molecules change the local carrier concentration in graphene one by one electron, which leads to step-like changes in resistance. The high sensitivity of graphene-based sensor is attributed to its low electronic noise. Although devices made from single piece of graphene is extremely sensitive, it might be so practical due to its high sensitivity to the surrounding environment as well. More practical sensors have been developed by using large quantity of graphene sheets derived from GOs as the sensing materials.^{395,399} Although these sensors are unable to detect single molecules, they are more stable than devices made from single piece of graphene sheet.

E. Spintronic devices

A typical spintronic device involves the generation/injection, transport, manipulation, storage and detection of spins or spin current.⁴⁰⁰ Materials with long spin diffusion length are desirable for application in lateral spin-valve type of devices. The spin diffusion length is determined by the spin relaxation mechanism in the materials. There are in general four mechanisms which have been found to be relevant for spin relaxation of conduction electrons in metals and semiconductors: the Elliott–Yafet (EY), D'yakonov–Perel' (DP), Bir–Aronov–Pikus (BAP), and hyperfine-interaction mechanisms.⁴⁰⁰ The EY and hyperfine-interaction mechanisms are common to most materials, whereas the DP becomes an efficient mechanism only in systems lacking inversion symmetry and the BAP is important only for spin relaxation of conduction electrons in *p*-doped semiconductors through scattering mediated spin exchange with holes. As both the EY and DP mechanisms have its origin in spin-orbit interactions, in general, a long spin diffusion length is expected for materials with small spin-orbit and hyperfine-interactions, such as the carbon allotropes. Spin transport and Larmor spin precession over micrometer-scale distances in single graphene layers have been demonstrated by several groups using nonlocal spin-dependent electrical measurement.^{401–405} High-efficiency spin-injection has been demonstrated in devices using both tunnel junctions,⁴⁰¹ and highly transparent electrodes.^{404,405} However, the local MR reported so far is still low as compared to all-metal spin-valves.

VIII. SUMMARY

Graphene is truly exceptional in various aspects including structural, mechanical, electronic, mechanical, thermal and possibly magnetic properties. In order to fully explore and make use of these properties, however, one must establish a viable technique to produce graphene in large quantity and in a controllable fashion. The fabrication processes must also be compatible with existing Si processes if it is to be used in electronic devices. This review has intended to give

an overview on the different synthesis and characterization techniques for 2D carbon nanostructures. Obviously, this has never been an easy task due to the rapid development in this field. It is the authors' hope that the information summarized in the review will serve as a reference for those who are interested in knowing different types of growth and characterization techniques for different types of 2D carbon nanostructures.

- ¹M. P. Marder, *Condensed Matter Physics* (Wiley, New York, 2000).
- ²M. S. Dresselhaus, G. Dresselhaus, and P. C. Eklund, *Science of Fullerenes and Carbon Nanotubes* (Academic, San Diego, 1996).
- ³S. Iijima, *Nature (London)* **354**, 56 (1991).
- ⁴R. Saito, G. Dresselhaus, and M. S. Dresselhaus, *Physical Properties of Carbon Nanotubes* (Imperial College Press, London, 1998).
- ⁵H. W. Kroto, J. R. Heath, S. C. O'Brien, R. F. Curl, and R. E. Smalley, *Nature (London)* **318**, 162 (1985).
- ⁶K. S. Novoselov, A. K. Geim, S. V. Morozov, D. Jiang, Y. Zhang, S. V. Dubonos, I. V. Grigorieva, and A. A. Firsov, *Science* **306**, 666 (2004).
- ⁷K. S. Novoselov, A. K. Geim, S. V. Morozov, D. Jiang, M. I. Katsnelson, I. V. Grigorieva, S. V. Dubonos, and A. A. Firsov, *Nature (London)* **438**, 197 (2005).
- ⁸Y. B. Zhang, Y. W. Tan, H. L. Stormer, and P. Kim, *Nature (London)* **438**, 201 (2005).
- ⁹A. Fasolino, J. H. Los, and M. I. Katsnelson, *Nature Mater.* **6**, 858 (2007).
- ¹⁰P. R. Wallace, *Phys. Rev.* **71**, 622 (1947).
- ¹¹J. W. McClure, *Phys. Rev.* **108**, 612 (1957).
- ¹²J. C. Slonczewski and P. R. Weiss, *Phys. Rev.* **109**, 272 (1958).
- ¹³G. W. Semenoff, *Phys. Rev. Lett.* **53**, 2449 (1984).
- ¹⁴A. H. C. Neto, F. Guinea, N. M. R. Peres, K. S. Novoselov, and A. K. Geim, *Rev. Mod. Phys.* **81**, 109 (2009).
- ¹⁵T. Ando, A. B. Fowler, and F. Stern, *Rev. Mod. Phys.* **54**, 437 (1982).
- ¹⁶M. I. Katsnelson, K. S. Novoselov, and A. K. Geim, *Nat. Phys.* **2**, 620 (2006).
- ¹⁷C. W. J. Beenakker, *Rev. Mod. Phys.* **80**, 1337 (2008).
- ¹⁸N. Stander, B. Huard, and D. Goldhaber-Gordon, *Phys. Rev. Lett.* **102**, 026807 (2009).
- ¹⁹A. Rycerz, J. Tworzydło, and C. W. J. Beenakker, *Nat. Phys.* **3**, 172 (2007).
- ²⁰A. Cresti, G. Grosso, and G. P. Parravicini, *Phys. Rev. B* **77**, 233402 (2008).
- ²¹A. K. Geim and K. S. Novoselov, *Nature Mater.* **6**, 183 (2007).
- ²²T. Ando, Y. S. Zheng, and H. Suzuura, *J. Phys. Soc. Jpn.* **71**, 1318 (2002).
- ²³K. Ziegler, *Phys. Rev. B* **75**, 233407 (2007).
- ²⁴S. Adam, E. H. Hwang, V. M. Galitski, and S. Das Sarma, *Proc. Natl. Acad. Sci. U.S.A.* **104**, 18392 (2007).
- ²⁵H. Suzuura and T. Ando, *Phys. Rev. Lett.* **89**, 266603 (2002).
- ²⁶E. McCann, K. Kechedzhi, V. I. Fal'ko, H. Suzuura, T. Ando, and B. L. Altshuler, *Phys. Rev. Lett.* **97**, 146805 (2006).
- ²⁷S. V. Morozov, K. S. Novoselov, M. I. Katsnelson, F. Schedin, L. A. Ponomarenko, D. Jiang, and A. K. Geim, *Phys. Rev. Lett.* **97**, 016801 (2006).
- ²⁸F. V. Tikhonenko, D. W. Horsell, R. V. Gorbachev, and A. K. Savchenko, *Phys. Rev. Lett.* **100**, 056802 (2008).
- ²⁹X. S. Wu, X. B. Li, Z. M. Song, C. Berger, and W. A. de Heer, *Phys. Rev. Lett.* **98**, 136801 (2007).
- ³⁰K. I. Bolotin, K. J. Sikes, Z. Jiang, M. Klima, G. Fudenberg, J. Hone, P. Kim, and H. L. Stormer, *Solid State Commun.* **146**, 351 (2008).
- ³¹M. Orlita, C. Faugeras, P. Plochocka, P. Neugebauer, G. Martinez, D. K. Maude, A. L. Barra, M. Sprinkle, C. Berger, W. A. de Heer, and M. Potemski, *Phys. Rev. Lett.* **101**, 267601 (2008).
- ³²X. Du, I. Skachko, A. Barker, and E. Y. Andrei, *Nat. Nanotechnol.* **3**, 491 (2008).
- ³³C. W. J. Beenakker, *Phys. Rev. Lett.* **97**, 067007 (2006).
- ³⁴Q. Y. Zhang, D. Y. Fu, B. G. Wang, R. Zhang, and D. Y. Xing, *Phys. Rev. Lett.* **101**, 047005 (2008).
- ³⁵W. A. de Heer, C. Berger, X. S. Wu, P. N. First, E. H. Conrad, X. B. Li, T. B. Li, M. Sprinkle, J. Hass, M. L. Sadowski, M. Potemski, and G. Martinez, *Solid State Commun.* **143**, 92 (2007).
- ³⁶J. Hass, W. A. de Heer, and E. H. Conrad, *J. Phys.: Condens. Matter* **20**, 323202 (2008).
- ³⁷N. R. Gall, E. V. Rut'kov, and A. Y. Tontegode, *Int. J. Mod. Phys. B* **11**,

- 1865 (1997).
- ³⁸C. Oshima and A. Nagashima, *J. Phys.: Condens. Matter* **9**, 1 (1997).
- ³⁹J. Wintterlin and M.-L. Bocquet, *Surf. Sci.* **603**, 1841 (2009).
- ⁴⁰S. J. Park and R. S. Ruoff, *Nat. Nanotechnol.* **4**, 217 (2009).
- ⁴¹Y. H. Wu, B. J. Yang, B. Y. Zong, H. Sun, Z. X. Shen, and Y. P. Feng, *J. Mater. Chem.* **14**, 469 (2004).
- ⁴²Y. H. Wu, P. W. Qiao, T. C. Chong, and Z. X. Shen, *Adv. Mater.* **14**, 64 (2002).
- ⁴³J. J. Wang, M. Y. Zhu, R. A. Outlaw, X. Zhao, D. M. Manos, B. C. Holloway, and V. P. Mammana, *Appl. Phys. Lett.* **85**, 1265 (2004).
- ⁴⁴M. Hiramatsu, K. Shiji, H. Amano, and M. Hori, *Appl. Phys. Lett.* **84**, 4708 (2004).
- ⁴⁵T. W. Ebbesen and P. M. Ajayan, *Nature (London)* **358**, 220 (1992).
- ⁴⁶G. D. Yuan, W. J. Zhang, Y. Yang, Y. B. Tang, Y. Q. Li, J. X. Wang, X. M. Meng, Z. B. He, C. M. L. Wu, I. Bello, C. S. Lee, and S. T. Lee, *Chem. Phys. Lett.* **467**, 361 (2009).
- ⁴⁷A. Reina, X. T. Jia, J. Ho, D. Nezich, H. B. Son, V. Bulovic, M. S. Dresselhaus, and J. Kong, *Nano Lett.* **9**, 30 (2009).
- ⁴⁸J. Hass, F. Varchon, J. E. Millan-Otoya, M. Sprinkle, N. Sharma, W. A. De Heer, C. Berger, P. N. First, L. Magaud, and E. H. Conrad, *Phys. Rev. Lett.* **100**, 125504 (2008).
- ⁴⁹P. Sutter, M. S. Hybertsen, J. T. Sadowski, and E. Sutter, *Nano Lett.* **9**, 2654 (2009).
- ⁵⁰A. K. Geim and A. H. MacDonald, *Phys. Today* **60**(8), 35 (2007).
- ⁵¹M. I. Katsnelson, *Mater. Today* **10**, 20 (2007).
- ⁵²T. Ando, *Physica E* **40**, 213 (2007).
- ⁵³A. C. Ferrari, *Solid State Commun.* **143**, 47 (2007).
- ⁵⁴L. M. Malard, M. A. Pimenta, G. Dresselhaus, and M. S. Dresselhaus, *Phys. Rep.* **473**, 51 (2009).
- ⁵⁵K. Sugihara, S. Ono, H. Oshima, K. Kawamura, and T. Tsuzuku, *J. Phys. Soc. Jpn.* **51**, 1900 (1982).
- ⁵⁶H. Ajiki and T. Ando, *J. Phys. Soc. Jpn.* **65**, 505 (1996).
- ⁵⁷R. Saito, G. Dresselhaus, and M. S. Dresselhaus, *Phys. Rev. B* **61**, 2981 (2000).
- ⁵⁸T. Ando, *J. Phys. Soc. Jpn.* **74**, 777 (2005).
- ⁵⁹T. Ando, T. Nakanishi, and R. Saito, *J. Phys. Soc. Jpn.* **67**, 2857 (1998).
- ⁶⁰P. L. McEuen, M. Bockrath, D. H. Cobden, Y. G. Yoon, and S. G. Louie, *Phys. Rev. Lett.* **83**, 5098 (1999).
- ⁶¹K. von Klitzing, G. Dorda, and M. Pepper, *Phys. Rev. Lett.* **45**, 494 (1980).
- ⁶²K. von Klitzing, *Rev. Mod. Phys.* **58**, 519 (1986).
- ⁶³J. W. McClure, *Phys. Rev.* **119**, 606 (1960).
- ⁶⁴J. W. McClure, *Phys. Rev.* **104**, 666 (1956).
- ⁶⁵R. S. Deacon, K. C. Chuang, R. J. Nicholas, K. S. Novoselov, and A. K. Geim, *Phys. Rev. B* **76**, 081406 (2007).
- ⁶⁶M. L. Sadowski, G. Martinez, M. Potemski, C. Berger, and W. A. de Heer, *Phys. Rev. Lett.* **97**, 266405 (2006).
- ⁶⁷G. Li and E. Y. Andrei, *Nat. Phys.* **3**, 623 (2007).
- ⁶⁸G. H. Li, A. Luican, and E. Y. Andrei, *Phys. Rev. Lett.* **102**, 176804 (2009).
- ⁶⁹D. L. Miller, K. D. Kubista, G. M. Rutter, M. Ruan, W. A. de Heer, P. N. First, and J. A. Stroscio, *Science* **324**, 924 (2009).
- ⁷⁰K. Nakada, M. Fujita, G. Dresselhaus, and M. S. Dresselhaus, *Phys. Rev. B* **54**, 17954 (1996).
- ⁷¹M. Fujita, K. Wakabayashi, K. Nakada, and K. Kusakabe, *J. Phys. Soc. Jpn.* **65**, 1920 (1996).
- ⁷²K. Wakabayashi, M. Fujita, H. Ajiki, and M. Sigrist, *Phys. Rev. B* **59**, 8271 (1999).
- ⁷³M. Ezawa, *Phys. Rev. B* **73**, 045432 (2006).
- ⁷⁴L. Brey and H. A. Fertig, *Phys. Rev. B* **73**, 235411 (2006).
- ⁷⁵K. I. Sasaki, S. Murakami, and R. Saito, *J. Phys. Soc. Jpn.* **75**, 074713 (2006).
- ⁷⁶Y. W. Son, M. L. Cohen, and S. G. Louie, *Phys. Rev. Lett.* **97**, 216803 (2006).
- ⁷⁷L. Yang, C. H. Park, Y. W. Son, M. L. Cohen, and S. G. Louie, *Phys. Rev. Lett.* **99**, 186801 (2007).
- ⁷⁸Y. W. Son, M. L. Cohen, and S. G. Louie, *Nature (London)* **444**, 347 (2006).
- ⁷⁹A. F. Young and P. Kim, *Nat. Phys.* **5**, 222 (2009).
- ⁸⁰G. A. Steele, G. Gotz, and L. P. Kouwenhoven, *Nat. Nanotechnol.* **4**, 363 (2009).
- ⁸¹D. Dragoman, *Phys. Scr.* **79**, 015003 (2009).
- ⁸²A. F. Morpurgo and F. Guinea, *Phys. Rev. Lett.* **97**, 196804 (2006).
- ⁸³F. Miao, S. Wijeratne, Y. Zhang, U. C. Coskun, W. Bao, and C. N. Lau, *Science* **317**, 1530 (2007).
- ⁸⁴R. Danneau, F. Wu, M. F. Craciun, S. Russo, M. Y. Tomi, J. Salmilehto, A. F. Morpurgo, and P. J. Hakonen, *Phys. Rev. Lett.* **100**, 196802 (2008).
- ⁸⁵E. H. Hwang, S. Adam, and S. Das Sarma, *Phys. Rev. Lett.* **98**, 186806 (2007).
- ⁸⁶T. Ando, *J. Phys. Soc. Jpn.* **75**, 074716 (2006).
- ⁸⁷K. Nomura and A. H. MacDonald, *Phys. Rev. Lett.* **98**, 076602 (2007).
- ⁸⁸V. V. Cheianov and V. I. Fal'ko, *Phys. Rev. Lett.* **97**, 226801 (2006).
- ⁸⁹V. F. Gantmakher, *Electrons and Disorder in Solids* (Clarendon/Oxford University Press, Oxford/New York, 2005).
- ⁹⁰Y. Imry, *Introduction to Mesoscopic Physics*, 2nd ed. (Oxford University Press, New York, 2001).
- ⁹¹X. Z. Yan and C. S. Ting, *Phys. Rev. Lett.* **101**, 126801 (2008).
- ⁹²R. V. Gorbachev, F. V. Tikhonenko, A. S. Mayorov, D. W. Horsell, and A. K. Savchenko, *Phys. Rev. Lett.* **98**, 176805 (2007).
- ⁹³F. V. Tikhonenko, A. A. Kozikov, A. K. Savchenko, and R. V. Gorbachev, *Phys. Rev. Lett.* **103**, 226801 (2009).
- ⁹⁴J. Tworzydło, B. Trauzettel, M. Titov, A. Rycerz, and C. W. J. Beenakker, *Phys. Rev. Lett.* **96**, 246802 (2006).
- ⁹⁵M. I. Katsnelson, *Eur. Phys. J. B* **51**, 157 (2006).
- ⁹⁶A. W. W. Ludwig, M. P. A. Fisher, R. Shankar, and G. Grinstein, *Phys. Rev. B* **50**, 7526 (1994).
- ⁹⁷K. Ziegler, *Phys. Rev. Lett.* **80**, 3113 (1998).
- ⁹⁸N. M. R. Peres, F. Guinea, and A. H. C. Neto, *Phys. Rev. B* **73**, 125411 (2006).
- ⁹⁹J. Cserti, *Phys. Rev. B* **75**, 033405 (2007).
- ¹⁰⁰P. M. Ostrovsky, I. V. Gornyi, and A. D. Mirlin, *Phys. Rev. B* **74**, 235443 (2006).
- ¹⁰¹S. Ryu, C. Mudry, A. Furusaki, and A. W. W. Ludwig, *Phys. Rev. B* **75**, 205344 (2007).
- ¹⁰²K. Ziegler, *Phys. Rev. Lett.* **97**, 266802 (2006).
- ¹⁰³V. P. Gusynin and S. G. Sharapov, *Phys. Rev. Lett.* **95**, 146801 (2005).
- ¹⁰⁴J. Martin, N. Akerman, G. Ulbricht, T. Lohmann, J. H. Smet, K. Von Klitzing, and A. Yacoby, *Nat. Phys.* **4**, 144 (2008).
- ¹⁰⁵Y. B. Zhang, V. W. Brar, C. Girit, A. Zettl, and M. F. Crommie, *Nature Physics* **5**, 722 (2009).
- ¹⁰⁶J. H. Chen, C. Jang, S. Adam, M. S. Fuhrer, E. D. Williams, and M. Ishigami, *Nat. Phys.* **4**, 377 (2008).
- ¹⁰⁷Y. W. Tan, Y. Zhang, K. Bolotin, Y. Zhao, S. Adam, E. H. Hwang, S. Das Sarma, H. L. Stormer, and P. Kim, *Phys. Rev. Lett.* **99**, 246803 (2007).
- ¹⁰⁸K. I. Bolotin, K. J. Sikes, J. Hone, H. L. Stormer, and P. Kim, *Phys. Rev. Lett.* **101**, 096802 (2008).
- ¹⁰⁹T. Stauber, N. M. R. Peres, and A. H. C. Neto, *Phys. Rev. B* **78**, 085418 (2008).
- ¹¹⁰Z. H. Ni, T. Yu, Z. Q. Luo, Y. Y. Wang, L. Liu, C. P. Wong, J. M. Miao, W. Huang, and Z. X. Shen, *ACS Nano* **3**, 569 (2009).
- ¹¹¹L. A. Ponomarenko, R. Yang, T. M. Mohiuddin, S. M. Morozov, A. A. Zhukov, F. Schedin, E. W. Hill, K. S. Novoselov, M. I. Katsnelson, and A. K. Geim, *Phys. Rev. Lett.* **102**, 206603 (2009).
- ¹¹²Y. Ando, X. Zhao, and M. Ohkohchi, *Carbon* **35**, 153 (1997).
- ¹¹³H. Hiura, T. W. Ebbesen, J. Fujita, K. Tanigaki, and T. Takada, *Nature (London)* **367**, 148 (1994).
- ¹¹⁴T. W. Ebbesen and H. Hiura, *Adv. Mater.* **7**, 582 (1995).
- ¹¹⁵T. M. Bernhardt, B. Kaiser, and K. Rademann, *Surf. Sci.* **408**, 86 (1998).
- ¹¹⁶H. V. Roy, C. Kallinger, B. Marsen, and K. Sattler, *J. Appl. Phys.* **83**, 4695 (1998).
- ¹¹⁷H. V. Roy, C. Kallinger, and K. Sattler, *Surf. Sci.* **407**, 1 (1998).
- ¹¹⁸X. Lu, M. Yu, H. Huang, and R. Ruoff, *Nanotechnology* **10**, 269 (1999).
- ¹¹⁹Y. B. Zhang, J. P. Small, W. V. Pontius, and P. Kim, *Appl. Phys. Lett.* **86**, 073104 (2005).
- ¹²⁰D. D. L. Chung, *J. Mater. Sci.* **22**, 4190 (1987).
- ¹²¹M. Inagaki, *J. Mater. Res.* **4**, 1560 (1989).
- ¹²²R. A. Greinke, R. A. Mercuri, and E. J. Beck, U.S. Patent No. 4895713 (January 23, 1990).
- ¹²³G. H. Chen, D. J. Wu, W. U. Weng, and C. L. Wu, *Carbon* **41**, 619 (2003).
- ¹²⁴G. H. Chen, W. G. Weng, D. J. Wu, C. L. Wu, J. R. Lu, P. P. Wang, and X. F. Chen, *Carbon* **42**, 753 (2004).
- ¹²⁵X. H. Chen, H. S. Yang, G. T. Wu, M. Wang, F. M. Deng, X. B. Zhang, J. C. Peng, and W. Z. Li, *J. Cryst. Growth* **218**, 57 (2000).
- ¹²⁶L. M. Viculis, J. J. Mack, O. M. Mayer, H. T. Hahn, and R. B. Kaner, *J. Mater. Chem.* **15**, 974 (2005).
- ¹²⁷X. L. Li, X. R. Wang, L. Zhang, S. W. Lee, and H. J. Dai, *Science* **319**, 1229 (2008).

- ¹²⁸B. C. Brodie, *Philos. Trans. R. Soc. London* **149**, 249 (1859).
- ¹²⁹W. S. Hummers, Jr. and R. E. Offeman, *J. Am. Chem. Soc.* **80**, 1339 (1958).
- ¹³⁰Z. S. Wu, W. C. Ren, L. B. Gao, J. P. Zhao, Z. P. Chen, B. L. Liu, D. M. Tang, B. Yu, C. B. Jiang, and H. M. Cheng, *ACS Nano* **3**, 411 (2009).
- ¹³¹S. Stankovich, D. A. Dikin, R. D. Piner, K. A. Kohlhaas, A. Kleinhammes, Y. Jia, Y. Wu, S. T. Nguyen, and R. S. Ruoff, *Carbon* **45**, 1558 (2007).
- ¹³²H. Kang, A. Kulkarni, S. Stankovich, R. S. Ruoff, and S. Baik, *Carbon* **47**, 1520 (2009).
- ¹³³G. K. Ramesha and S. Sampath, *J. Phys. Chem. C* **113**, 7985 (2009).
- ¹³⁴S. Horiuchi, T. Gotou, M. Fujiwara, T. Asaka, T. Yokosawa, and Y. Matsui, *Appl. Phys. Lett.* **84**, 2403 (2004).
- ¹³⁵S. Horiuchi, T. Gotou, M. Fujiwara, R. Sotoaka, M. Hirata, K. Kimoto, T. Asaka, T. Yokosawa, Y. Matsui, K. Watanabe, and M. Sekita, *Jpn. J. Appl. Phys., Part 2* **42**, L1073 (2003).
- ¹³⁶I. Jung, D. A. Dikin, R. D. Piner, and R. S. Ruoff, *Nano Lett.* **8**, 4283 (2008).
- ¹³⁷C. Gómez-Navarro, R. T. Weitz, A. M. Bittner, M. Scolari, A. Mews, M. Burghard, and K. Kern, *Nano Lett.* **7**, 3499 (2007).
- ¹³⁸M. J. Allen, J. D. Fowler, V. C. Tung, Y. Yang, B. H. Weiller, and R. B. Kaner, *Appl. Phys. Lett.* **93**, 193119 (2008).
- ¹³⁹K. N. Kudin, B. Ozbas, H. C. Schniepp, R. K. Prud'homme, I. A. Aksay, and R. Car, *Nano Lett.* **8**, 36 (2008).
- ¹⁴⁰K. A. Mkhoyan, A. W. Contryman, J. Silcox, D. A. Stewart, G. Eda, C. Mattevi, S. Miller, and M. Chhowalla, *Nano Lett.* **9**, 1058 (2009).
- ¹⁴¹G. Eda, G. Fanchini, and M. Chhowalla, *Nat. Nanotechnol.* **3**, 270 (2008).
- ¹⁴²H. A. Becerril, J. Mao, Z. Liu, R. M. Stoltenberg, Z. Bao, and Y. Chen, *ACS Nano* **2**, 463 (2008).
- ¹⁴³G. H. Chen, W. G. Weng, D. J. Wu, and C. L. Wu, *Eur. Polym. J.* **39**, 2329 (2003).
- ¹⁴⁴S. Stankovich, D. A. Dikin, G. H. B. Dommett, K. M. Kohlhaas, E. J. Zimney, E. A. Stach, R. D. Piner, S. T. Nguyen, and R. S. Ruoff, *Nature (London)* **442**, 282 (2006).
- ¹⁴⁵D. A. Dikin, S. Stankovich, E. J. Zimney, R. D. Piner, G. H. B. Dommett, G. Evmenenko, S. T. Nguyen, and R. S. Ruoff, *Nature (London)* **448**, 457 (2007).
- ¹⁴⁶D. W. Boukhvalov and M. I. Katsnelson, *J. Am. Chem. Soc.* **130**, 10697 (2008).
- ¹⁴⁷T. Nakajima, A. Mabuchi, and R. Hagiwara, *Carbon* **26**, 357 (1988).
- ¹⁴⁸T. Szabo, E. Tombacz, E. Illes, and I. Dekany, *Carbon* **44**, 537 (2006).
- ¹⁴⁹C. Hontoria-Lucas, A. J. López-Peinado, J. D. D. López-Gonzalez, M. L. Rojas-Cervantes, and R. M. Martín-Aranda, *Carbon* **33**, 1585 (1995).
- ¹⁵⁰T. Cassagneau, F. Guerin, and J. H. Fendler, *Langmuir* **16**, 7318 (2000).
- ¹⁵¹D. Li, M. B. Muller, S. Gilje, R. B. Kaner, and G. G. Wallace, *Nat. Nanotechnol.* **3**, 101 (2008).
- ¹⁵²S. Park, J. H. An, R. D. Piner, I. Jung, D. X. Yang, A. Velamakanni, S. T. Nguyen, and R. S. Ruoff, *Chem. Mater.* **20**, 6592 (2008).
- ¹⁵³Y. Si and E. T. Samulski, *Nano Lett.* **8**, 1679 (2008).
- ¹⁵⁴Y. Hernandez, V. Nicolosi, M. Lotya, F. M. Blighe, Z. Y. Sun, S. De, I. T. McGovern, B. Holland, M. Byrne, Y. K. Gun'ko, J. J. Boland, P. Niraj, G. Duesberg, S. Krishnamurthy, R. Goodhue, J. Hutchison, V. Scardaci, A. C. Ferrari, and J. N. Coleman, *Nat. Nanotechnol.* **3**, 563 (2008).
- ¹⁵⁵J. Hamilton and J. Blakely, *Surf. Sci.* **91**, 199 (1980).
- ¹⁵⁶J. T. Grant and T. W. Haas, *Surf. Sci.* **21**, 76 (1970).
- ¹⁵⁷Y. Pan, D. X. Shi, and H. J. Gao, *Chin. Phys.* **16**, 3151 (2007).
- ¹⁵⁸P. W. Sutter, J. I. Flege, and E. A. Sutter, *Nature Mater.* **7**, 406 (2008).
- ¹⁵⁹M. C. Wu, Q. Xu, and D. W. Goodman, *J. Phys. Chem.* **98**, 5104 (1994).
- ¹⁶⁰S. Marchini, S. Gunther, and J. Winterlin, *Phys. Rev. B* **76**, 075429 (2007).
- ¹⁶¹A. L. Vázquez de Parga, F. Calleja, B. Borca, M. C. G. Passeggi, J. J. Hinarejos, F. Guinea, and R. Miranda, *Phys. Rev. Lett.* **100**, 056807 (2008).
- ¹⁶²E. Loginova, N. C. Bartelt, P. J. Feibelman, and K. F. McCarty, *New J. Phys.* **10**, 093026 (2008).
- ¹⁶³D. Martocchia, P. R. Willmott, T. Brugger, M. Bjorck, S. Gunther, C. M. Schlepütz, A. Cervellino, S. A. Pauli, B. D. Patterson, S. Marchini, J. Winterlin, W. Moritz, and T. Greber, *Phys. Rev. Lett.* **101**, 126102 (2008).
- ¹⁶⁴D. E. Jiang, M. H. Du, and S. Dai, *J. Chem. Phys.* **130**, 074705 (2009).
- ¹⁶⁵M. C. Wu and D. W. Goodman, *J. Am. Chem. Soc.* **116**, 1364 (1994).
- ¹⁶⁶Y. Pan, H. G. Zhang, D. X. Shi, J. T. Sun, S. X. Du, F. Liu, and H. J. Gao, *Adv. Mater.* **21**, 277 (2009).
- ¹⁶⁷J. C. Shelton, H. R. Patil, and J. M. Blakely, *Surf. Sci.* **43**, 493 (1974).
- ¹⁶⁸M. Eizenberg and J. M. Blakely, *Surf. Sci.* **82**, 228 (1979).
- ¹⁶⁹R. Rosei, M. De Crescenzi, F. Sette, C. Quaresima, A. Savoia, and P. Perfetti, *Phys. Rev. B* **28**, 1161 (1983).
- ¹⁷⁰Y. Gamo, A. Nagashima, M. Wakabayashi, M. Terai, and C. Oshima, *Surf. Sci.* **374**, 61 (1997).
- ¹⁷¹Y. S. Dedkov, M. Fonin, U. Rüdiger, and C. Laubschat, *Phys. Rev. Lett.* **100**, 107602 (2008).
- ¹⁷²M. Fuentes-Cabrera, M. I. Baskes, A. V. Melechko, and M. L. Simpson, *Phys. Rev. B* **77**, 035405 (2008).
- ¹⁷³Y. S. Dedkov, M. Fonin, and C. Laubschat, *Appl. Phys. Lett.* **93**, 022509 (2008).
- ¹⁷⁴A. Varykhalov, J. Sánchez-Barriga, A. M. Shikin, C. Biswas, E. Ves-covo, A. Rybkin, D. Marchenko, and O. Rader, *Phys. Rev. Lett.* **101**, 157601 (2008).
- ¹⁷⁵T. Tanaka, A. Ito, A. Tajima, E. Rokuta, and C. Oshima, *Surf. Rev. Lett.* **10**, 721 (2003).
- ¹⁷⁶D. Usachov, A. M. Dobrotvorskii, A. Varykhalov, O. Rader, W. Gudat, A. M. Shikin, and V. K. Adamchuk, *Phys. Rev. B* **78**, 085403 (2008).
- ¹⁷⁷L. C. Isett and J. M. Blakely, *Surf. Sci.* **58**, 397 (1976).
- ¹⁷⁸B. E. Nieuwenhuys, D. I. Hagen, G. Rovida, and G. A. Somorjai, *Surf. Sci.* **59**, 155 (1976).
- ¹⁷⁹Z. Klusek, W. Kozłowski, Z. Waqar, S. Datta, J. S. Burnell-Gray, I. V. Makarenko, N. R. Gall, E. V. Rutkov, A. Y. Tontegode, and A. N. Titkov, *Appl. Surf. Sci.* **252**, 1221 (2005).
- ¹⁸⁰J. Coraux, A. T. N'Diaye, C. Busse, and T. Michely, *Nano Lett.* **8**, 565 (2008).
- ¹⁸¹A. T. N'Diaye, J. Coraux, T. N. Plasa, C. Busse, and T. Michely, *New J. Phys.* **10**, 043033 (2008).
- ¹⁸²A. B. Preobrajenski, M. L. Ng, A. S. Vinogradov, and N. Martensson, *Phys. Rev. B* **78**, 073401 (2008).
- ¹⁸³J. Coraux, A. T. N'Diaye, M. Engler, C. Busse, D. Wall, N. Buckanie, F. Heringdorf, R. van Gastel, B. Poelsema, and T. Michely, *New J. Phys.* **11**, 039801 (2009).
- ¹⁸⁴I. Pletikosić, M. Kralj, P. Pervan, R. Brako, J. Coraux, A. T. N'Diaye, C. Busse, and T. Michely, *Phys. Rev. Lett.* **102**, 056808 (2009).
- ¹⁸⁵D. G. Castner, B. A. Sexton, and G. A. Somorjai, *Surf. Sci.* **71**, 519 (1978).
- ¹⁸⁶K. Baron, D. W. Blakely, and G. A. Somorjai, *Surf. Sci.* **41**, 45 (1974).
- ¹⁸⁷T. A. Land, T. Michely, R. J. Behm, J. C. Hemminger, and G. Comsa, *Surf. Sci.* **264**, 261 (1992).
- ¹⁸⁸B. Lang, *Surf. Sci.* **53**, 317 (1975).
- ¹⁸⁹H. B. Lyon and G. A. Somorjai, *J. Chem. Phys.* **46**, 2539 (1967).
- ¹⁹⁰J. W. May, *Surf. Sci.* **17**, 267 (1969).
- ¹⁹¹A. E. Morgan and G. A. Somorjai, *Surf. Sci.* **12**, 405 (1968).
- ¹⁹²M. Sasaki, Y. Yamada, Y. Ogiwara, S. Yagyu, and S. Yamamoto, *Phys. Rev. B* **61**, 15653 (2000).
- ¹⁹³H. Ueta, M. Saida, C. Nakai, Y. Yamada, M. Sasaki, and S. Yamamoto, *Surf. Sci.* **560**, 183 (2004).
- ¹⁹⁴S. Hagstrom, H. B. Lyon, and G. A. Somorjai, *Phys. Rev. Lett.* **15**, 491 (1965).
- ¹⁹⁵Y. S. Li, W. W. Cai, J. H. An, S. Y. Kim, J. H. Nah, D. G. Yang, R. Piner, A. Velamakanni, I. H. Jung, E. Tutuc, S. K. Banerjee, L. Colombo, and R. S. Ruoff, *Science* **324**, 1312 (2009).
- ¹⁹⁶B. Wang, M. L. Bocquet, S. Marchini, S. Gähler, and J. Winterlin, *Phys. Chem. Chem. Phys.* **10**, 3530 (2008).
- ¹⁹⁷A. T. N'Diaye, S. Bleikamp, P. J. Feibelman, and T. Michely, *Phys. Rev. Lett.* **97**, 215501 (2006).
- ¹⁹⁸H. Kawanowa, H. Ozawa, T. Yazaki, Y. Gotoh, and R. Souda, *Jpn. J. Appl. Phys., Part 1* **41**, 6149 (2002).
- ¹⁹⁹V. M. Karpan, G. Giovannetti, P. A. Khomyakov, M. Talanana, A. A. Starikov, M. Zwierzycki, J. van den Brink, G. Brocks, and P. J. Kelly, *Phys. Rev. Lett.* **99**, 176602 (2007).
- ²⁰⁰G. Bertoni, L. Calmels, A. Altibelli, and V. Scrin, *Phys. Rev. B* **71**, 075402 (2005).
- ²⁰¹G. Giovannetti, P. A. Khomyakov, G. Brocks, V. M. Karpan, J. van den Brink, and P. J. Kelly, *Phys. Rev. Lett.* **101**, 026803 (2008).
- ²⁰²Q. K. Yu, J. Lian, S. Siriponglert, H. Li, Y. P. Chen, and S. S. Pei, *Appl. Phys. Lett.* **93**, 113103 (2008).
- ²⁰³K. S. Kim, Y. Zhao, H. Jang, S. Y. Lee, J. M. Kim, J. H. Ahn, P. Kim, J. Y. Choi, and B. H. Hong, *Nature (London)* **457**, 706 (2009).
- ²⁰⁴T. Aizawa, R. Souda, Y. Ishizawa, H. Hirano, T. Yamada, K. I. Tanaka, and C. Oshima, *Surf. Sci.* **237**, 194 (1990).
- ²⁰⁵T. Aizawa, Y. Hwang, W. Hayami, R. Souda, S. Otani, and Y. Ishizawa, *Surf. Sci.* **260**, 311 (1992).

- ²⁰⁶A. Nagashima, N. Tejima, and C. Oshima, *Phys. Rev. B* **50**, 17487 (1994).
- ²⁰⁷F. J. Himpsel, K. Christmann, P. Heimann, D. E. Eastman, and P. J. Feibelman, *Surf. Sci.* **115**, L159 (1982).
- ²⁰⁸A. J. Van Bommel, J. E. Crombeen, and A. Van Tooren, *Surf. Sci.* **48**, 463 (1975).
- ²⁰⁹L. Muehlhoff, W. J. Choyke, M. J. Bozack, and J. T. Yates, *J. Appl. Phys.* **60**, 2842 (1986).
- ²¹⁰I. Forbeaux, J. M. Themlin, and J. M. Debever, *Phys. Rev. B* **58**, 16396 (1998).
- ²¹¹I. Forbeaux, J. M. Themlin, and J. M. Debever, *Surf. Sci.* **442**, 9 (1999).
- ²¹²C. Berger, Z. M. Song, T. B. Li, X. B. Li, A. Y. Ogbazghi, R. Feng, Z. T. Dai, A. N. Marchenkov, E. H. Conrad, P. N. First, and W. A. de Heer, *J. Phys. Chem. B* **108**, 19912 (2004).
- ²¹³C. Berger, Z. M. Song, X. B. Li, X. S. Wu, N. Brown, C. Naud, D. Mayou, T. B. Li, J. Hass, A. N. Marchenkov, E. H. Conrad, P. N. First, and W. A. de Heer, *Science* **312**, 1191 (2006).
- ²¹⁴V. Ramachandran, M. F. Brady, A. R. Smith, R. M. Feenstra, and D. W. Greve, *J. Electron. Mater.* **27**, 308 (1998).
- ²¹⁵M. E. Lin, S. Strite, A. Agarwal, A. Salvador, G. L. Zhou, N. Teraguchi, A. Rockett, and H. Morkoc, *Appl. Phys. Lett.* **62**, 702 (1993).
- ²¹⁶F. Owman, C. Hallin, P. Mårtensson, and E. Janzén, *J. Cryst. Growth* **167**, 391 (1996).
- ²¹⁷L. Liu and J. H. Edgar, *Mater. Sci. Eng. R.* **37**, 61 (2002).
- ²¹⁸M. A. Kulakov, G. Henn, and B. Bullemer, *Surf. Sci.* **346**, 49 (1996).
- ²¹⁹L. Li and I. S. T. Tsong, *Surf. Sci.* **351**, 141 (1996).
- ²²⁰U. Starke, *Phys. Status Solidi B* **202**, 475 (1997).
- ²²¹R. M. Tromp and J. B. Hannon, *Phys. Rev. Lett.* **102**, 106104 (2009).
- ²²²U. Starke and C. Riedl, *J. Phys.: Condens. Matter* **21**, 134016 (2009).
- ²²³L. Li, Y. Hasegawa, T. Sakurai, and I. S. T. Tsong, *J. Appl. Phys.* **80**, 2524 (1996).
- ²²⁴X. N. Xie, H. Q. Wang, A. T. S. Wee, and K. P. Loh, *Surf. Sci.* **478**, 57 (2001).
- ²²⁵K. V. Emtsev, A. Bostwick, K. Horn, J. Jobst, G. L. Kellogg, L. Ley, J. L. McChesney, T. Ohta, S. A. Reshanov, J. Rohrl, E. Rotenberg, A. K. Schmid, D. Waldmann, H. B. Weber, and T. Seyller, *Nature Mater.* **8**, 203 (2009).
- ²²⁶J. Hass, R. Feng, T. Li, X. Li, Z. Zong, W. A. de Heer, P. N. First, E. H. Conrad, C. A. Jeffrey, and C. Berger, *Appl. Phys. Lett.* **89**, 143106 (2006).
- ²²⁷J. Hass, R. Feng, J. E. Millan-Otoya, X. Li, M. Sprinkle, P. N. First, W. A. de Heer, E. H. Conrad, and C. Berger, *Phys. Rev. B* **75**, 214109 (2007).
- ²²⁸S. Iijima, T. Wakabayashi, and Y. Achiba, *J. Phys. Chem.* **100**, 5839 (1996).
- ²²⁹Y. H. Wu and T. C. Chong, 2001 MRS Spring Meeting, San Francisco, 16–20 April 2001, Abstract No. W8.3.
- ²³⁰Y. H. Wu and B. J. Yang, *Nano Lett.* **2**, 355 (2002).
- ²³¹K. Tanaka, M. Yoshimura, A. Okamoto, and K. Ueda, *Jpn. J. Appl. Phys., Part 1* **44**, 2074 (2005).
- ²³²A. T. H. Chuang, B. O. Boskovic, and J. Robertson, *Diamond Relat. Mater.* **15**, 1103 (2006).
- ²³³A. T. H. Chuang, J. Robertson, B. O. Boskovic, and K. K. K. Koziol, *Appl. Phys. Lett.* **90**, 123107 (2007).
- ²³⁴L. Le Brizoual, M. Belmahi, H. Chatei, M. B. Assouar, and J. Bougdira, *Diamond Relat. Mater.* **16**, 1244 (2007).
- ²³⁵L. Y. Zeng, D. Lei, W. B. Wang, J. Q. Liang, Z. Q. Wang, N. Yao, and B. L. Zhang, *Appl. Surf. Sci.* **254**, 1700 (2008).
- ²³⁶S. Vizireanu, L. Nistor, M. Haupt, V. Katzenmaier, C. Oehr, and G. Dinescu, *Plasma Processes Polym.* **5**, 263 (2008).
- ²³⁷A. Malesevic, R. Vitchev, K. Schouteden, A. Volodin, L. Zhang, G. V. Tendeloo, A. Vanhulsel, and C. V. Haesendonck, *Nanotechnology* **19**, 305604 (2008).
- ²³⁸J. J. Wang, M. Y. Zhu, R. A. Outlaw, X. Zhao, D. M. Manos, and B. C. Holloway, *Carbon* **42**, 2867 (2004).
- ²³⁹K. Nishimura, N. Jiang, and A. Hiraki, *IEICE Trans. Electron.* **E86-C**, 821 (2003).
- ²⁴⁰S. Kurita, A. Yoshimura, H. Kawamoto, T. Uchida, K. Kojima, M. Tachibana, P. Molina-Morales, and H. Nakai, *J. Appl. Phys.* **97**, 104320 (2005).
- ²⁴¹C. R. Lin, C. H. Su, C. Y. Chang, C. H. Hung, and Y. F. Huang, *Surf. Coat. Technol.* **200**, 3190 (2006).
- ²⁴²G. Sato, T. Morio, T. Kato, and R. Hatakeyama, *Jpn. J. Appl. Phys., Part 1* **45**, 5210 (2006).
- ²⁴³A. Malesevic, S. Vizireanu, R. Kemps, A. Vanhulsel, C. Van Haesendonck, and G. Dinescu, *Carbon* **45**, 2932 (2007).
- ²⁴⁴S. Kondo, M. Hori, K. Yamakawa, S. Den, H. Kano, and M. Hiramatsu, *J. Vac. Sci. Technol. B* **26**, 1294 (2008).
- ²⁴⁵M. Y. Zhu, J. J. Wang, R. A. Outlaw, K. Hou, D. M. Manos, and B. C. Holloway, *Diamond Relat. Mater.* **16**, 196 (2007).
- ²⁴⁶N. G. Shang, F. C. K. Au, X. M. Meng, C. S. Lee, I. Bello, and S. T. Lee, *Chem. Phys. Lett.* **358**, 187 (2002).
- ²⁴⁷T. Dikonimos, L. Giorgi, R. Giorgi, N. Lisi, E. Salernitano, and R. Rossi, *Diamond Relat. Mater.* **16**, 1240 (2007).
- ²⁴⁸L. Giorgi, T. D. Makris, R. Giorgi, N. Lisi, and E. Salernitano, *Sens. Actuators B* **126**, 144 (2007).
- ²⁴⁹S. Shimabukuro, Y. Hatakeyama, M. Takeuchi, T. Itoh, and S. Nonomura, *Jpn. J. Appl. Phys.* **47**, 8635 (2008).
- ²⁵⁰B. J. Yang, Ph.D. thesis, National University of Singapore, 2004.
- ²⁵¹K. Shiji, M. Hiramatsu, A. Enomoto, N. Nakamura, H. Amano, and M. Hori, *Diamond Relat. Mater.* **14**, 831 (2005).
- ²⁵²T. Mori, M. Hiramatsu, K. Yamakawa, K. Takeda, and M. Hori, *Diamond Relat. Mater.* **17**, 1513 (2008).
- ²⁵³M. Y. Zhu, J. J. Wang, B. C. Holloway, R. A. Outlaw, X. Zhao, K. Hou, V. Shutthanandan, and D. M. Manos, *Carbon* **45**, 2229 (2007).
- ²⁵⁴B. L. French, J. J. Wang, M. Y. Zhu, and B. C. Holloway, *J. Appl. Phys.* **97**, 114317 (2005).
- ²⁵⁵Z. H. Ni, H. M. Fan, Y. P. Feng, Z. X. Shen, B. J. Yang, and Y. H. Wu, *J. Chem. Phys.* **124**, 204703 (2006).
- ²⁵⁶K. Kobayashi, M. Tanimura, H. Nakai, A. Yoshimura, H. Yoshimura, K. Kojima, and M. Tachibana, *J. Appl. Phys.* **101**, 094306 (2007).
- ²⁵⁷G. Mie, *Ann. Phys.* **330**, 377 (1908).
- ²⁵⁸L. Y. Cao, D. N. Barsic, A. R. Guichard, and M. L. Brongersma, *Nano Lett.* **7**, 3523 (2007).
- ²⁵⁹D. A. Boyd, L. Greengard, M. Brongersma, M. Y. El-Naggar, and D. G. Goodwin, *Nano Lett.* **6**, 2592 (2006).
- ²⁶⁰D. B. Shao and S. C. Chen, *Nano Lett.* **6**, 2279 (2006).
- ²⁶¹S. G. Wang, J. J. Wang, P. Miraldo, M. Y. Zhu, R. Outlaw, K. Hou, X. Zhao, B. C. Holloway, D. Manos, T. Tyler, O. Shenderova, M. Ray, J. Dalton, and G. McGuire, *Appl. Phys. Lett.* **89**, 183103 (2006).
- ²⁶²T. Tyler, O. Shenderova, M. Ray, J. Dalton, J. Wang, R. Outlaw, M. Zhu, X. Zhao, G. McGuire, and B. C. Holloway, *J. Vac. Sci. Technol. B* **24**, 2295 (2006).
- ²⁶³S. Chhoker, S. K. Arora, P. Srivastava, and V. D. Vankar, *J. Nanosci. Nanotechnol.* **8**, 4309 (2008).
- ²⁶⁴A. Malesevic, R. Kemps, A. Vanhulsel, M. P. Chowdhury, A. Volodin, and C. Van Haesendonck, *J. Appl. Phys.* **104**, 084301 (2008).
- ²⁶⁵M. Y. Chen, C. M. Yeh, J. S. Syu, J. Hwang, and C. S. Kou, *Nanotechnology* **18**, 185706 (2007).
- ²⁶⁶M. Araidai, Y. Nakamura, and K. Watanabe, *Phys. Rev. B* **70**, 245410 (2004).
- ²⁶⁷D. C. Elias, R. R. Nair, T. M. G. Mohiuddin, S. V. Morozov, P. Blake, M. P. Halsall, A. C. Ferrari, D. W. Boukhvalov, M. I. Katsnelson, A. K. Geim, and K. S. Novoselov, *Science* **323**, 610 (2009).
- ²⁶⁸Z. Q. Luo, T. Yu, K. J. Kim, Z. H. Ni, Y. M. You, Z. X. Shen, S. Z. Wang, and J. Y. Li, *ACS Nano* **3**, 1781 (2009).
- ²⁶⁹H. M. Wang, C. Choong, J. Zhang, K. L. Teo, and Y. H. Wu, *Solid State Commun.* **145**, 341 (2008).
- ²⁷⁰Y. H. Wu, B. J. Yang, G. C. Han, B. Y. Zong, H. Q. Ni, P. Luo, T. C. Chong, T. S. Low, and Z. X. Shen, *Adv. Funct. Mater.* **12**, 489 (2002).
- ²⁷¹Z. H. Chen, Y. M. Lin, M. J. Rooks, and P. Avouris, *Physica E (Amsterdam)* **40**, 228 (2007).
- ²⁷²M. Y. Han, B. Ozyilmaz, Y. B. Zhang, and P. Kim, *Phys. Rev. Lett.* **98**, 206805 (2007).
- ²⁷³M. C. Lemme, D. C. Bell, J. R. Williams, L. A. Stern, B. W. H. Baugher, P. Jarillo-Herrero, and C. M. Marcus, *ACS Nano* **2009** **3**, 2674 (2009).
- ²⁷⁴D. C. Bell, M. C. Lemme, L. A. Stern, J. R. Williams, and C. M. Marcus, *Nanotechnology* **20**, 455301 (2009).
- ²⁷⁵B. Banerjee and P. Walker, Jr., *J. Appl. Phys.* **33**, 229 (1962).
- ²⁷⁶J. Meyer, A. Geim, M. Katsnelson, K. Novoselov, T. Booth, and S. Roth, *Nature (London)* **446**, 60 (2007).
- ²⁷⁷R. E. Peierls, *Helv. Phys. Acta Suppl.* **7**, 81 (1934).
- ²⁷⁸J. C. Meyer, C. Kisielowski, R. Erni, M. D. Rossell, M. F. Crommie, and A. Zettl, *Nano Lett.* **8**, 3582 (2008).
- ²⁷⁹M. H. Gass, U. Bangert, A. L. Bleloch, P. Wang, R. R. Nair, and A. K. Geim, *Nat. Nanotechnol.* **3**, 676 (2008).
- ²⁸⁰F. Banhart, *Rep. Prog. Phys.* **62**, 1181 (1999).
- ²⁸¹Y. W. Son, M. L. Cohen, and S. G. Louie, *Nature (London)* **446**, 342

- (2007).
- ²⁸²Z. Liu, K. Suenaga, P. J. F. Harris, and S. Iijima, *Phys. Rev. Lett.* **102**, 015501 (2009).
- ²⁸³D. J. Klein, *Chem. Phys. Lett.* **217**, 261 (1994).
- ²⁸⁴C. O. Girit, J. C. Meyer, R. Erni, M. D. Rossell, C. Kisielowski, L. Yang, C. H. Park, M. F. Crommie, M. L. Cohen, S. G. Louie, and A. Zettl, *Science* **323**, 1705 (2009).
- ²⁸⁵X. T. Jia, M. Hofmann, V. Meunier, B. G. Sumpter, J. Campos-Delgado, J. M. Romo-Herrera, H. B. Son, Y. P. Hsieh, A. Reina, J. Kong, M. Terrones, and M. S. Dresselhaus, *Science* **323**, 1701 (2009).
- ²⁸⁶J. H. Warner, M. H. Rummeli, T. Gemming, B. Buchner, and G. A. D. Briggs, *Nano Lett.* **9**, 102 (2009).
- ²⁸⁷J. C. Meyer, C. O. Girit, M. F. Crommie, and A. Zettl, *Appl. Phys. Lett.* **92**, 123110 (2008).
- ²⁸⁸M. D. Fischbein and M. Drndic, *Appl. Phys. Lett.* **93**, 113107 (2008).
- ²⁸⁹H. Itoh, T. Ichinose, C. Oshima, T. Ichinokawa, and T. Aizawa, *Surf. Sci.* **254**, L437 (1991).
- ²⁹⁰G. M. Rutter, N. P. Guisinger, J. N. Crain, E. A. A. Jarvis, M. D. Stiles, T. Li, P. N. First, and J. A. Stroscio, *Phys. Rev. B* **76**, 235416 (2007).
- ²⁹¹F. Hiebel, P. Mallet, F. Varchon, L. Magaud, and J. Y. Veuillen, *Phys. Rev. B* **78**, 153412 (2008).
- ²⁹²V. W. Brar, Y. Zhang, Y. Yayon, T. Ohta, J. L. McChesney, A. Bostwick, E. Rotenberg, K. Horn, and M. F. Crommie, *Appl. Phys. Lett.* **91**, 122102 (2007).
- ²⁹³Z. Klusek, P. Dabrowski, P. Kowalczyk, W. Kozłowski, P. Blake, M. Szybowicz, T. Runka, and W. Olejniczak, *Appl. Phys. Lett.* **95**, 113114 (2009).
- ²⁹⁴G. M. Rutter, J. N. Crain, N. P. Guisinger, T. Li, P. N. First, and J. A. Stroscio, *Science* **317**, 219 (2007).
- ²⁹⁵P. Mallet, F. Varchon, C. Naud, L. Magaud, C. Berger, and J. Y. Veuillen, *Phys. Rev. B* **76**, 041403 (2007).
- ²⁹⁶Z. Waqar, I. V. Makarenko, A. N. Titkov, N. R. Gall, E. V. Rutkov, A. Y. Tontegode, and P. Dumas, *J. Mater. Res.* **19**, 1058 (2004).
- ²⁹⁷L. Simon, C. Bena, F. Vonau, D. Aubel, H. Nasrallah, M. Habar, and J. C. Peruchetti, *Eur. Phys. J. B* **69**, 351 (2009).
- ²⁹⁸H. Huang, W. Chen, S. Chen, and A. T. S. Wee, *ACS Nano* **2**, 2513 (2008).
- ²⁹⁹T. Enoki, Y. Kobayashi, and K. I. Fukui, *Int. Rev. Phys. Chem.* **26**, 609 (2007).
- ³⁰⁰L. Tapasztó, G. Dobrik, P. Lambin, and L. P. Biro, *Nat. Nanotechnol.* **3**, 397 (2008).
- ³⁰¹K. A. Ritter and J. W. Lyding, *Nature Mater.* **8**, 235 (2009).
- ³⁰²E. Stolyarova, K. T. Rim, S. M. Ryu, J. Maultzsch, P. Kim, L. E. Brus, T. F. Heinz, M. S. Hybertsen, and G. W. Flynn, *Proc. Natl. Acad. Sci. U.S.A.* **104**, 9209 (2007).
- ³⁰³M. Ishigami, J. H. Chen, W. G. Cullen, M. S. Fuhrer, and E. D. Williams, *Nano Lett.* **7**, 1643 (2007).
- ³⁰⁴A. Deshpande, W. Bao, F. Miao, C. N. Lau, and B. J. LeRoy, *Phys. Rev. B* **79**, 205411 (2009).
- ³⁰⁵Y. B. Zhang, V. W. Brar, F. Wang, C. Girit, Y. Yayon, M. Panlasigui, A. Zettl, and M. F. Crommie, *Nat. Phys.* **4**, 627 (2008).
- ³⁰⁶T. O. Wehling, I. Grigorenko, A. I. Lichtenstein, and A. V. Balatsky, *Phys. Rev. Lett.* **101**, 216803 (2008).
- ³⁰⁷C. H. Park, F. Giustino, M. L. Cohen, and S. G. Louie, *Phys. Rev. Lett.* **99**, 086804 (2007).
- ³⁰⁸M. L. Teague, A. P. Lai, J. Velasco, C. R. Hughes, A. D. Beyer, M. W. Bockrath, C. N. Lau, and N.-C. Yeh, *Nano Lett.* **9**, 2542 (2009).
- ³⁰⁹A. Gupta, G. Chen, P. Joshi, S. Tadigadapa, and P. C. Eklund, *Nano Lett.* **6**, 2667 (2006).
- ³¹⁰A. C. Ferrari, J. C. Meyer, V. Scardaci, C. Casiraghi, M. Lazzeri, F. Mauri, S. Piscanec, D. Jiang, K. S. Novoselov, S. Roth, and A. K. Geim, *Phys. Rev. Lett.* **97**, 187401 (2006).
- ³¹¹Z. H. Ni, H. M. Wang, J. Kasim, H. M. Fan, T. Yu, Y. H. Wu, Y. P. Feng, and Z. X. Shen, *Nano Lett.* **7**, 2758 (2007).
- ³¹²M. A. Pimenta, G. Dresselhaus, M. S. Dresselhaus, L. G. Cancado, A. Jorio, and R. Saito, *Phys. Chem. Chem. Phys.* **9**, 1276 (2007).
- ³¹³S. Reich and C. Thomsen, *Philos. Trans. R. Soc. London, Ser. A* **362**, 2271 (2004).
- ³¹⁴M. S. Dresselhaus and P. C. Eklund, *Adv. Phys.* **49**, 705 (2000).
- ³¹⁵M. S. Dresselhaus, G. Dresselhaus, R. Saito, and A. Jorio, *Phys. Rep.* **409**, 47 (2005).
- ³¹⁶C. Thomsen and S. Reich, *Phys. Rev. Lett.* **85**, 5214 (2000).
- ³¹⁷L. G. Cançado, A. Reina, J. Kong, and M. S. Dresselhaus, *Phys. Rev. B* **77**, 245408 (2008).
- ³¹⁸J. S. Bunch, A. M. van der Zande, S. S. Verbridge, I. W. Frank, D. M. Tanenbaum, J. M. Parpia, H. G. Craighead, and P. L. McEuen, *Science* **315**, 490 (2007).
- ³¹⁹Y. Y. Wang, Z. H. Ni, Z. X. Shen, H. M. Wang, and Y. H. Wu, *Appl. Phys. Lett.* **92**, 043121 (2008).
- ³²⁰D. Graf, F. Molitor, K. Ensslin, C. Stampfer, A. Jungen, C. Hierold, and L. Wirtz, *Nano Lett.* **7**, 238 (2007).
- ³²¹S. B. Cronin, A. K. Swan, M. S. Unlu, B. B. Goldberg, M. S. Dresselhaus, and M. Tinkham, *Phys. Rev. Lett.* **93**, 167401 (2004).
- ³²²M. D. Frogley, Q. Zhao, and H. D. Wagner, *Phys. Rev. B* **65**, 113413 (2002).
- ³²³S. B. Cronin, A. K. Swan, M. S. Unlu, B. B. Goldberg, M. S. Dresselhaus, and M. Tinkham, *Phys. Rev. B* **72**, 035425 (2005).
- ³²⁴A. G. Souza Filho, N. Kobayashi, J. Jiang, A. Gruneis, R. Saito, S. B. Cronin, J. Mendes, G. G. Samsonidze, G. G. Dresselhaus, and M. S. Dresselhaus, *Phys. Rev. Lett.* **95**, 217403 (2005).
- ³²⁵M. Lucas and R. J. Young, *Phys. Rev. B* **69**, 085405 (2004).
- ³²⁶T. Yu, Z. H. Ni, C. L. Du, Y. M. You, Y. Y. Wang, and Z. X. Shen, *J. Phys. Chem. C* **112**, 12602 (2008).
- ³²⁷Z. H. Ni, T. Yu, Y. H. Lu, Y. Y. Wang, Y. P. Feng, and Z. X. Shen, *ACS Nano* **3**, 483 (2009).
- ³²⁸Z. H. Ni, T. Yu, Y. H. Lu, Y. Y. Wang, Y. P. Feng, and Z. X. Shen, *ACS Nano* **2**, 2301 (2008).
- ³²⁹T. M. G. Mohiuddin, A. Lombardo, R. R. Nair, A. Bonetti, G. Savini, R. Jalil, N. Bonini, D. M. Basko, C. Galiotis, N. Marzari, K. S. Novoselov, A. K. Geim, and A. C. Ferrari, *Phys. Rev. B* **79**, 205433 (2009).
- ³³⁰M. Y. Huang, H. G. Yan, C. Y. Chen, D. H. Song, T. F. Heinz, and J. Hone, *Proc. Natl. Acad. Sci. U.S.A.* **106**, 7304 (2009).
- ³³¹L. S. Ramsdell, *Am. Mineral.* **29**, 431 (1944).
- ³³²J. S. Lukesh and L. Pauling, *Am. Mineral.* **35**, 125 (1950).
- ³³³J. Röhr, M. Hundhausen, K. V. Emtsev, T. Seyller, R. Graupner, and L. Ley, *Appl. Phys. Lett.* **92**, 201918 (2008).
- ³³⁴J. A. Robinson, C. P. Puls, N. E. Staley, J. P. Stitt, M. A. Fanton, K. V. Emtsev, T. Seyller, and Y. Liu, *Nano Lett.* **9**, 964 (2009).
- ³³⁵Z. H. Ni, W. Chen, X. F. Fan, J. L. Kuo, T. Yu, A. T. S. Wee, and Z. X. Shen, *Phys. Rev. B* **77**, 115416 (2008).
- ³³⁶J. C. Tsang, M. Freitag, V. Perebeinos, J. Liu, and P. Avouris, *Nat. Nanotechnol.* **2**, 725 (2007).
- ³³⁷A. Das, A. K. Sood, A. Govindaraj, A. M. Saitta, M. Lazzeri, F. Mauri, and C. N. R. Rao, *Phys. Rev. Lett.* **99**, 136803 (2007).
- ³³⁸S. Piscanec, M. Lazzeri, F. Mauri, A. C. Ferrari, and J. Robertson, *Phys. Rev. Lett.* **93**, 185503 (2004).
- ³³⁹M. Lazzeri and F. Mauri, *Phys. Rev. Lett.* **97**, 266407 (2006).
- ³⁴⁰T. Ando, *J. Phys. Soc. Jpn.* **75**, 054701 (2006).
- ³⁴¹W. Kohn, *Phys. Rev. Lett.* **2**, 393 (1959).
- ³⁴²S. Pisana, M. Lazzeri, C. Casiraghi, K. S. Novoselov, A. K. Geim, A. C. Ferrari, and F. Mauri, *Nature Mater.* **6**, 198 (2007).
- ³⁴³J. Yan, Y. B. Zhang, P. Kim, and A. Pinczuk, *Phys. Rev. Lett.* **98**, 166802 (2007).
- ³⁴⁴A. Das, S. Pisana, B. Chakraborty, S. Piscanec, S. K. Saha, U. V. Waghmare, K. S. Novoselov, H. R. Krishnamurthy, A. K. Geim, A. C. Ferrari, and A. K. Sood, *Nat. Nanotechnol.* **3**, 210 (2008).
- ³⁴⁵J. Yan, E. A. Henriksen, P. Kim, and A. Pinczuk, *Phys. Rev. Lett.* **101**, 136804 (2008).
- ³⁴⁶A. Das, B. Chakraborty, S. Piscanec, S. Pisana, A. K. Sood, and A. C. Ferrari, *Phys. Rev. B* **79**, 155417 (2009).
- ³⁴⁷L. M. Malard, D. C. Elias, E. S. Alves, and M. A. Pimenta, *Phys. Rev. Lett.* **101**, 257401 (2008).
- ³⁴⁸H. E. Romero, N. Shen, P. Joshi, H. R. Gutierrez, S. A. Tadigadapa, J. O. Sofo, and P. C. Eklund, *ACS Nano* **2**, 2037 (2008).
- ³⁴⁹C. Casiraghi, S. Pisana, K. S. Novoselov, A. K. Geim, and A. C. Ferrari, *Appl. Phys. Lett.* **91**, 233108 (2007).
- ³⁵⁰Y. M. Shi, X. C. Dong, P. Chen, J. L. Wang, and L. J. Li, *Phys. Rev. B* **79**, 115402 (2009).
- ³⁵¹D. A. Siegel, S. Y. Zhou, F. El Gabaly, A. V. Fedorov, A. K. Schmid, and A. Lanzara, *Appl. Phys. Lett.* **93**, 243119 (2008).
- ³⁵²C. Stampfer, F. Molitor, D. Graf, K. Ensslin, A. Jungen, C. Hierold, and L. Wirtz, *Appl. Phys. Lett.* **91**, 241907 (2007).
- ³⁵³A. A. Balandin, S. Ghosh, W. Z. Bao, I. Calizo, D. Teweldebrhan, F. Miao, and C. N. Lau, *Nano Lett.* **8**, 902 (2008).
- ³⁵⁴S. Ghosh, I. Calizo, D. Teweldebrhan, E. P. Pokatilov, D. L. Nika, A. A. Balandin, W. Bao, F. Miao, and C. N. Lau, *Appl. Phys. Lett.* **92**, 151911 (2008).
- ³⁵⁵J. Vaari, J. Lahtinen, and P. Hautojarvi, *Catal. Lett.* **44**, 43 (1997).

- ³⁵⁶D. E. Starr, E. M. Pazhetnov, A. I. Stadnichenko, A. I. Boronin, and S. K. Shaikhutdinov, *Surf. Sci.* **600**, 2688 (2006).
- ³⁵⁷N. R. Gall, E. V. Rut'kov, and A. Y. Tontegode, *Phys. Solid State* **46**, 371 (2004).
- ³⁵⁸T. Kawano, M. Kawaguchi, Y. Okamoto, H. Enomoto, and H. Bando, *Solid State Sci.* **4**, 1521 (2002).
- ³⁵⁹H. H. Madden, J. Kuppers, and G. Ertl, *J. Chem. Phys.* **58**, 3401 (1973).
- ³⁶⁰D. W. Goodman and J. T. Yates, *J. Catal.* **82**, 255 (1983).
- ³⁶¹A. G. Starodubov, M. A. Medvetskii, A. M. Shikin, and V. K. Adamchuk, *Phys. Solid State* **46**, 1340 (2004).
- ³⁶²Z. H. Ni, Y. Y. Wang, T. Yu, Y. M. You, and Z. X. Shen, *Phys. Rev. B* **77**, 235403 (2008).
- ³⁶³P. Poncharal, A. Ayari, T. Michel, and J. L. Sauvajol, *Phys. Rev. B* **78**, 113407 (2008).
- ³⁶⁴Z. H. Ni (unpublished).
- ³⁶⁵S. M. Bachilo, M. S. Strano, C. Kittrell, R. H. Hauge, R. E. Smalley, and R. B. Weisman, *Science* **298**, 2361 (2002).
- ³⁶⁶A. Jorio, R. Saito, J. H. Hafner, C. M. Lieber, M. Hunter, T. McClure, G. Dresselhaus, and M. S. Dresselhaus, *Phys. Rev. Lett.* **86**, 1118 (2001).
- ³⁶⁷A. Jorio, A. G. Souza, G. Dresselhaus, M. S. Dresselhaus, A. K. Swan, M. S. Unlu, B. B. Goldberg, M. A. Pimenta, J. H. Hafner, C. M. Lieber, and R. Saito, *Phys. Rev. B* **65**, 155412 (2002).
- ³⁶⁸M. S. Strano, S. K. Doorn, E. H. Haroz, C. Kittrell, R. H. Hauge, and R. E. Smalley, *Nano Lett.* **3**, 1091 (2003).
- ³⁶⁹M. S. Strano, *J. Am. Chem. Soc.* **125**, 16148 (2003).
- ³⁷⁰L. G. Cançado, M. A. Pimenta, B. R. A. Neves, M. S. S. Dantas, and A. Jorio, *Phys. Rev. Lett.* **93**, 247401 (2004).
- ³⁷¹Y. M. You, Z. H. Ni, T. Yu, and Z. X. Shen, *Appl. Phys. Lett.* **93**, 163112 (2008).
- ³⁷²A. K. Gupta, T. J. Russin, H. R. Gutierrez, and P. C. Eklund, *ACS Nano* **3**, 45 (2009).
- ³⁷³C. Casiraghi, A. Hartschuh, H. Qian, S. Piscanec, C. Georgi, A. Fasoli, K. S. Novoselov, D. M. Basko, and A. C. Ferrari, *Nano Lett.* **9**, 1433 (2009).
- ³⁷⁴A. Gruneis, C. Attacalite, A. Rubio, D. V. Vyalikh, S. L. Molodtsov, J. Fink, R. Follath, W. Eberhardt, B. Buchner, and T. Pichler, *Phys. Rev. B* **79**, 205106 (2009).
- ³⁷⁵Y. M. Lin, K. A. Jenkins, A. Valdes-Garcia, J. P. Small, D. B. Farmer, and P. Avouris, *Nano Lett.* **9**, 422 (2009).
- ³⁷⁶X. Wang, L. J. Zhi, and K. Mullen, *Nano Lett.* **8**, 323 (2008).
- ³⁷⁷G. Eda, Y. Y. Lin, S. Miller, C. W. Chen, W. F. Su, and M. Chhowalla, *Appl. Phys. Lett.* **92**, 233305 (2008).
- ³⁷⁸J. B. Wu, H. A. Becerril, Z. N. Bao, Z. F. Liu, Y. S. Chen, and P. Peumans, *Appl. Phys. Lett.* **92**, 263302 (2008).
- ³⁷⁹S. Watcharotone, D. A. Dikin, S. Stankovich, R. Piner, I. Jung, G. H. B. Dommett, G. Evmenenko, S. E. Wu, S. F. Chen, C. P. Liu, S. T. Nguyen, and R. S. Ruoff, *Nano Lett.* **7**, 1888 (2007).
- ³⁸⁰C. Lee, X. D. Wei, J. W. Kysar, and J. Hone, *Science* **321**, 385 (2008).
- ³⁸¹C. Nisoli, P. E. Lammert, E. Mockensturm, and V. H. Crespi, *Phys. Rev. Lett.* **99**, 045501 (2007).
- ³⁸²D. Garcia-Sanchez, A. M. van der Zande, A. S. Paulo, B. Lassagne, P. L. McEuen, and A. Bachtold, *Nano Lett.* **8**, 1399 (2008).
- ³⁸³O. H. Kwon, B. Barwick, H. S. Park, J. S. Baskin, and A. H. Zewail, *Nano Lett.* **8**, 3557 (2008).
- ³⁸⁴M. Poot and H. S. J. van der Zant, *Appl. Phys. Lett.* **92**, 063111 (2008).
- ³⁸⁵T. J. Booth, P. Blake, R. R. Nair, D. Jiang, E. W. Hill, U. Bangert, A. Bleloch, M. Gass, K. S. Novoselov, M. I. Katsnelson, and A. K. Geim, *Nano Lett.* **8**, 2442 (2008).
- ³⁸⁶H. Chen, M. B. Muller, K. J. Gilmore, G. G. Wallace, and D. Li, *Adv. Mater.* **20**, 3557 (2008).
- ³⁸⁷F. Schedin, A. K. Geim, S. V. Morozov, E. W. Hill, P. Blake, M. I. Katsnelson, and K. S. Novoselov, *Nature Mater.* **6**, 652 (2007).
- ³⁸⁸P. K. Ang, W. Chen, A. T. S. Wee, and K. P. Loh, *J. Am. Chem. Soc.* **130**, 14392 (2008).
- ³⁸⁹B. Huang, Z. Y. Li, Z. R. Liu, G. Zhou, S. G. Hao, J. Wu, B. L. Gu, and W. H. Duan, *J. Phys. Chem. C* **112**, 13442 (2008).
- ³⁹⁰I. Jung, D. Dikin, S. Park, W. Cai, S. L. Mielke, and R. S. Ruoff, *J. Phys. Chem. C* **112**, 20264 (2008).
- ³⁹¹O. Leenaerts, B. Partoens, and F. M. Peeters, *Phys. Rev. B* **77**, 125416 (2008).
- ³⁹²N. Mohanty and V. Berry, *Nano Lett.* **8**, 4469 (2008).
- ³⁹³R. Moradian, Y. Mohammadi, and N. Ghobadi, *J. Phys.: Condens. Matter* **20**, 425211 (2008).
- ³⁹⁴N. L. Rangel and J. A. Seminario, *J. Phys. Chem. A* **112**, 13699 (2008).
- ³⁹⁵J. T. Robinson, F. K. Perkins, E. S. Snow, Z. Q. Wei, and P. E. Sheehan, *Nano Lett.* **8**, 3137 (2008).
- ³⁹⁶A. Sakhaee-Pour, M. T. Ahmadian, and A. Vafai, *Solid State Commun.* **145**, 168 (2008).
- ³⁹⁷T. O. Wehling, K. S. Novoselov, S. V. Morozov, E. E. Vdovin, M. I. Katsnelson, A. K. Geim, and A. I. Lichtenstein, *Nano Lett.* **8**, 173 (2008).
- ³⁹⁸Y. P. Dan, Y. Lu, N. J. Kybert, Z. T. Luo, and A. T. C. Johnson, *Nano Lett.* **9**, 1472 (2009).
- ³⁹⁹J. D. Fowler, M. J. Allen, V. C. Tung, Y. Yang, R. B. Kaner, and B. H. Weiller, *ACS Nano* **3**, 301 (2009).
- ⁴⁰⁰I. Žutić, J. Fabian, and S. Das Sarma, *Rev. Mod. Phys.* **76**, 323 (2004).
- ⁴⁰¹N. Tombros, C. Jozsa, M. Popinciuc, H. T. Jonkman, and B. J. van Wees, *Nature (London)* **448**, 571 (2007).
- ⁴⁰²M. Ohishi, M. Shiraishi, R. Nouchi, T. Nozaki, T. Shinjo, and Y. Suzuki, *Jpn. J. Appl. Phys., Part 2* **46**, L605 (2007).
- ⁴⁰³S. J. Cho, Y. F. Chen, and M. S. Fuhrer, *Appl. Phys. Lett.* **91**, 123105 (2007).
- ⁴⁰⁴M. Shiraishi, M. Ohishi, R. Nouchi, T. Nozaki, T. Shinjo, and Y. Suzuki, *Adv. Func. Mater.* **9**, 3711 (2009).
- ⁴⁰⁵W. Han, K. Pi, W. Bao, K. M. McCreary, Y. Li, W. H. Wang, C. N. Lau, and R. K. Kawakami, *Phys. Rev. Lett.* **102**, 137205 (2009).